University of Alberta

Load Modeling Techniques for Power System Dynamic Studies

by

Shengqiang Li

A thesis submitted to the Faculty of Graduate Studies and Research
in partial fulfillment of the requirements for the degree of

Master of Science

in

Power Engineering and Power Electronics

Department of Electrical and Computer Engineering

Spring 2013

Edmonton, Alberta

Abstract

Accurately modeling power system loads is essential in simulation-based power system planning and operation studies. Since large industrial facilities such as petro-chemical plants and paper mills are major power system loads, they must be modeled properly. Utilizing the concept of the template-based load modeling technique for industry facilities, this thesis investigates the modeling of paper mills for power system dynamic studies. A systematic approach with representative data is established for constructing equivalent dynamic models of the Kraft type of paper mills. Case studies demonstrate that the proposed model can capture the dynamic behavior of paper mill facilities adequately and accurately. This thesis also investigates the modeling of DC (motor) drives and their collective dynamic responses for system dynamic studies. The DC drive is one type of elementary load, the modeling of which has not been fully studied in the past. It is also a major load component in paper mills. This work develops an equivalent dynamic model of DC drives, and a model aggregation technique. Simulation results demonstrate the accuracy and usefulness of the proposed model.

Acknowledgements

First and foremost, I would like to express my most sincere gratitude to my supervisor, Professor Wilsun Xu for his tireless guidance and supervision over the past two years. Without his support, I won't have the opportunity to conduct this work and gain valuable knowledge and experience that I will need to succeed in my future career. I am and will always be proud of being his student.

I'd like to show my special appreciation to Dr. Walmir Freitas. His patient guidance and insightful suggestions have contributed greatly to this thesis, especially to Chapter 5.

I thank all my colleagues for their friendship, and it's a great pleasure to work with them. In particular, I'd like to thank my teammates: Xiaodong Liang, Ming Dong, Tiago Ricciardi, and Iraj Rahimi Pordanjani, for their kindly assistance and fruitful discussion.

I'd like to express my highest appreciation to my parents, Mr. Zheng Li and Mrs. Xianqiong Tian. Their unconditional love motivates me to overcome the major difficulties in my life. It's my proud to be their son.

I deeply appreciate my wife, Yi Xiong for her endless love and selfless dedication to our marriage. I wish to lead our marriage to a harmonious and lifelong relationship.

I dedicate this thesis to them all.

Table of Content

List of Tables

List of Figures

Nomenclature

V	Utility-side bus voltage, per-unit.
V_0	Utility-side bus voltage, per-unit (pre-fault condition).
V_{lg}	AC supply voltage of the SCR bridge converter, phase-to-ground.
V_{lg0}	AC supply voltage of the SCR bridge converter, phase-to-ground. (pre-fault condition).
P	Real power consumption of the drive.
P_0	Real power consumption of the drive (pre-fault condition).
Q	Reactive power consumption of the drive.
Q_0	Reactive power consumption of the drive (pre-fault condition).
S	Apparent power consumption of the drive.
S_0	Apparent power consumption of the drive (pre-fault condition).
P_n	Rated motor horsepower.
I_n	Nominal DC motor armature current.
ω_n	Nominal DC motor speed.
R_d	DC armature circuit resistance (total).
L_d	DC armature circuit inductance (total).
K_{pc}	Proportional constant of PI current controller.
K_{ic}	Integral constant of PI current controller.
K_{ps}	Proportional constant of PI speed controller.
K_{is}	Integral constant of PI speed controller.
λ	Over-loading factor.
K_E	Voltage constant of the DC motor.
K_T	Torque constant of the DC motor.
J	Moment of inertia of the DC motor.
I_{ac}	AC-side phase current (RMS).
α	Firing angle of SCR-bridge converter.
i_{dc}	DC motor armature current.
I_{dc}	Averaged DC motor armature current.
v_{dc}	Output voltage of SCR-bridge converter.
V_{dc}	Averaged output voltage of SCR-bridge converter.
e_g	Motor generated voltage (Back EMF)
E_g	Averaged motor generated voltage (Back EMF).
L_C	Commutating inductance.

Chapter 1

Introduction

The modeling of power system loads plays an influential role in simulation and analysis of power system dynamic studies. Having an accurate load model is essential in understanding the system impacts of disturbances, and developing appropriate standards and practices for power system planning and operating. Since large industrial facilities such as petro-chemical plants and paper mills are major loads in power systems, modeling them accurately is especially crucial.

The main topic of this thesis is the modeling of paper mills, one of major industrial loads in the U.S. and Canada，for power system dynamic studies. This introductory chapter briefly reviews the background of modeling loads in power system studies. The chapter also explains the motivation of modeling paper mills as well as DC drives, one type of elementary load component in paper mills. At the end of this chapter, the scope and outline of this thesis are presented.

1.1 Background of Load Models & Power System Studies

This subsection reviews the significance of load models in power system studies, types of classical load models, and traditional and new techniques for modeling

power system loads.

1.1.1 Significance of Load Models in Power System Studies

Accurately modeling power system components is important for simulation-based power system planning and operation studies. An inaccurate system model may either result in poorly-designed power systems or lead to bad decision-making in grid operation. For example, if over-optimistic models are selected, the grid can be designed with an inadequate system security margin or operated in a risky manner so that the system is vulnerable to widespread outages such as the blackout in summer 1996. Conversely, if over-conservative models are selected, the grid can be designed with unnecessary capital investment or operated uneconomically so that an electricity shortage might be exacerbated in highly-stressed areas.

The load is a type of major power system component, which generally refers to the collective power demand at a substation observed from the transmission level. It is well recognized that the modeling of loads is very critical in a variety of power system studies. Many studies have observed that the characteristics of loads play an influential role in the simulation and analysis of power system dynamic behaviors [1-4]. More importantly, the representation of loads has a

major impact on the analysis of voltage instability and system oscillation [2, 3]. In addition, accurately modeling loads is also essential for properly tuning automatic controllers such as SVCs (static VAR compensators) or STATCOM (Static Synchronous Compensator).

However, loads have not been sufficiently modeled in the past, as compared with most other power system components such as generators and transmission equipment which have been modeled accurately with full consideration of their actual physical characteristics. Over decades, loads have been represented by highly simplified models (such as constant impedance, constant current sources, constant power, or combination of them) due to the limitations in computing resources and the inaccessibility of specific load information. Many studies have observed that the insufficiency of the load representation is has become the major obstacle for improving the accuracy of power system dynamic studies [5]. For example, the post-contingency analysis of the summer 1996 blackout found that the deficiency of the load model is the major barrier to predict the undamped oscillation [6].

On one hand, the advance of computing technology has greatly facilitated the improvement of the existing load models; WECC (Western Electricity Coordinating Council) also agrees that the improvements of load model have been

possible and greatly needed [7]. On the other hand, the difficulty in accessing specific load information is still a barrier in modeling loads accurately. In summary, there is an opportunity as well as a challenge for improving the modeling of loads.

1.1.2 Overview of Classical Loads Models

A load model is a mathematical representation of the relationship between a bus voltage (magnitude and frequency) and the power (active and reactive). Generally, the two types of classical load models are static load model and dynamic load models.

Traditionally, loads were represented by static load models, which assume that the active and reactive load is an algebraic function of the bus voltage (magnitude and frequency) and is not dependent on time [8]. A typical example is the polynomial load model, which expresses the active or reactive power as a polynomial function of the voltage. The most common structure of the polynomial load model is the ZIP model (Z-constant impedance, I- constant current, P- constant power) as described by.

$$P_L(V) = P_{L0}\left[a_p \left(\frac{V}{V_0} \right)^2 + b_p \left(\frac{V}{V_0} \right) + c_p \right] \qquad (1.1)$$

where, the frequency dependence is normally disregarded, especially in the

voltage stability studies.

Static ZIP load models have been very popular in power system dynamic simulation programs during the past decades [9] Even today, many utilities had adopted the static ZIP load model for large-scale dynamic performance studies [10]. However, static load models may be inadequate, especially when the bus voltage is changing rapidly within a large range [5, 11].

Realizing the weakness of static load models, many researchers have paid much attention to dynamic load models [12-16]. Unlike the former, the later assume that the active and reactive power is related to both the past and present values of the voltage and frequency and is dependent on time. Dynamic load models normally take the form of an aggregated induction motor model, or a composite load model (in the form of differential equations, or transfer functions) [11].

Because induction motors account for around 60% of the electricity consumption in North America, the inclusion of the dynamics of induction motors has been one of the first attempts to build a dynamic load model [11]. Some utilities' load modeling practices assume that the dynamic part of loads can be simply represented by an aggregated induction motor [6]. For instance, the WSCC interim load model consists of a static part (80% of the total load) and a dynamic

part (20% of the total load, in the form of an induction motor). The induction motor is normally represented by a well-established equivalent circuit model as shown in Figure 1.1.

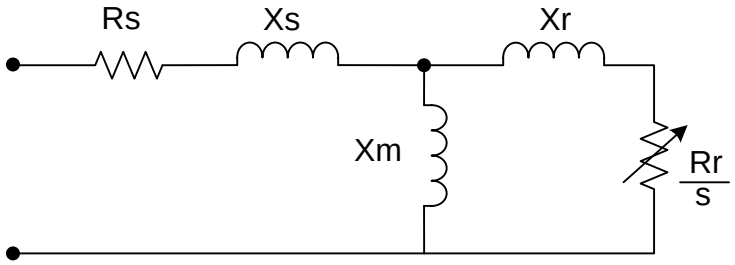

Figure 1.1 Equivalent circuit model of induction motors

A composite load model is another form of load representation. It is the reflection of the collective effects of all down-stream components, i.e. induction motors, synchronous motors, excitation control and tap changers [17]. This model can be represented by differential equations. Reference [17] presents a generic dynamic load model in the form:.

$$T_p \frac{dx}{dt} = P_s(V) - P, \quad P = xP_t(V) \tag{1.2}$$

where T_p is the time constant, and P_t and P_s are the transient and steady-state load characteristics as given by $P_t(V) = V^{\alpha}$ and $P_s(V) = P_0 V^a$.

Alternatively, a composite load model can be also represented by transfer functions [18]. According to [19], the dynamic load model can be simply represented by a first-order transfer function, as presented below:

$$\Delta P(s) = \frac{\tau_p s + k_p}{T_p s + 1} \Delta V(s) \qquad (1.3)$$

where T_p and τ_p are the time constants, and k_p is the gain constant.

In recent years, the electric power industry has reached a consensus that modeling loads with dynamic characteristics is necessary. For example, it's found that the inclusion of load dynamics is critical in capturing the phenomenon of power system damping [20] and post-contingency voltage recovery delay [11].

1.1.3 Traditional Methods of Modeling Power System Loads

Traditionally, the measurement-based method and the component-based method (also called the "bottom-up" method) are the two major approaches for modeling power system loads.

The measurement-based method [21-26] estimates load parameters by using the actual measurements observed at various load substations. For example, the method in [26] is implemented by creating a voltage disturbance with a manual or automatic tap changer and estimating the detailed load parameters by monitoring the load responses at the load substations. The measurement-based method seems to be effective and practical, but unfortunately, it is difficult to generate voltage disturbances that are sufficiently significant for load model measurement.

Additionally, this method is not applicable to long-term planning, because a load model might be needed for the system studies several years ahead of the construction of the facility.

The component-based method, on the other hand builds up the load model from information on its constituent parts (such as induction motors, synchronous motors, static loads, and so on) and is also referred to as the “bottom-up” method [27, 28]. For example, reference [29] presents a typical component-based method, in which the electrical loads in an industrial plant are aggregated and represented by a lumped induction motor and a lumped static load.

The component-based methods normally assume that the electrical system structure and load composition of the industrial facilities are already known. For instance, reference [29] assumes that the single-line diagram is obtainable from the plant engineers and that the motor parameters can be taken from the pre-determined values. This assumption is actually hard to implement, because the requirement for legal confidentiality makes obtaining the specific plant data difficult.

In practice, neither of the two methods is widely used in the industry, which would prefer a simpler method. For instance, the WECC interim load modeling

practise suggests that any type of industrial loads consists of two components: 80% static loads and 20% induction motors [6]. This approach is obviously too rough. For example, our studies have found the difference in motor composition between a paper mill and an aluminum smelter can be up to 50%. One may wonder why the industry is still using such a rough load modeling practice. The main reason is that the grid operators or planners feel reluctant to collect specific load data, especially for long-term power system planning. For example, if a paper mill is planned to be in service after 10 years, grid planners cannot access even the basic information of this plant, such as single-line diagrams, load composition, or loading factors.

In summary, the main drawback of the traditional load modeling methods is the difficulty in accessing the load information (either field measurement data or specific plant data).

1.1.4 An Novel Method of Modeling Power System Loads

In view of the disadvantages of traditional load modeling methods, reference [28] proposed a new method: the template-based load modeling technique. The objective of this method is to model large industrial facilities (such as oil refineries and steel mills) accurately with minimal user input. This method has

been successfully applied to model oil-refinery facilities.

This method is based on the concept of the "template", which means the commonly-shared characteristics on the electrical system configuration for industrial facilities of the same type. The configuration may include typical industrial processes, circuit structure (i.e., single-line diagrams, voltage levels), load composition (i.e., motor types/sizes, AC/DC drives, etc.), and parameters of cables and transformers. The two general steps to construct a template-based load model are the following:

Step A: Software vendors build the template database for the major types of industry facilities that is involved in the utility grid. Table 1.1 presents a list of the major industrial facilities in the North America, as recommended by WECC. The template should include all the eight types of facilities.

Step B: Users utilize the template to model the facility of interest. The main idea is to scale the template to a given size (in MW), and aggregate it into a single-unit equivalence. The final outcome is a single induction motor and a single lumped static load, which is computationally feasible for large-scale system simulation.

Table 1.1 List of major industrial facilities in North America

Type#	Feeder Type	Template ready?
1	Petro-Chemical Plant	Built
2	Paper Mill (Kraft type)	Not built
3	Paper Mill (TMP type)	Not built
4	Aluminum Smelter	Not built
5	Steel Mill	Not built
6	Mining operation	Not built
7	Semiconductor Plant	Not built
8	Server Farm	Not built

This template-based load modeling method has two major advantages: (1) the load model is more accurate than traditional models, and (2) The method requires minimal user input (only the type and capacity of the facility). As a result, this method is especially useful in long-term planning, where specific information for future loads is limited.

The major challenge with this method is that the template database has not been fully established in the past. Theoretically speaking, the template database must include all types of the major industrial facilities connected to the utility grid. Until now, only petro-chemical plants (type#1) have had a template built for them [28]; the templates of other facilities have not been built yet. Consequently, the need to build templates for the other seven types of facilities listed in the Table 1.1 is urgent.

1.2 Motivation of Modeling Paper Mills and DC Drives

Paper mills are the major type of industrial facilities in both the U.S. and Canada. As Table 1.1 reveals, paper mills (both the Kraft Type and TMP type) are among the top 3 of major industrial facilities in the North America [30]. In addition, paper mill loads constitute the major power demand of the utility grid in Canada. According to [31], paper mills consume 30% of the industrial energy used in Canada. Reference [32] also reports that paper mill loads are the major loads of a Canadian utility company (Hydro Ontario).

More importantly, paper mill loads are normally large in capacity. The results of a survey on the size (in MW) of 26 paper mills in British Columbia are presented in Figure 1.2 [33]. The figure shows that most paper mills are between 20 and 40 MW, and many mills have even larger sizes, i.e. 80MW~100MW. The above information indicates that the typical size of a paper mill varies from 20MW to 100MW. This size is normally equivalent to or greater than a single residential/commercial substation.

In summary, there are strong reasons for modeling paper mills with as many details as possible. Hence, this report will use paper mill loads as an example to demonstrate the template-based load modeling method.

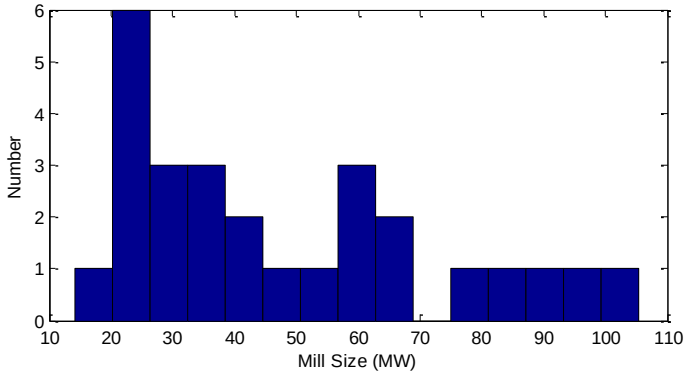

Figure 1.2 Distribution of 26 Paper Mills at B.C. province vs. Mill sizes

DC (motor) drives are one type of elementary load component in many industrial plants, especially in paper mills. Although DC drives are becoming less popular than AC drives, they are still one of the major loads in the industry. Our studies have found that DC drives can account for around 15%~20% of total loads in many large industrial facilities such as paper mills and petro-chemical plants.

Unfortunately, the modeling of DC drives has not been fully studied in the past. Traditionally, motor drives are represented simply as transparent devices[1] in dynamic studies, because these drives are vulnerable to nuisance trips in case of voltage disturbances [34]. In fact, many studies observe that DC drives are able to ride through voltage disturbance within ±10% [35]. Obviously, excluding the DC drives while the modeling of other components such as generators is done accurately is not acceptable. Thus, developing an equivalent model of DC drives

[1] In ETAP, "transparent devices" means the load that is tripped for the during-fault period and recovers immediately to the initial power consumption after the fault clears.

for system dynamic studies is important.

1.3 Thesis Scope and Outline

This thesis investigates mainly the issues of developing load models for power system dynamic studies. Two topics are discussed in this research work.

The first topic discusses the building of an equivalent dynamic model for paper mills by using the template-based load modeling method. The objectives of this discussion include:

1) To investigate the configuration of electrical systems of sample paper mills, extract the commonly shared features, and develop a template for paper mills.

2) To construct a template-based load model for a specific paper mill, and to verify the obtained model by comparing it against the guideline models through ETAP simulation.

The second topic of this thesis is the modeling of DC drives and their collective dynamic response. DC drives are one of the elementary load components in industrial plants, especially in paper mills, but the dynamic model of DC drives

has not been fully studied in the past. The objectives of this discussion include three folds: (1) to determine the tripping criteria for DC drives, (2) to derive an equivalent dynamic model for ride-through DC drives, and (3) to develop a technique to aggregate a group of DC drives.

In addition, this thesis also presents another stability-related research work conducted by the author. This project investigates a novel method to study small-signal stability and is presented to demonstrate the author's workload in the author's MSc. Program.

This thesis is organized as follows:

Chapter 2 presents a survey on the configuration of the electrical systems of paper mills, including the typical processes, system structures, parameters of cables and transformers, and load composition (motor or non-motor, motor types, drive types). The Kraft paper mill, the most representative type of paper mills, is selected as the benchmark case.

Based on the survey in Chapter 2, Chapter 3 develops a facility template of paper mill loads, and models a specific paper mill by using the template-based load modeling method. Through ETAP simulation, the obtained model is verified and

compared to the WECC guideline model.

Chapter 4 investigates the requirements for modeling and aggregating DC drive loads for power system stability studies. This chapter discusses the following three issues: the tripping criteria of DC drives, the equivalent model for ride-through DC drives, and the model aggregation technique.

Chapter 5 presents another research project conducted by the author. This chapter mainly investigates a synchrophasor-based technique for analyzing and monitoring the small-signal angle stability.

Chapter 6 concludes this thesis and provides suggestions for future researches.

Appendix A summarizes the data sources used for the survey in Chapter 2.

Appendix B presents the detailed derivation of the proposed DC drive model.

Appendix C documents the Pade-approximation-based model reduction method.

Appendix D documents the parameters of the DC drives used for the simulation studies and model validation.

Appendix E presents a Matlab function “Build_DD” to convert the input data into an equivalent dynamic model for DC drives.

Appendix F presents a package of Matlab functions to implement the proposed aggregation techniques.

Chapter 2

Overviews of Paper Mill Facilities

Paper mills are used as an example to demonstrate the template-based load modeling method in this thesis. The first step is to build the template of paper mill facilities. For this reason, this chapter presents a survey on electrical system configurations of paper mills, and extracts their commonly shared features that are necessary for constructing the template. The representative data is summarized at the end of this chapter.

2.1 Types of Paper Mills

Generally, there are four types of paper mills by pulping process: Kraft-type, Mechanical-type, Recycled-type, and Sulphite-type. Different types of paper mills may or may not have different configuration of electrical systems (i.e. source of energy, and load composition). So we must select the most representative type of paper mills that can be used to establish the template.

According to Lockwood's Directory (1990 edition) [36], Kraft paper mills and TMP (Thermal Mechanical Pulping) paper mills are the most popular types, together accounting for approximately 90% of total mills in North America. Table

2.1 reveals that Kraft mills are the most popular type in the United States, accounting for over 50% of the total mills.

Table 2.1 Distribution of 136 pulp mills in USA (Lockwood's Directory)

Pulp Mill Type	**Number**	**Percentage (%)**
Kraft Mills	74	54.4
TMP Mills	48	35.3
Other	14	10.3
Total	136	100

Kraft paper mill is also the major type of paper mills in Canada. Table 2.2 presents the distribution of 49 paper mills of different types [31]. It's observed that Kraft paper mills account for approximately 50% of paper mills in Canada. In addition, Kraft-type paper mills contribute to 67.8% of the total pulp and paper production in the North America [36]. Therefore, in terms of both the number of mills and electricity consumption (proportional to production), Kraft-type paper mills is dominant among others.

Table 2.2 Distribution of mills by pulping process

Total Mills in Data Analysis: 49	
Mills by Pulping Process	Numbers
Kraft-pulping mill	**24**
Mechanical-pulping mill	28
Recycled-pulping mill	10
Sulphite-pulping mill	4

Therefore, we have sufficient reasons to select Kraft paper mill as a representative

example of paper mills. In this report, a Kraft Paper mill with the capacity of 88MW is chosen as a benchmark case. The major specifications of this mill are presented as below.

Table 2.3 Specifications of a Kraft Paper mill (Benchmark Case)

Capacity	88MW
Major products	Kraft pulp + Uncoated paper
Annual production	680 000 tons/year
Non-motor Load, %	17.8%
Motor Load, %	82.3%
Source of electricity	Co-generation plus Utility supply
One-line diagram available?	Yes
Voltage levels of motors	4.16kV, 0.44kV

2.2 Typical Processes of Paper Mills (Kraft-type)

According to the survey on the sample facility data, Canadian paper mill directory [37] and the design handbook of paper mills [36], there are normally ten major chemical processes in Kraft paper mills, as shown below in Figure 2.1. Note that the general buildings and other ancillary loads are categorized into Process 10 (Other). The explanations of these chemical processes (sub-process and major equipment) are as shown in the Table 2.4.

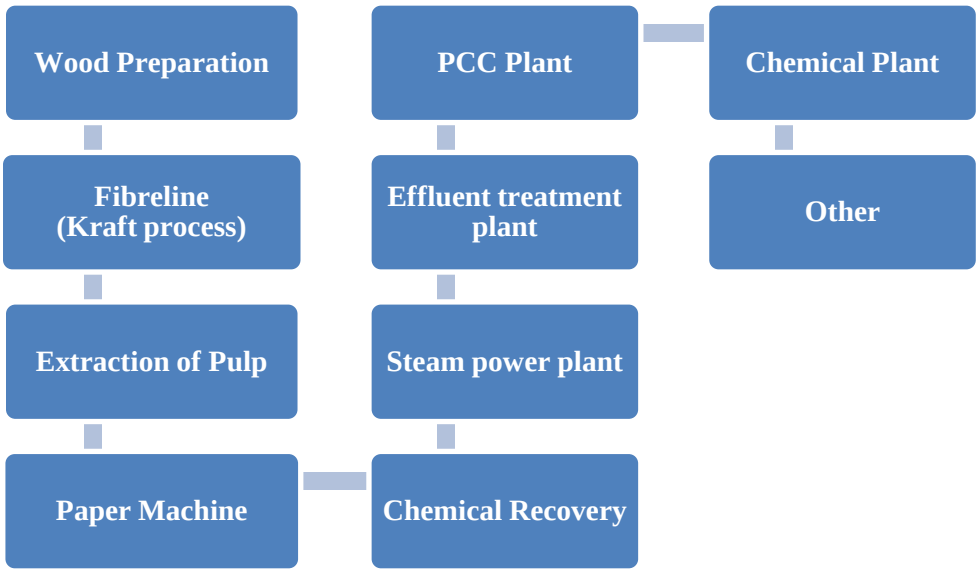

Figure 2.1 Major processes in a typical Kraft paper mill

Table 2.4 Major Processes, Sub-process and Equipment in Kraft Paper Mills

Process	Sub-process	Explanation	Major Equipment
Wood Preparation	Debarking	To remove barks of logs	Barking Drum
	Chipping	To convert logs in to chips.	Chipper
	Chip screening	To screen out moistures from chips	Roller screen
Fibreline (Kraft process)	Cooking	The wood chips are cooked in digesters with liquor made of sodium hydroxide and sodium sulfide	Continuous digester Boiler/Cooling Tower
	Washing	The process where the used cooking liquors are separated from the cellulose fibers	Brownstock Washer
	Oxygen delignification	Part of the residual lignin left in pulp after cooking is removed using oxygen and alkali.	oxygen delignification reactor
	Screening	The process where the pulp is separated from large shives, knots, dirt and other debris.	Cowan screen
	Bleaching	To bleach the pulp by	Power pump,

		treating it with chlorine, chlorine dioxide, ozone, peroxide et al.	Dilution Thread, Cleaner
Extraction of Pulp	Beating & Refining	Bleached pulp slurry. Alum, Dyes, Clay, Titanium Dioxide, added.	Pulp Beater, Jordans Hydrapulper,
Paper Machine	Sheet forming, Pressing, Drying, Packaging	Through press, drying, cutting and packaging process, paper products is made in paper	Headbox, Dryer, Fourdrinier, Winder
Chemical Recovery	Recovery Boiler & Evaporator	To recycle and regenerate cooking chemicals; Heat recovery	
	Causticizing/Calcination	The process of converting sodium carbonate into sodium hydroxide.	
Steam power plant	Ancillary boiler	To service the conventional steam power plant	
Effluent treatment plant	None	Effluents are treated in a biological effluent treatment plant	
PCC Plant	None	To produce Precipitated Calcium Carbonate (PCC) which is an additive of papermaking	
Chemical Plant	None	To provide the chemicals for papermaking (i.e. Na_2S, NaOH)	
Other	Compressors, Air conditioner, Office, Canteen, Lighting	General areas	

The benchmark case (Table 2.3) is used to quantify the power demand distributed in each process. According to the benchmark facility, the typical power demand (in %) of each process is shown in Table 2.5. The representative electrical loads

are also presented in this table. These loads indicated in this table are mainly large motors or heating loads. As seen in this table, the processes that consume most of electricity include paper machine, Fiber line, chemical recovery, etc.

In summary, the typical processes shown in Table 2.4 and the distribution of power demand shown in Table 2.5 can be used to establish the template for Kraft paper mill facilities.

Table 2.5 Typical power demand of each process (benchmark case)

	Processes	Power Demand (%)	Representative Electrical Loads
1	Preparation of wood	5.0	Chipper, barking drum
2	Chemical recovery	15.2	Recovery boiler, evaporator
3	Power plant	3.6	Ancillary boiler
4	Extraction of pulp	13.7	Pulp beater, Hydrapulper
5	Fibreline	16.2	Digester, boiler/cooling tower
6	Paper machine	21.0	Dryer, Fourdrinier, winder
7	Effluent treatment plant	7.7	
8	PCC plant	2.4	
9	Chemical plant	7.2	
10	Other	8.1	Air conditioner

2.3 Electrical Systems of Paper Mills (Kraft-type)

This subsection presents a survey on the common characteristics of electrical systems of Kraft paper mills. This survey is based on real-facility plant data,

technical documents, facility design manuals, and experience of electrical engineers who are working or used to work in the paper mills. The survey intends to provide technical evidences and support to establish a "template" for Kraft paper mill facilities. This subsection will cover the five issues as follows.

- Source of electrical power supplies (utility / co-generation)
- Typical structures of distribution systems (i.e. connection structures, voltage levels)
- Typical parameters for cables and transformers
- Load composition of Kraft paper mills (induction motor / DC motors / synchronous motors, AC/DC drives)

2.3.1 Source of Electrical Power Supplies

The electrical power consumed in a Kraft paper mills is typically a combination of purchased power from utility and self-generated power from co-generation units.

While a few large and fortunate mills are self-sufficient in electrical power, a number of smaller mills are totally dependent on power supplied by local utility grid. Table 2.6 shows a survey on the co-generating units of 7 Kraft paper mills. It's seen that except for a few smaller mills, most of Kraft paper mills have their own co-generating unit, and that the percentage of self-sufficiency level is ranging from 60% to 100%.

Table 2.6 Level of self-generated power for some Kraft paper mills

Mill Name	Full Capacity (MW)	Self-Generated Power (MW)	Percentage of Self-Sufficiency (%)
BC Mill_1990 BC, Canada	30.8	0	0
Intercontinental Mill BC, Canada	40	25	62.5
Papier Kingsey Falls BC, Canada	50	32	64
Northwood Pulp Mill BC, Canada	54	47	87.0
Simpson Tacoma Kraft, Tacoma WA	55	60	109.1
North Wood Pulp Mills BC, Canada	75	60	80
Tolko Manitoba Kraft Papers Manitoba, Canada	153	123	80
Average	--	--	80

In this thesis, the average value for self-sufficiency level is taking 80%. This high level of self-sufficiency is very common in Kraft paper mills, not only due to the economical consideration, but also because of the motivation to utilize the massive biomass produced from Kraft process.

Note that if the self-sufficiency level of the facility of interest is already known, the specific plant data should be used. Otherwise, if this information is unavailable, the self-sufficiency level for the facility model can be taken from the 80% average value.

2.3.2 Typical Structure of Industrial Distribution Systems

Industrial distribution systems of the majority of industrial facilities have radial (tree) configurations, as shown in Figure 2.2. For the purpose of reliability, the electricity supply of the facility is often fed by two main transformers (i.e. T1 or T2) with redundant capacity. Loads of different processes are connected to the main bus by one or two service transformers (i.e. T3). At the downstream of the radial system are multiple motors (or other types of loads) connected to the same buses. These motors or loads are connected to either the medium-voltage bus (2.4kV or 4.16kV) or the low-voltage bus (0.44kV).

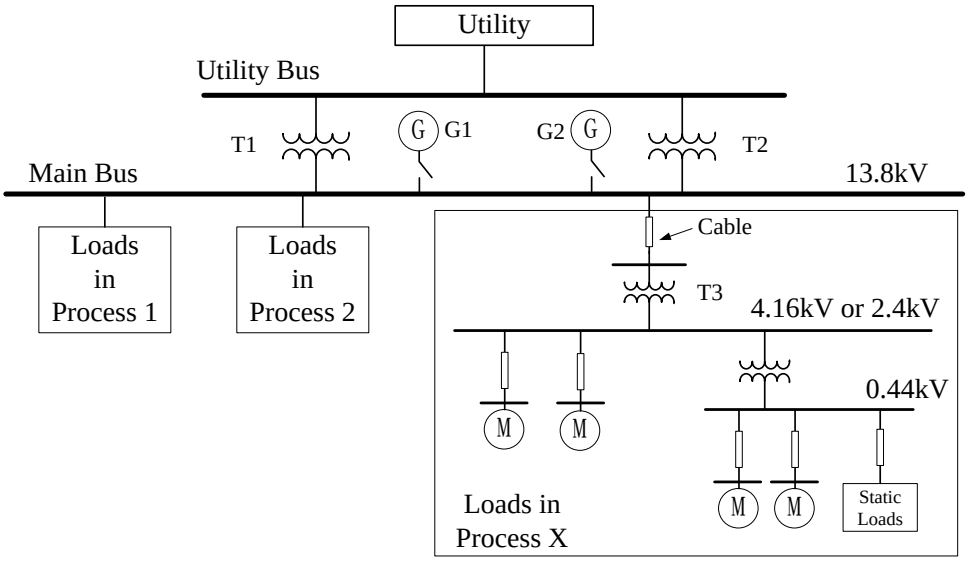

Figure 2.2 Typical structure of industrial distribution systems

Most of Kraft paper mills have co-generation system, since the process of Kraft pulping yields a considerable amount of bio-mass, which can be used for bio-mass

power plant (i.e. G1 and G2 are the two co-generation synchronous machines of the bio-mass power plant).

As seen in Figure 2.2, the voltage levels of a typical industrial distribution system are taking the below values: 13.8 kV for the main bus, 4.16 or 2.4kV for the medium voltage bus, 0.44kV for the low voltage bus. This distribution of loads in different voltage levels is determined based on the survey of real industrial facilities. Table 2.7 shows the survey on distribution of loads connected to different voltage levels, for several real-case industrial facilities [28, 38]. It is observed that the major motor voltage levels used in the facilities are 480V/600 V, 2.4 kV, and 4.16 kV. Although 13.2-kV motors are used in some facilities, they are not very common. Therefore, voltage level distribution in this report thereby adopts the result as shown in Table 2.7.

Table 2.7 Distribution of loads vs. voltage levels

Voltage level	480V	2.4kV	4.16kV
Load distribution (%)	35	15	50

2.3.3 Typical Parameters of Cables and Transformers

Since the impedance of cables and transformers have an influence on the dynamic response of the motors and other loads, we need to document the parameters of

cables and transformers in a typical Kraft paper mill. Hereby, we utilize the data extracted from the benchmark case (Brazilian 80MW Kraft paper mills) to build a database of cables and transformers used at PKM facilities.

Underground cables are widely used in Kraft paper mills for power distribution. The major types of cables and their parameters (length, size, resistance per unit length, and resistance per unit length, voltage level, etc.) are as given in Table 2.8. Note that only positive sequence data is documented, because the zero/positive sequence parameters are not considered in system stability studies.

Table 2.8 Typical Parameters for Cables Used in Paper Mills

Dielectric Rating (kV)	Used on Bus (kV)	Conductor Size(mm^2)	Typical Length (m)	R(Ω/km)	X(Ω/km)
138	138	120	1000	0.19	0.504
20	13.8	185	400-500	0.128	0.119
20	13.8	95	400-850	0.247	0.131
15	13.8	150	450	0.16	0.115
6	4.16	120	30-50	0.197	0.0997
6	4.16	95	30-50	0.247	0.103
1	0.44	300	30-50	0.0812	0.0836
1	0.44	240	30-50	0.0998	0.0843
1	0.44	185	30-50	0.129	0.0854

The typical parameters of transformers (primary-side voltage rating, secondary-side voltage rating, positive sequence impedance Z, and X/R ratio, etc.) are also documented in the below Table 2.9.

Table 2.9 Typical Parameters for Cables Used in Paper Mills

Primary rated voltage (kV)	Secondary rated voltage (kV)	Capacity (MVA)	Z(%)	X/R ratio
138	13.8	100	12.5	34
13.8	4.16	3.0	7.0	10.67
13.8	4.16	6.0	7.0	12.85
13.8	4.16	9.0	8.0	15.5
13.8	4.16	5.0	7.0	12.14
13.8	2.4	2.0	6.0	7.098
13.8	2.4	3.0	7.0	10.67
13.8	0.44	2.0	6.0	7.098
13.8	0.44	1.5	6.0	7.098
13.8	0.44	1.0	5.0	5.79
13.8	0.44	0.5	5.0	3.96
4.16	0.44	0.75	5.0	3.96

2.3.4 Load Composition of Paper Mills

According to a survey [39] on motor loads conducted by U.S. Dept. of Energy (DOE), the motor loads contribute 82% of the total electricity use in pulp and paper industry, as seen in Figure 2.3. Since electrical motors take a dominant position in electricity consumption, it's very necessary to investigate the motor composition in terms of motor type (Synchronous/Asynchronous) and drive type (AC drive/DC drive).

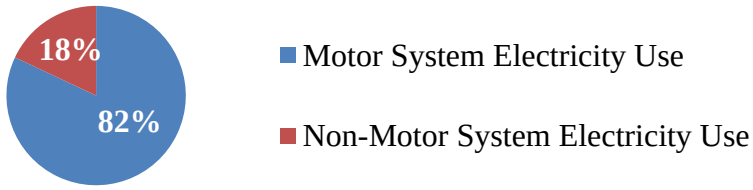

Figure 2.3 Electricity usage in paper industry (Data Source: U.S. Department of Energy Motor System Survey)

Table 2.10 and Table 2.11 present a survey on the motor composition of Kraft paper mills. As presented, there is a considerable difference in motor composition between older mills and newer (or recently upgraded) mills. In addition, the electrical engineers at paper mills also support that old mills and new mills have a completely different motor composition. For example, in an old mill, the capacity of DC motors and synchronous motors in combine may account for up to 40% as of total motor loads, while this number could be as small as zero in the majority of new mills.

Table 2.10 Motor composition of older Kraft paper mill facilities

Mill Name	**MW**	**Induction Motor (%)**	**DC motor (%)**	**Synchronous Motor (%)**
BC Mill_1990*	30.8	71.5	17.6	10.9
Linerboard Mill_1*	55.4	60.5	17.3	22.2
Linerboard Mill_2*	113.7	74.3	10.9	14.8
Fine paper_1*	78.3	69.9	20.2	9.9
Expert estimation**	\	55.0	25.0	20.0
Template Value		**65.0**	**20.0**	**15.0**

*: Data provided by James Gibson, with Weyerhaeuser Paper Inc.

**: Data provided by Walter V. Jones, with TMEIC Solutions Inc.

Table 2.11 Motor composition of newer Kraft paper mill facilities

Mill Name	**MW**	**Induction Motor (%)**	**DC motor (%)**	**Synchronous Motor (%)**
Suzano Mill*	88.0	100.0	0	0
Fray Bentos Mill [40, 41]	122.0	100.0	0	0
Simpson Tacoma Mill [42]	55.0	100.0	0	0
Expert suggests**	\	100.0	0	0
Template Value		**100.0**	**0**	**0**

*: Case file provided by Tiago R. Ricciardi

**: Data provided by Mark Weaver, with Rockwell Automation

Consequently, Kraft paper mill facilities should be classified into two sub-categories, represented by two different templates. Different motor compositions should be taken for the template of new mills and that of old mills, respectively. In this report, the template value is chosen based on both the real-facility data and experts' estimation. Based on those considerations, Table 2.10 and Table 2.11 present a survey on the motor composition for typical Kraft paper mill facilities (newer and older). The template value is estimated based on the average of the facilities surveyed.

In addition, it is observed in Table 2.10 and Table 2.11 that the load composition is very similar for Kraft paper mills of various sizes. This observation is consistent with the basic assumption of template-based load models that industrial facilities of the same type have a similar load composition and dynamic behavior.

Note that power electronic drives may be used for DC motors and induction motors. So DC/AC drives must be included in the model. But power electronic drives are not commonly used for synchronous motors. According to the industrial experts, most of the synchronous motors are directly connected to the AC power supply.

Since power electronic loads (i.e. variable frequency drives, VFD) have an

influence on power system stability [43], we need to investigate the penetration level of VFD in Kraft paper mill facilities.

According to a survey on VFD applications conducted by U.S. Department of Energy in 2002, the average VFD penetration level is around 4% for a wide range of industries. In addition, the industry experts observe that the number of VFD loads is very few in older paper mills. This is because DC motor drives are dominantly used in older mills for variable speed applications. In summary, the VFD penetration level for Kraft-type of paper mills is given by Table 2.12.

Table 2.12 VFD penetration level in paper industry

Motor types	Older Mills	Newer Mills
Induction Motor without VFD (% as of total HP induction motor)	100%	96%
Induction Motor with VFD (% as of total HP induction motor)	≈0%	4%

In addition, we need to know which particular process contains VFD loads. Reference [44] provide a list of processes in paper mills that could involve VFD loads, as seen in Table 2.13.

Table 2.13 Processes typically equipped with VFD in a paper mill (Kraft)

	Processes	Motors equipped with VFD
1	Preparation of Wood	Yes
2	Chemical Recovery	--
3	Power Plant	--
4	Extraction of Pulp	Yes
5	Fibreline	Yes

6	Paper Machine	Yes
7	Effluent Treatment	Yes
8	PCC Plant	--
9	Chemical Plant	--
10	Other	--

VFD loads are simply modeled as static loads in this thesis, because there is no well-developed model for VFD loads. For the same reason, most of commercialized simulation software (i.e. ETAP and DIgSILENT) treats VFD drives as transparent devices for the transient stability studies [45].

2.4 Summary of Representative Data

Based on the survey presented in this chapter, the representative data, as summarized below, can be used to construct the template of paper mill facilities.

- The facility template has 10 processes shown in Figure 2.1; the typical loads in each process should take the value as shown in Table 2.10.

- The template has the radial structure of distribution systems with four voltage levels (13.8kV, 4.16kV, 2.4kV, and 0.44kV), two main transformers, and optional co-generating synchronous machines.

- The parameters of cables and transformers are documented in Table 2.8 and Table 2.9.

- In the template, motor loads account for 82% of total loads, and static loads account for 18% of the total load. The motor composition for older mills and newer mills is taking the different values as given by Table 2.14.

Table 2.14 Motor/non-motor load composition of Kraft paper mills

Load types	Type 2-Older mills	Type 1-Newe`r mills
IM, without VFD (%)	53.3	78.7
IM, with VFD (%)	0	3.3
DC motor (%)	16.4	0
Syn. motor (%)	12.3	0
Static loads	18.0	18.0

- VFD loads are modeled as static loads in this report, unless a proper dynamic load model for VFD loads is developed in the future.

Chapter 3

Example of Modeling Paper Mills (Kraft-type)

In this chapter, a template-based approach has been established for constructing equivalent dynamic models of paper mills. Firstly, this chapter reviews the general procedures and requirements of the template-based load modeling method. Secondly, the template of paper mills (Kraft type) has been constructed based on the representative data summarized in chapter 2. The template has been used for modeling a specific paper mill. Finally, the obtained model is further verified through ETAP simulation and compared against the WECC guideline load model.

3.1 Template-Based Facility Modeling Method

This subsection briefly reviews the template-based load modeling method established by reference [28] (Liang's paper published on IEEE transaction on Power Systems). General procedures and technical requirements of this method are discussed.

3.1.1 General Procedures

Our extensive studies have observed that industrial facilities of the same kind

have many commonly-shared features in their electrical system configurations. Due to these common features, the industrial facilities of the same kind can be represented with similar load characteristics.

Based on these considerations, reference [28] proposed a template-based load modeling method. In this reference, “template” means the commonly-shared features of industrial facilities of the same kind in their electrical system configurations [28]. These common features could include, but not limited to:

- Industrial processes,
- Circuit structure,
- Load composition,
- Parameters of cables and transformers.

A template can be extracted from various data sources including:

- Sample facilities,
- Facility design manuals or technologist handbooks,
- Technical database / survey,
- Interview with facility electrical engineers.

The method has two general steps as follow:

Step A: Software vendors build the template database. The Software vendors need to develop a template database that includes the major types of large industrial facilities. A template should contain the following components:

1) A typical single-line diagram and voltage levels of distribution systems (for example, Figure 2.2).

2) Template scaling rules (load composition), as seen in Table 3.1.

3) Typical parameters of cables and transformers.

Table 3.1 A sample template scaling rules table

#	Process	Rated loads, % of total load	480V induction motor, % of total load	Static loads, % of total load
1	Process #1	20	15	5
2	Process #2	45	35	10
3	Process #3	35	30	5
	total	100	80	20

Step B: Users utilize the template to model the facility of interest (Steps are seen in Fig.1). The procedures of Step B are shown in Figure 3.1.

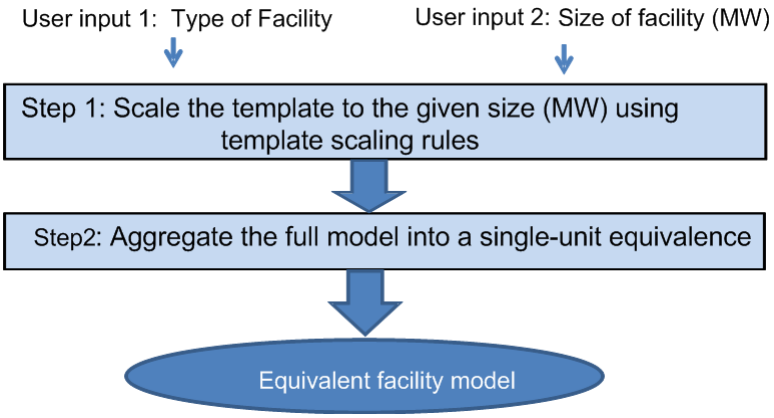

Figure 3.1 Procedures of Step B

Step B.1 is to scale the template to a given size (in MW). There are two required input: facility type (select from Table 1.1) and facility capacity (in MW). The template of the given type should be scaled to the given size per the "template scaling rules", as seen in Table 3.1. Note that only the motors and loads are scaled up or down; the cables and transformers are kept unchanged.

Step B.2 is to aggregate the full template model into a single-unit equivalence. After the Step B.1, the scaled template may contain hundreds of motors. Using the concept of "bottom-up" equivalence, various machines and loads can be aggregated and represented as a systematic single-unit equivalent model, which contains one aggregated induction motor, and/or one aggregated synchronous motor, and one aggregated static load. The final outcome is called "Equivalent Facility (EF) model" (Figure 3.2), which is computationally feasible for large-scale system simulation.

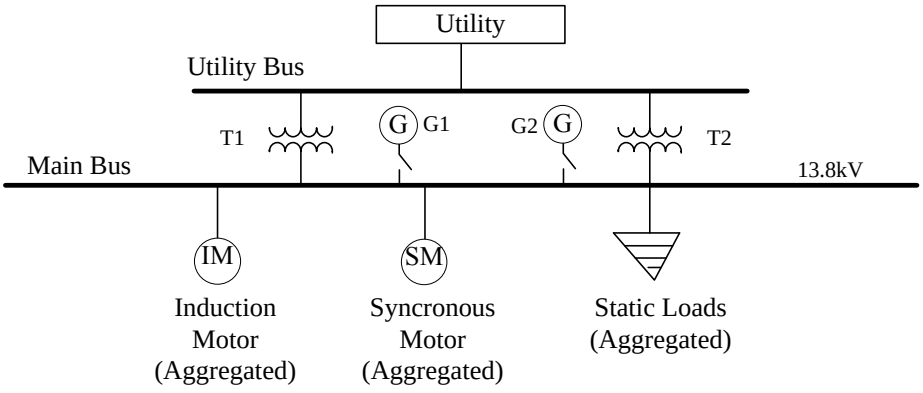

Figure 3.2 Atypical Equivalent Facility (EF) model

3.1.2 Technical Requirement

Model aggregation and system equivalence (Step B.2) is the key step of the proposed method. This section will discuss the required techniques for aggregating the most common load components including static loads, induction motors, synchronous motors, and motor drives.

Aggregating static loads

Static loads of each process are added together to form a single lumped static load for the whole facility, which is modeled as constant impedance connected to the main bus, as calculated below.

$$Z_{Lump} = \frac{P_{Static,Total} + jQ_{Static,Total}}{V^2}$$

Aggregate induction motor (IM) loads

Induction motors are normally represented with circuit models as shown by Figure 3.3. In this circuit model, “s” represents the motor slip. Most of aggregation techniques are based on this circuit model and have been well established and verified in existing publications. A typical example of such techniques is given by reference [16].

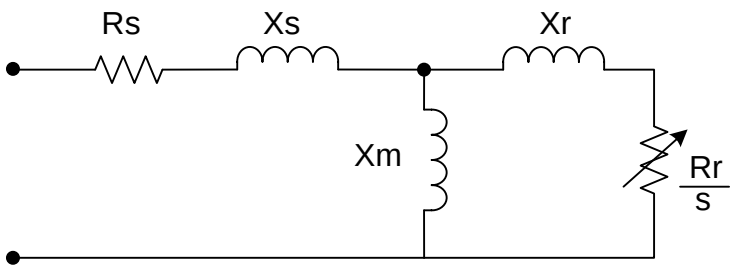

Figure 3.3 Circuit model of induction motors

The basic idea of reference [16] is to aggregate the models by obtaining the equivalent circuit of a group of in-parallel circuit models. The highlight of this idea is the introduction of an alternative equivalent circuit that replace the stator impedance Z_s (=R_s+jX_s) with a fictitious impedance Z_{fic}, which highly facilitate the process of model aggregation.

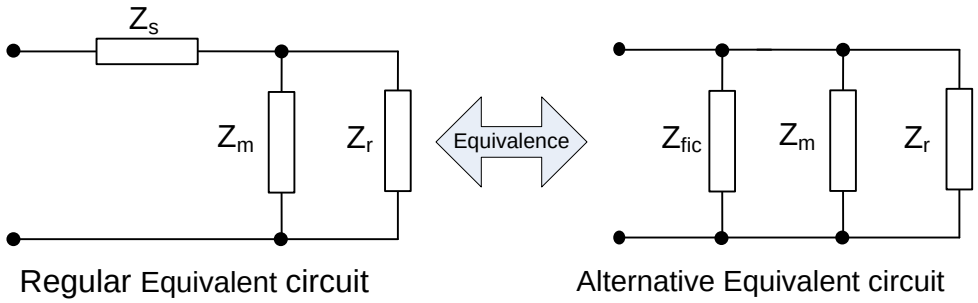

Figure 3.4 Alternative equivalent circuit model

According to [16], the fictitious resistance Z_{fic} in this model can be calculated under block rotor condition (s=1), as given by,

$$Z_s + \frac{1}{\frac{1}{Z_m}+\frac{1}{Z_r}} = \frac{1}{\frac{1}{Z_{fic}}+\frac{1}{Z_m}+\frac{1}{Z_r}} \qquad (3.1)$$

Hence, the circuit parameters of aggregated model can be obtained by in-parallel circuit equivalence as given by,

$$Z_m^{agg} = \frac{1}{\sum_{i=1}^{n} \frac{1}{Z_m^i}}, Z_r^{agg} = \frac{1}{\sum_{i=1}^{n} \frac{1}{Z_r^i}}, \text{ and } Z_{fic}^{agg} = \frac{1}{\sum_{i=1}^{n} \frac{1}{Z_{fic}^i}} \quad (3.2)$$

The final circuit model should be converted into the form of regular circuit model. The aggregated stator resistance Z_s^{agg} can be obtained from (3.1).

Reference [16] has also developed a simple method to a. The aggregated slip "*s*" can be obtained by equalizing between the active power of the total power ($P_{\sum}$) and the aggregated model (P_{agg}). In other words, slip "*s*" can be obtainable by solving the below equation,

$$P_{agg}(\mathrm{s}) - P_{\Sigma} = 0 \quad (3.3)$$

where, $P_{agg}(s) = \mathrm{Re}\left(Y_{tot}^{*} V^2\right)$ and Y_{tot} is the total admittance of the circuit model as of the function of slip "s".

As of the mechanical loads, a simple way to aggregated them is to just summarize them. For the inertia constant, a simple way to aggregated them is to calculate their weighted average using their rated power (HP). Then we can obtain the aggregated mechanical loads and inertia constant, as given by,

$$T_{m,agg} = \sum T_i \quad (3.4)$$

$$H_{agg} = \sum P_{rate,i} H_i \quad (3.5)$$

For the series impedance (transmission lines, cables and transformers) connecting

the induction motors, one can simply incorporate them with Z_s as shown in the circuit model as presented. In summary, this thesis will adopt this technique to aggregate the induction model loads for model reduction.

Aggregate synchronous motor (SM) loads

The technique for aggregating Synchronous motor loads has been well established in reference [46]. Note that the technique for aggregating synchronous motors is not covered in this thesis, because the case study of this thesis only focuses on modeling newer Kraft paper mills which don't have considerable amount of synchronous motor loads. However, if we need to model facility loads that contain many synchronous motors, we need to include the aggregation technique synchronous motor loads.

Aggregating Motor Drive Loads

AC/DC motor drives are widely used in the industry drive systems; however the modeling of them is not fully studied in the past. For this reason, AC/DC drives are simply treated as static load in the template-based models. In order to include motor drives in the future, this thesis will discuss the modeling of DC drives in Chapter 4. For the modeling of AC drives, there is another project (in process) being conducted in Power Lab at University of Alberta.

3.2 Modeling Paper Mills (Kraft-type)

In this subsection, the template of Kraft-type paper mills is constructed with the representative data in Chapter 2. Using the template, a load model is established for a specific paper mill facility. Finally, the established load model is verified through ETAP simulation.

3.2.1 Establishing a Template of Kraft Paper Mills

According to the template-based load modeling method, the first procedure is to build the template. Hence, in this subsection, the template of Kraft-type paper mills is constructed based on the most representative data (see Chapter 2). This template contains three parts of information as follow.

(1) Circuit structure (single-line diagrams and voltage levels). The typical data can be obtained from the section 2.3.2. By referring to the sample systems, one can develop a single line diagram for the template as shown in Figure 3.5. Each subsystem (little square) in Figure 3.5 consists of a number of motors and loads involved in an industrial process.

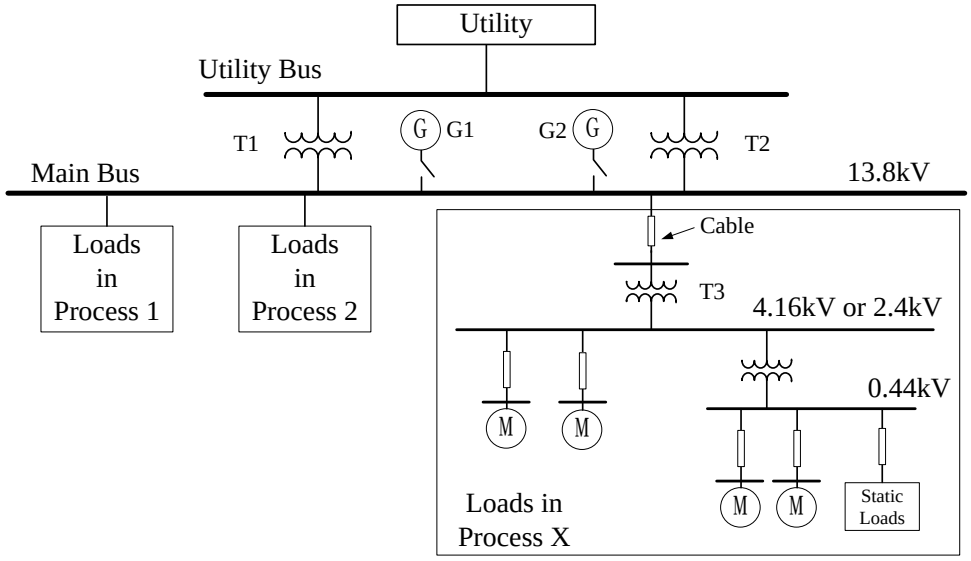

Figure 3.5 A typical circuit structure in Kraft paper mills

(2) Typical parameters of cables and transformers. The cable and transformer data has been documented in section 2.3.3. Using the typical data, one can easily set values for the cables and transformers. Note that in the template, cables are modeled as constant impedance, and transformers are modeled as constant impedance plus an ideal transformer, as shown in Figure 3.6.

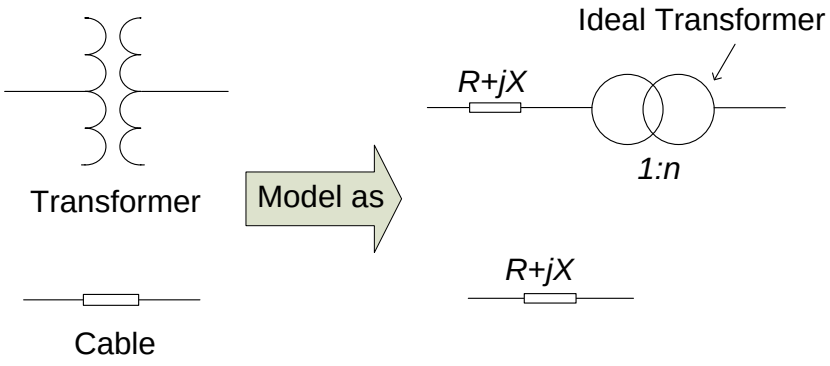

Figure 3.6 Representation of cables and transformers

(3) Template scaling rules. Template scaling rules are developed from the load composition data (section 2.3.4) and the data of sample facilities. Worth of mention is that the newer mills and older mills should use different load composition data, as shown below in Figure 3.2.

Table 3.2 Summary of Load Composition

Load types	Type 1-Newer mills	Type 2-Older mills
Induction Motor	77.7%	53.3%
VFD	4.3%	0
DC Drives	0	16.4%
Synchronous motor	0	12.3%
Static loads	18.0%	18.0%

Based on the above consideration, two set of template scaling rules are developed. Table 3.3 presents the template scaling rules for newer Kraft paper mills (Type 1). Table 3.4 presents the template scaling rules for older Kraft paper mills (Type 2). Due to page limitation, only the newer mills (type 1) will be adopted as an example to demonstrate the use of template scaling rules in the next section.

Table 3.3 Template scaling rules for newer Kraft paper mills (Type 1)

#	Process	Rated loads, % of total load	480V induction motor, % of total load		2.4kV induction motor, % of total load		4.16kV induction motor, % of total load		Static loads, % of total load
			None	VFD	None	VFD	None	VFD	None
1	Wood Preparation	4.89	2.17	0.25	0	0	2.22	0	0.25
2	Chemical	11.94	4.51	0	0	0	4.05	0	3.39

	Recovery								
3	Power Plant	3.75	1.24	0	0	0	2.51	0	0
4	Extraction of Pulp	19.79	0	0	6.84	0.16	8.97	0.29	3.36
5	Fibreline	12.10	3.48	0.50	3.77	0.17	4.35	0	0
6	Paper Machine	22.90	6.00	1.00	2.95	0.33	10.53	0	2.10
7	Effluent Treatment	7.98	2.75	0.50	0	0	4.57	0.17	0
8	PCC Plant	2.16	2.16	0	0	0	0	0	0
9	Chemical Plant	7.58	0.80	0	0	0	0.28	0	6.50
10	Other	6.90	2.36	0	0	0	1.99	0	2.55
	Total	100.00	25.47	2.25	13.55	0.66	39.45	0.46	18.15

Table 3.4 Template scaling rules for older Kraft paper mills (Type 2)

#	Process	Rated loads (Real), % of total load	480V induction motor,% of total load	4.16kV induction motor,% of total load	480V synchronous motor,% of total load	4.16kV synchronous motor, % of total load	480V DC motor, % of total load	Static loads,% of total load
1	Wood Preparation	6.61	1.92	1.73	1.22	0	1.5	0.24
2	Chemical Recovery	9.74	3.94	3.53	0	0	0	2.27
3	Power Plant	6.08	1.09	2.18	0	0	1.6	1.21
4	Extraction of Pulp	19.48	0	6.41	1.13	4.29	4.4	3.25
5	Fibreline	16.3	3.04	3.47	1.41	4.29	2.2	1.89
6	Paper Machine	20.52	5.25	8.34	0	0	4.9	2.03
7	Effluent Treatment	7.94	2.41	3.73	0	0	1.8	0
8	PCC Plant	1.82	1.82	0	0	0	0	0
9	Chemical Plant	5.23	0.71	0.24	0	0	0	4.28
10	Other	6.28	2.07	1.74	0	0	0	2.46
	Total	100	22.25	31.37	3.76	8.58	16.4	17.6

3.2.2 Modeling a Kraft Paper Mill with the Template

Now that the construction of the template is complete, the next procedure is to apply the template for modeling the facility of interest. According to the template-based load modeling method, the modeling of a specific Kraft paper mill has two steps (Figure 3.7) as follows:

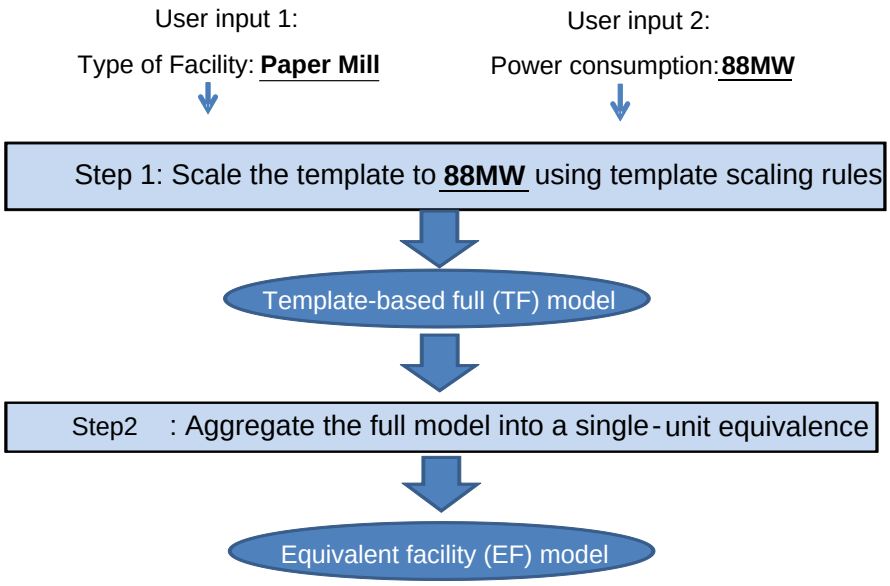

Figure 3.7 Two steps for modeling a Kraft paper mill

Step 1: Scale the template up or down to the given size (88MW in this example). The use of template scaling rules is simple: scaling the motors and loads up or down, and keeping the series impedance (i.e. cables and transformers) unchanged.

After this step, a template-based full model can be obtained; one can create a case file to represent this systematic model in the ETAP program, as shown in Figure

3.8. Each sub-system represents a small network of motors and loads. For example, Figure 3.9 presents the details inside a sub-system (process#1: wood preparation). The loads and motors distributed in each process have been summarized in Table 3.5. Due to page limitation, the size and typical parameters of motors are not listed here.

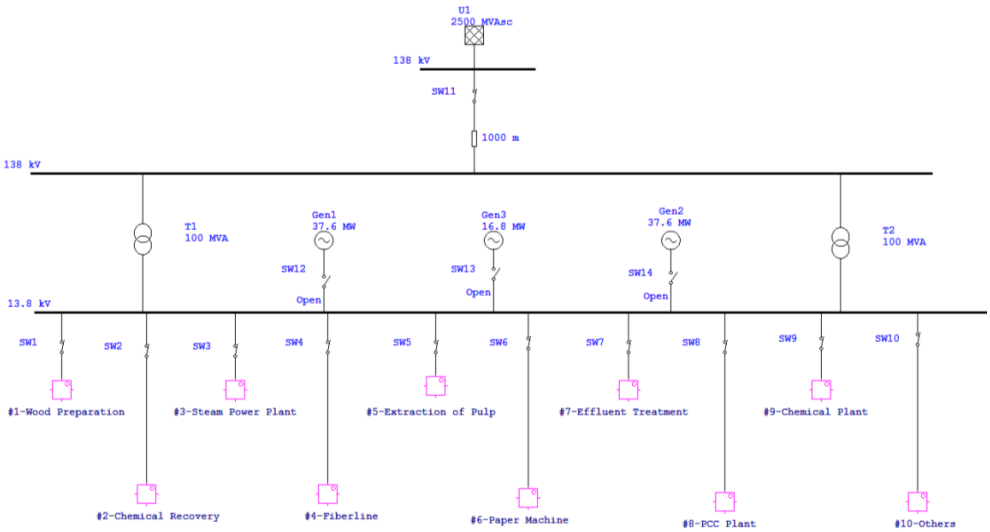

Figure 3.8 One-line diagram for the template-based full model

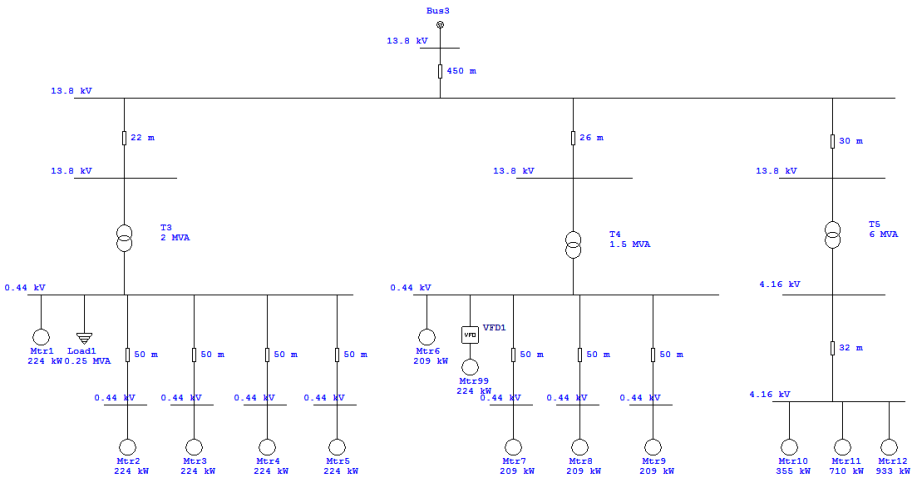

Figure 3.9 One-line diagram for one of the sub-system (Process #1-Wood preparation)

Table 3.5 Case-specific Template for 88MW Kraft paper mill (Type 1), in MW

#	Process	Rated loads, MW	480V induction motor, MW		2.4kV induction motor, MW		4.16kV induction motor, MW		Static loads, MW
			None	VFD	None	VFD	None	VFD	None
1	Wood Preparation	4.30	1.91	0.22	0	0	1.95	0	0.22
2	Chemical Recovery	10.51	3.97	0	0	0	3.56	0	2.98
3	Power Plant	3.30	1.09	0	0	0	2.21	0	0
4	Extraction of Pulp	17.42	0.00	0	6.02	0.14	7.89	0.26	2.96
5	Fibreline	10.65	3.06	0.44	3.32	0.15	3.83	0	0
6	Paper Machine	20.15	5.28	0.88	2.60	0.29	9.27	0	1.85
7	Effluent Treatment	7.02	2.42	0.44	0	0	4.02	0.15	0
8	PCC Plant	1.90	1.90	0	0	0	0	0	0
9	Chem. Plant	6.67	0.70	0	0	0	0.25	0	5.72
10	Other	6.07	2.08	0	0	0	1.75	0	2.24
	Total	88.00	22.41	1.98	11.92	0.58	34.72	0.40	15.97

The full model could contain hundreds of motors and loads, and is not computationally feasible for large scale system simulation. The next step is how to reduce this full model.

Step 2: Aggregate the template-based full model into a single unit-equivalence. In this step, using the "bottom-up" approach, one can be apply the aggregation techniques (details in section 3.1.2) on motors and loads from the bottom level up to the top, until single-unit equivalence is obtained. The single-unit equivalence is called "Equivalent Facility (EF) model" in this method. The EF model consists of

one lumped induction motor and one lumped static load, as shown in Figure 3.10. This EF model is computationally feasible for large scale system simulation. The parameters for the aggregated motor and static load are summarized in Table 3.6; the parameters of the circuit model are illustrated in Figure 3.11.

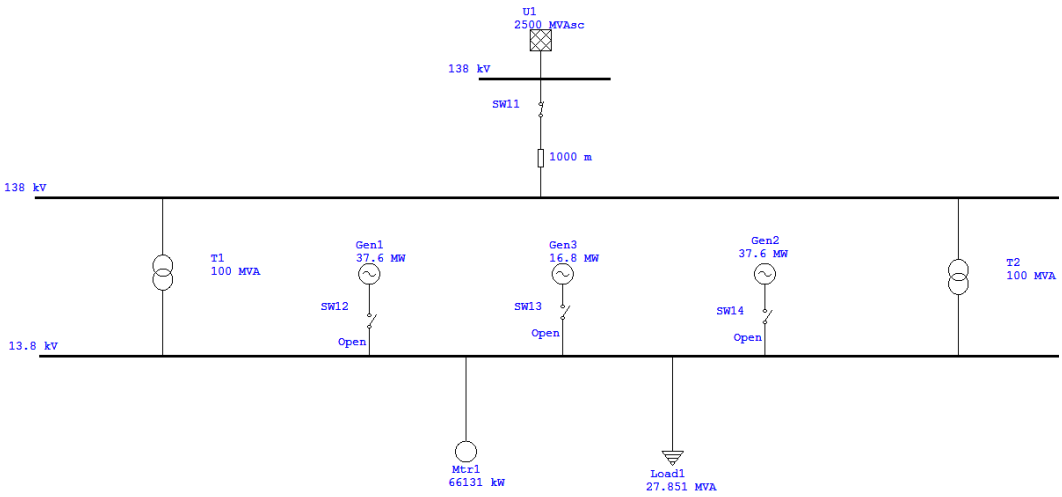

Figure 3.10 Equivalent facility (EF) model of newer Kraft paper mills (Type 1)

Table 3.6 Parameters of Equivalent facility (EF) model

	Induction motor	Static load
Rated MW	66.13	24.22
Rated MVA	87.26	27.85
Rated kV	13.8	13.8
Power Factor (100%)	0.797	0.869
Slip	1.73	--
Rated RPM	3538	--
Full-load current (A)	3651	--
Inertia constant (s)	2.02	--
Mechanical Loads	T_m(%)=100*ω^2	--
R_s (%)	3.19	--
X_s (%)	13.92	--
X_m (%)	242.86	--
X_r (%)	17.28	--
R_r (%)	1.757	--

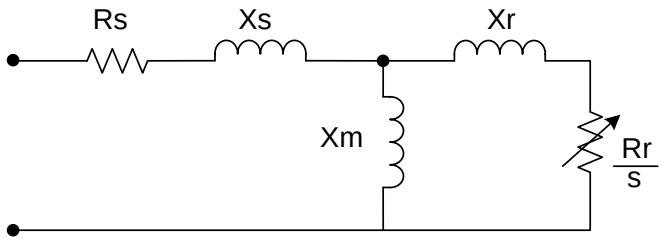

Figure 3.11 Circuit model of an induction motor

Worth of mention is that the established EF model can be readily imported into the commercial simulation programs such as PSS/E. The static load can be implemented with the polynomial load characteristics; the lumped induction motor can be implemented by the CIM series induction motor load models [47].

Since some paper mills may or may not have co-generation, the generators in EF model can be set as either in-service or out-of-service per the specific facility configuration. The number of co-generating units can also be modified manually per the situation of the real facility.

3.3 Simulation Results

The objective of this section is to demonstrate the accuracy and usefulness of the established load model through ETAP simulation. For this purpose, two sets of comparison studies are made as follows. The dynamic responses of these models to system disturbances (such as a three-phase fault) are compared and analyzed.

(1) Compare the template-based equivalent facility (EF) model and the template-based full (TF) model;

(2) Compare between the real facility, equivalent facility (EF) model, and WECC interim guideline model.

1) Comparison between EF model and TF model

A three-phase fault is applied at the 138-kV Utility Bus, for both TF model and EF model. The fault occurs at 1.0 sec and clears at 1.25 sec with total simulation time equal to 5 sec. The simulation is conducted using the ETAP program. The dynamic responses of the two models for this event are presented in Figure 3.12.

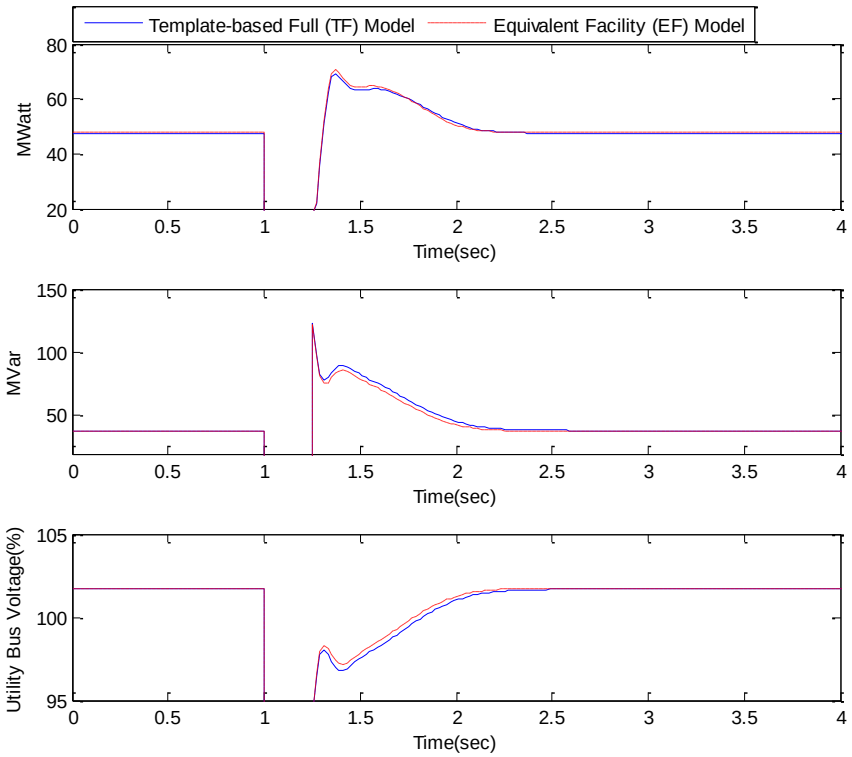

Figure 3.12 Active power, reactive power, and voltage responses at transformer T1 for template-based full model and equivalent facility model

It’s observed that there is a good agreement between the dynamic responses of the two template-based models. This agreement confirms the accuracy and effectiveness of model aggregation techniques as described previously.

2) Comparison between real facility, EF model and WECC guideline model

Further, in order to compare the proposed models against the existing models, we made a comparison between Real Facility, EF Model, and WECC Guideline Model. The description of those models is shown as follows.

- **Real Facility (Benchmark Case)** (80% induction motor, 20% static loads): the detailed model for the Brazilian Kraft paper mills, which is newly upgraded in 2006.
- **WECC guideline model** (20% induction motor, 80% ZIP static loads): an interim load model recommended by WECC starting from 2001 [7]. Typical motor data is used to construct the model.
- **Template-based Equivalent Facility (EF) Model** (82% induction motor, 18% static loads): the model derived from the template, the structure of which is as shown in Figure 3.10.

As seen in Figure 3.13, there is a good agreement in dynamic response between

the EF Model and the real facility. However, the WECC guideline model fails to capture the dynamic response of the real facility adequately, especially the phenomenon of delayed voltage recovery.

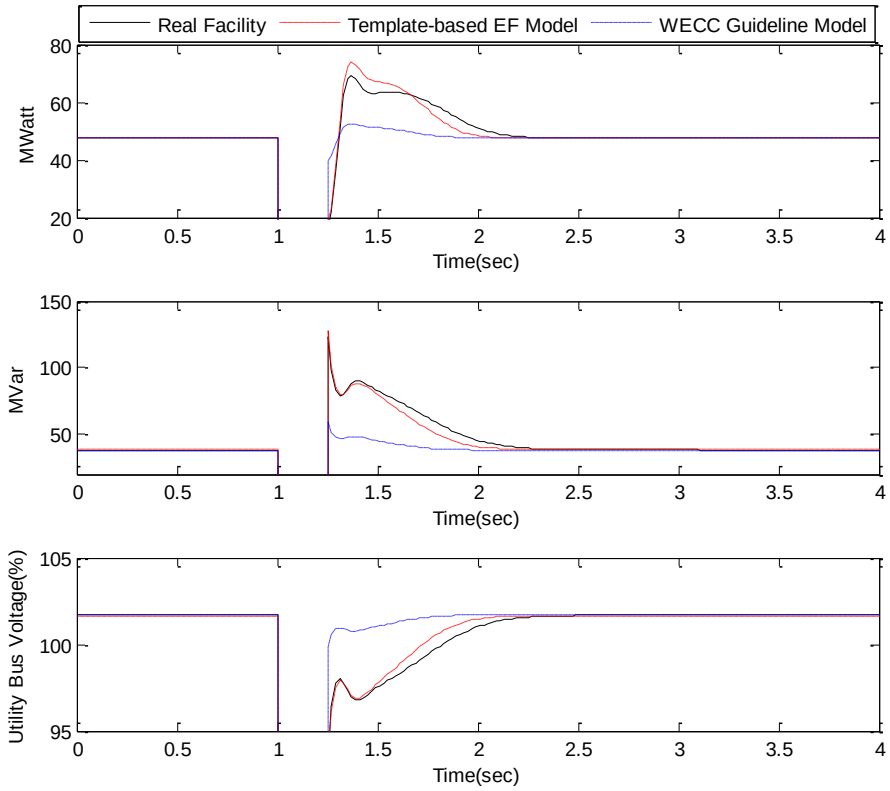

Figure 3.13 Active power, reactive power, and voltage responses at Utility main bus for real facility, template-based EF model, and WECC guideline model

Table 3.7 explains the reason why WECC guideline model has such as big error. As seen, the percentage of motor loads in WECC guideline model is only 1/4 of the real facility. In comparison, the percentage of motor loads in EF model is very accurate related to the real facility. In summary, inaccurate percentage of motor composition is the major errors source for the WECC guideline model.

Table 3.7 Comparison of load composition

	Real Facility	EF model	WECC model
Motor loads	80%	82%	20%
Static loads	20%	18%	80%

In conclusion, the simulation results reveal that the proposed equivalent facility (EF) model can accurately represent the full model. It's also observed that EF model is more accurate than the WECC guideline model.

Chapter 4

Modeling and Aggregating DC Drive Loads

DC drive loads have a large population in industrial plants, especially in paper mills. Although DC drives are getting less popular than AC drives, DC drives are still very common in today's paper manufacturing industry, due to their large base number [48]. Therefore, the objective of this chapter is to discuss the issue of modeling and aggregating DC motor drives for power system stability studies. This chapter mainly investigates three issues: tripping criterions for DC drives, equivalent model for ride-through DC drives, and model aggregation techniques.

4.1 Introduction

Traditionally, DC drives are treated simply as transparent devices[2] for the dynamic performance simulation in most of the commercialized simulation software (i.e. ETAP and DIgSILENT) [34]. This is because DC drives are very sensitive to voltage disturbance, and are very likely to be tripped, subjected to voltage disturbance.

However, it's inappropriate to treat DC drives simply as transparent devices. The

[2] In ETAP, "transparent devices" means the load that is tripped for the during-fault period, and recovers to the initial power consumption immediately after the fault clears.

behavior of DC drives can be classified into two scenarios, subjected to voltage sags. As seen in Figure 4.1, if the voltage sag is severe, DC drives will be tripped and should not be included in the dynamic simulation program. Otherwise, if the voltage sag is mild, DC drives will ride through the fault and should be included in the dynamic simulation program. Modeling of DC drives should consider both two scenarios.

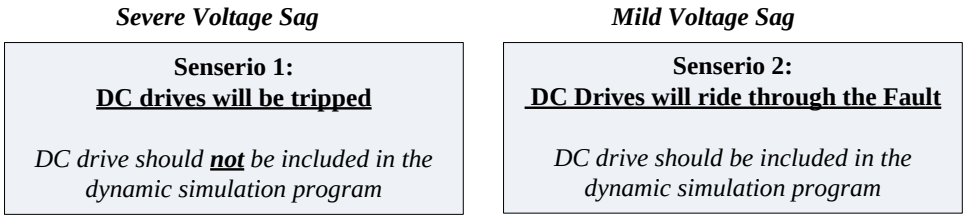

Figure 4.1 Two scenarios: DC drives responding to voltage sags

The objective of this chapter is to establish a valid load model and an aggregation technique of DC drive loads for power system dynamic performance studies. The following context is organized as follows. Firstly, the criterion for determining whether a given voltage sag will trip DC drives is discussed. Secondly, the issue of modeling ride-through DC drives as the standard transfer function model. Thirdly, techniques for aggregating DC drive loads and incorporating cables and transformers are discussed.

4.2 Trip-off Criterion for DC Drives

This sub-section discusses the criterion for determining if a given voltage sag will trip DC drives. Firstly, we present a survey on the threshold settings of DC drives' under-voltage protection. Then, a DC drive trip curve based on the survey results is proposed. Finally, a general procedure for dynamic simulation of DC drives is presented.

4.2.1 Threshold Settings of DC Drives' Undervoltage Protection

Voltage sags are normally characterized by depth and duration. In addition, other parameters such as the imbalance, non-sinusoidal wave shapes, and phase-angle jump also have an impact on DC motor's dynamic response [49]. Nevertheless, only the positive fundamental network is strictly considered, for the purpose of power system dynamic studies (i.e., PSS/E) [50].

Therefore, this project only considers the balanced fault and investigates the impact of depth and duration on DC drives. In addition, for the sake of simplicity, the shape of voltage sags is considered to be rectangular in this project. This is because the influence of the voltage sag fall and rise time on DC drive behavior is very small and can be omitted [49].

The below four literature surveys have shown the sensitivity of DC drives

subjected to voltage sags. The data sources cited here include product manuals of industrial DC drives, technical and academic publications, and EPRI field measurement data.

(1) Most of DC drive manufacturers only indicate the voltage tolerance in terms of depth. For example, For ABB's medium-voltage DC drive (model number DSC 800), voltage tolerance is indicated as -15 %/+10% [51].

(2) Reference [35] points out that Many DC drives are generally set to trip if the voltage magnitude of one, two, or all of the supply phases sags below 90%. DC drives with regenerative bridges, are especially sensitive to imbalance, and will trip if one phase drops as little as 10% for 1-2 cycles.

(3) Reference [52] observes that DC drives are very sensitive to voltage drops, and will trip when subjected to voltage drops to only 88% of nominal. There may be 5 to 10 trips per year based on the utility average EPRI study.

(4) Reference [53] presents field measurement conducted in a newspaper facility in Baltimore. The results are shown below. A sag generator is used to create sags of different depth and duration.

Table 4.1 Response of DC drives to voltage sags

Depth \ Duration(cycles)	4	5	6	10	15	20	30
90%							
80%							
70%							
60%							

DC drive not tripped DC drive tripped

4.2.2 DC Drive Trip Curve

Based on the survey in the last sub-section, a recommended voltage tolerance characteristic curve, as seen in Figure 4.2, is proposed to represent the sensitivity of DC drive to voltage sags.

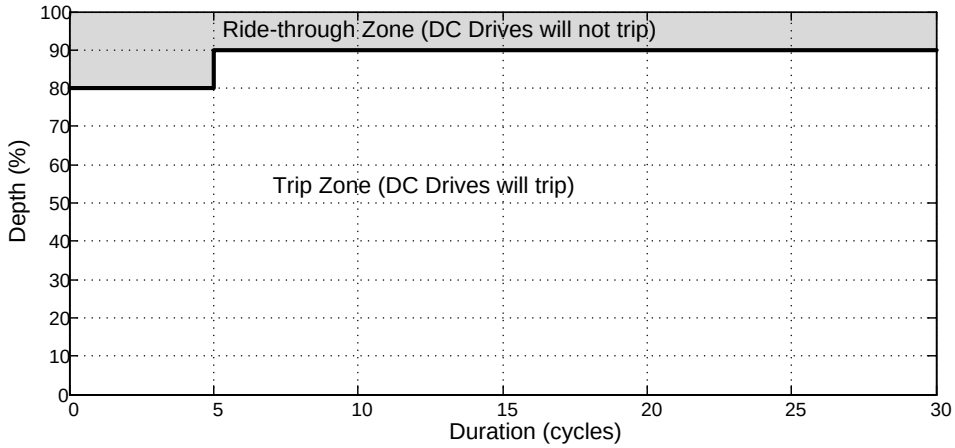

Figure 4.2 DC drive trip curve for voltage sags due to three-phase balanced faults (recommended)

The voltage tolerance characteristic curve is normally expressed in terms of one pair of voltage sag magnitude/duration values. If the sag characteristic (magnitude,

duration) is above the curve, DC drives will not trip and shall be included in the dynamic load model; otherwise, if the sag characteristic (magnitude, duration) is below the curve, DC drives will be tripped and won't be included in the dynamic load model.

The curve in Figure 4.2 is meaningful in determining if a given voltage sag will trip DC drives. This curve shows that for voltage sags below 80% for duration less than 5 cycles (83ms), or voltage sags below 90% for duration over 5 cycles (83ms), DC drives will trip. Also, it's observed that DC drives are more sensitive and vulnerable to voltage sags as compared to the DC drive trip curves in reference [54]. This is because DC drives don't have any DC-link capacitors that function as electrical energy storage devices.

4.2.3 General Procedures for DC Drive Simulation

As seen below are a list of recommended procedures for including DC drive loads in power system dynamic simulation.

Step1: Conduct a three-phase short-circuit study on the study system if the outage event of interest involves a short-circuit fault. In this study, the DC drives can be omitted since they have little contributions to the fault current. This study will

yield a voltage sag magnitude at the DC drive's location.

Step 2: Check the relay setting involved in clearing the fault. This setting will provide the sag duration value for the outage event.

Step 3: The resulting sag magnitude and duration values are then compared with the DC drive trip curve. If the point is below the curve, the DC drive will trip and they shall not be modeled in dynamic studies.

Step 4: If the point is above the trip curve, DC drives will ride through the fault. In this case, a detailed DC drive model may be needed for dynamic simulation. Such a dynamic model will be developed and presented in the next section. The technique to aggregate these models is also discussed.

4.3 Modeling Ride-Through DC Drives

In case of mild voltage sags, the DC drive may ride through the fault and must be included in dynamic simulation model. This section discusses the issue of modeling ride-through DC drives.

4.3.1 Description of DC Drives Adopted in This Thesis

A typical DC drive consists of a power electronic converter and a DC motor in series with a smoothing inductor. For most industrial applications, the power electronic converter is a three-phase full-bridge thyristor rectifier as seen in Figure 4.3. The structure of DC Drives is based on P.C. Sen [55], P. C. Krause [56], and S. Zhang [57].

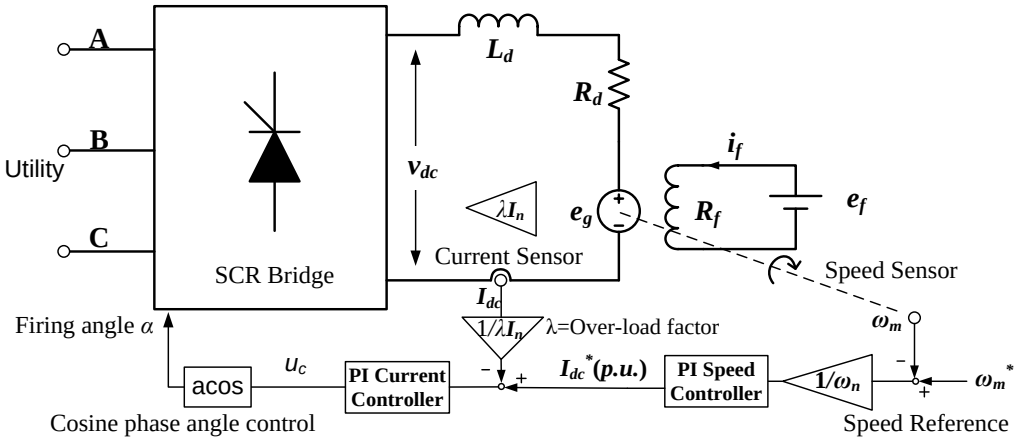

Figure 4.3 Schematic diagram of typical DC drives

Double-loop speed control scheme is the most common method used to adjust the speed of DC motors. Figure 4.3 shows the schematic diagram of a double-loop speed DC drive control system. The control system consists of a PI speed controller (ASR) and a PI current controller (ACR). The ASR outputs the armature current reference i_d^* used by the current controller in order to obtain the electromagnetic torque needed to reach the desired speed ω_m^*. The ACR controls the armature current i_d by computing the appropriate thyristor firing angle α,

which generates the rectifier output voltage v_{dc} needed to obtain the desired armature current i_d and thus the desired electromagnetic torque. Normally, cosine control of phase angle (the procedure of "acos") is used to maintain a linear relationship between control signal u_c and the output voltage of SCR bridge rectifier v_{dc}.

4.3.2 Response of Ride-Through DC Drives

To model ride-through DC drives, we need to simulate how ride-through DC drives respond to voltage drops. The parameters for simulating DC drives are taken from the textbook by N. Hong [58] as shown in Table 4.2. The simulation is conducted using *Simulink* software (*SimPowerSystem* toolbox) based on a detailed DC drive model as described in the previous subsection. This detailed model includes the operation of switching devices in the rectifier, and the dynamics of DC motors and circuits. In the simulation study, a three-phase balanced voltage sag (depth: 90%, duration: 0.25 sec) is applied to the utility side of the drive at t=0.5 sec.

Table 4.2 Simulation parameters for DC drives

Rated Power (HP)	40	Commutation Inductance L_c(H)	0
Nominal Voltage (V)	220	Armature Resistance R_d (Ω)	0.21
Nominal Current (A)	136	Smoothing Inductance L_d (mH)	20
Nominal Speed (rpm)	1500	Mutual Inductance L_{df} (H)	2.621
Motor Inertia (kg·m^2)	0.57	Field Current I_f (A)	1.5
Controller parameter	PI Speed controller: K_p=10.5, K_i=120.5		

	PI Current controller: K_p=2.48, K_i=37.3 Overload factor λ=1.5
Mechanical Load	TL=239.36N·m
Base Case Status	46.0kW+j27.2kVar, Supply voltage: 208V(L-L), 1500rpm (full speed)

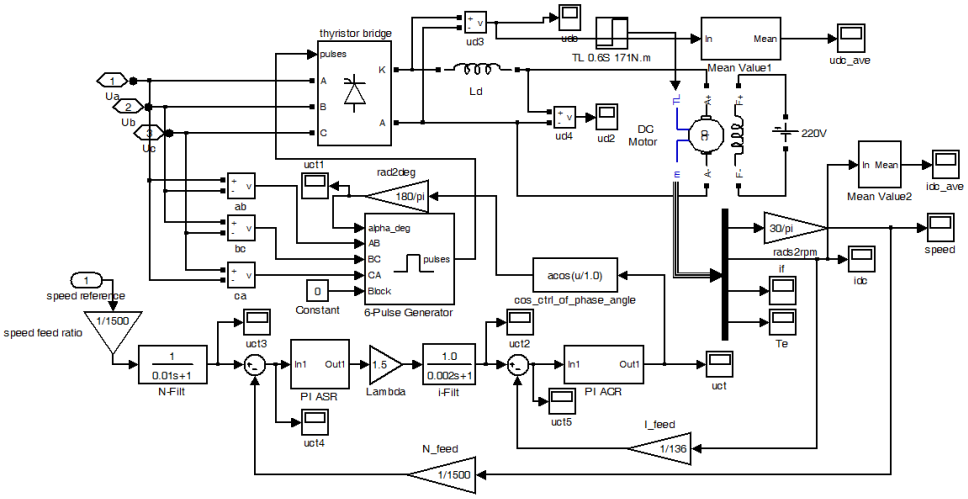

Figure 4.4 Simulation block diagram of DC drives (Built in Simulink)

The simulation block diagram of DC drives is presented in Figure 4.4. The simulation results are shown in Figure 4.5 and Figure 4.6. Figure 4.5 presents the waveforms and RMS values for utility-side variables including line-to-ground voltage V_{lg}, active power P, and reactive power Q. Figure 4.6 presents the waveforms and RMS values for DC-side variables, including output DC voltage of bridge converter v_{dc}, DC motor armature current i_{dc} and Motor generated voltage e_g. It's observed that it takes more than ten cycles for a DC drive to reach its post-fault steady state. Therefore, there's a strong reason to represent DC drives with dynamic characteristics.

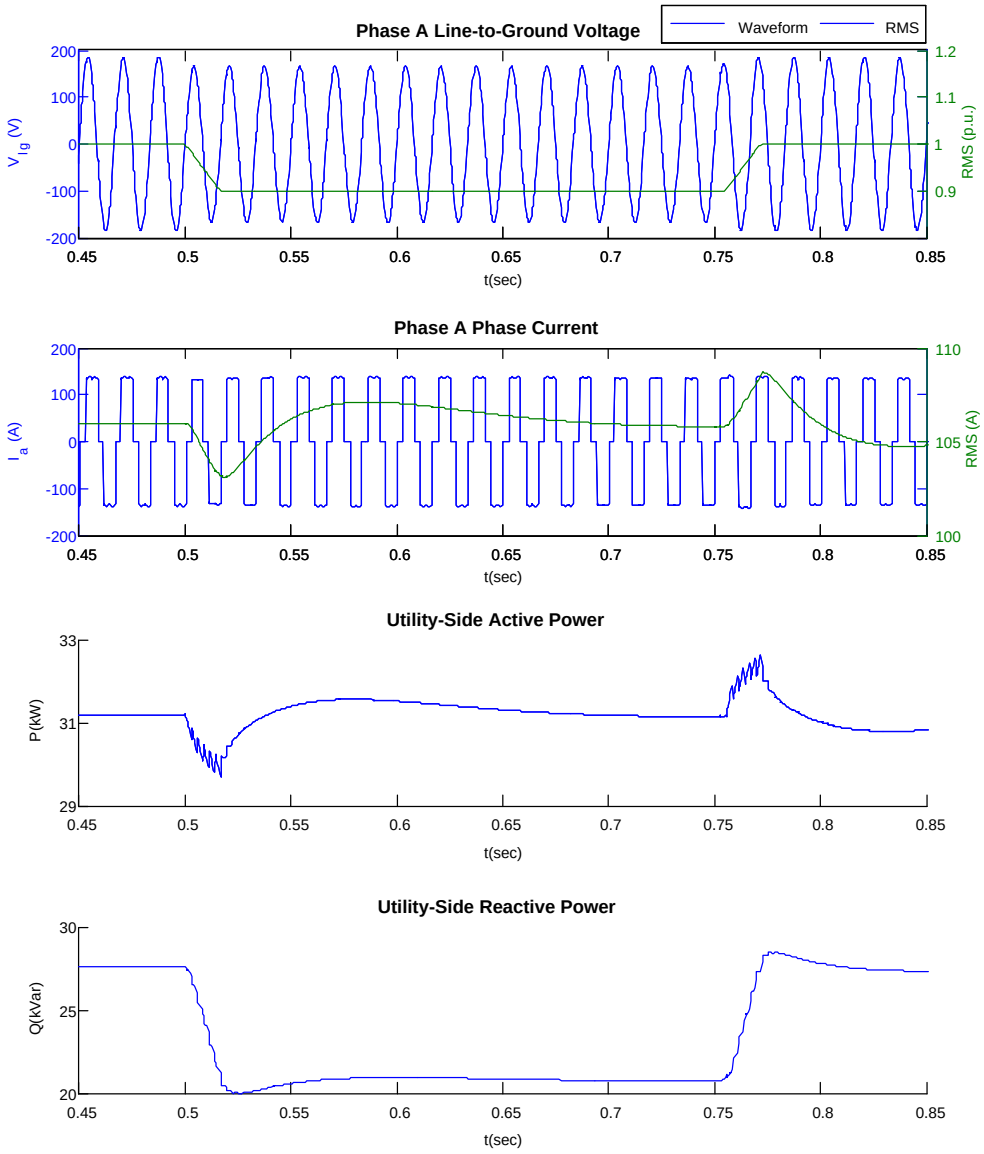

Figure 4.5 Utility-side waveforms and RMS values

Note that in this case of 5% voltage drop, the variation of AC/DC side current (RMS or averaged values) is in a very small range (around 5%). Also note that the disturbance of averaged output V_{dc} is less than 5%. As a result, it is permissible to use the small-signal model to characterize the system dynamics.

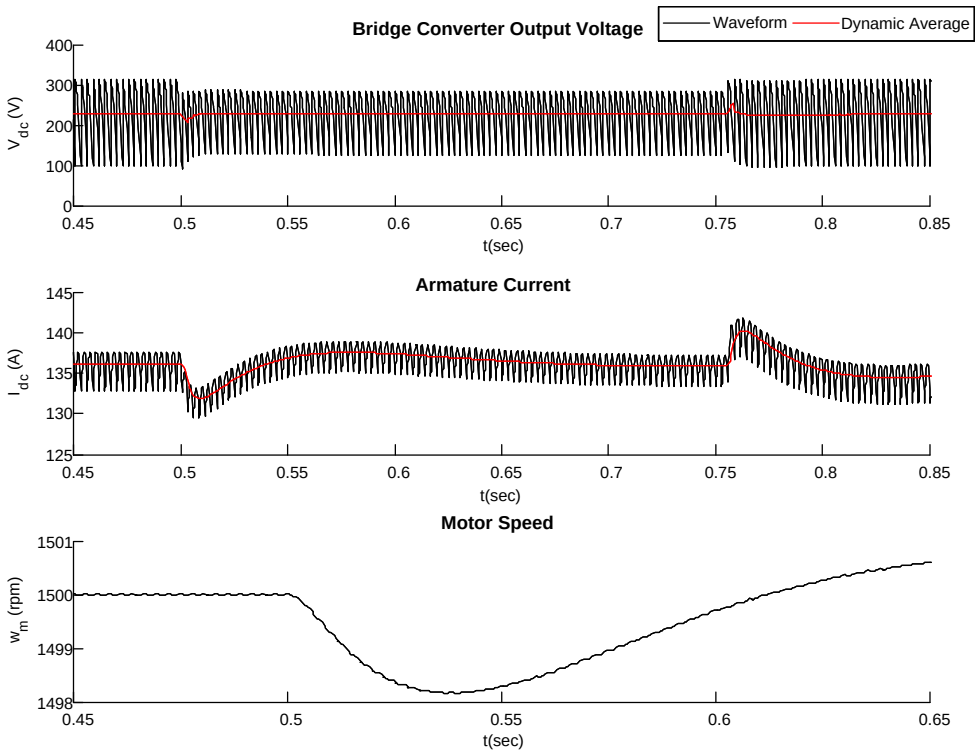

Figure 4.6 DC-side waveforms and dynamic-averaging values

It's observed that there are some the ripples (within one cycle at t=0.5sec) in the active and reactive power. Obviously, the ripples are not related to system dynamics, but caused by the distortion of utility-side current waveforms at the fault time. This is because the active and reactive power is calculated with a running window over one cycle of the fundamental frequency, and will be discontinuous at the edge of the current waveform.

4.3.3 Equivalent Dynamic Model for DC Drives

In this subsection, an equivalent model is proposed to simulate the DC drives for power system dynamic performance studies. The proposed model is based on the

three-phase full-converter DC drive (Figure 4.7) which is widely used for adjustable speed applications in the industry. This type of DC drives is normally equipped with speed-current double loop control systems as shown in Figure 4.8 [57].

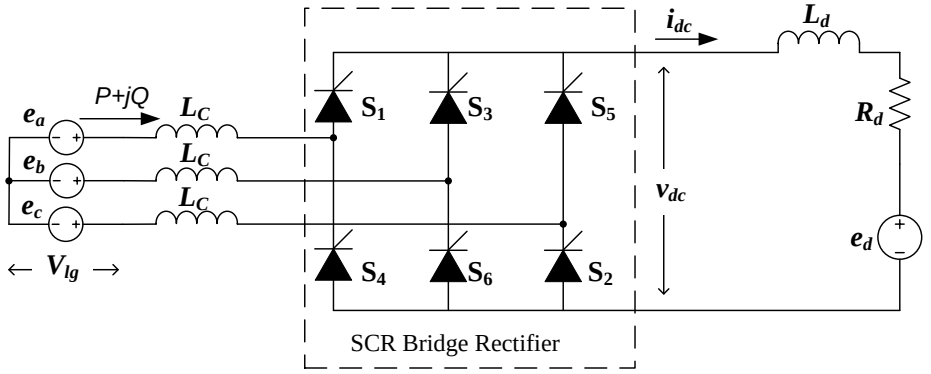

Figure 4.7 Full-converter DC drive (two quadrants) with line commutation

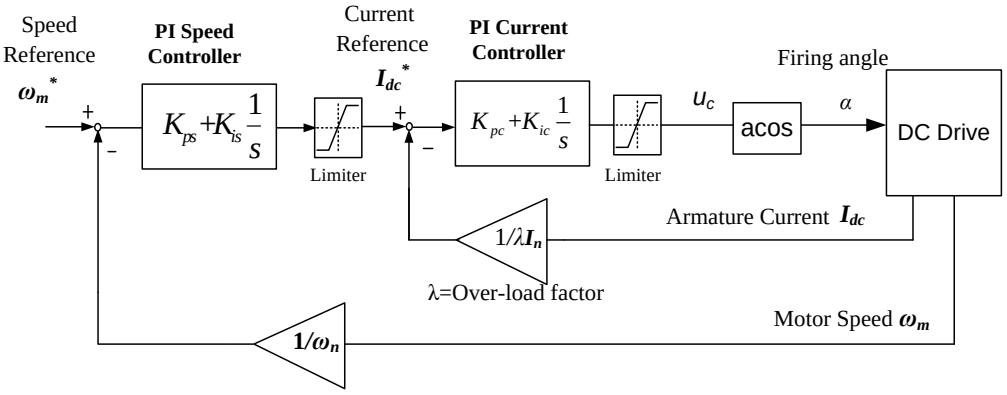

Figure 4.8 Control system blocks for PI current controller

An equivalent dynamic model of the DC drive can be established from the electrical circuit equations, the control system dynamics, and the mechanical dynamics of the DC motor. The derivation of the model is presented with details

in Appendix B. The model structure is shown in Figure 4.9. This model is based on an average-value model (AVM) and can simulate a DC drive under symmetric operation condition, i.e. a three-phase symmetric fault.

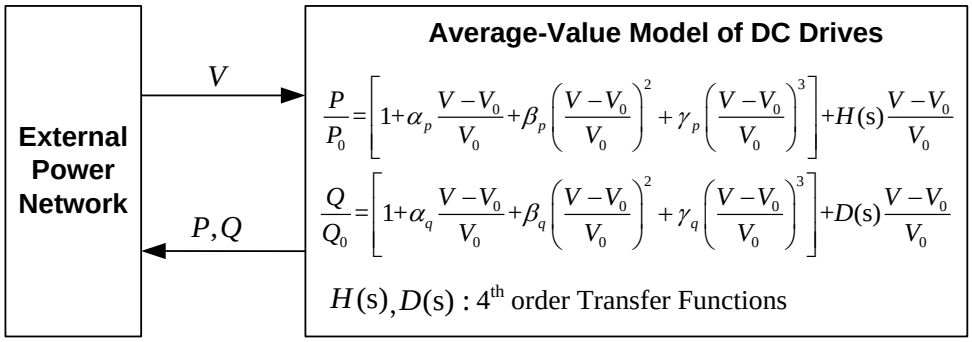

Figure 4.9 Equivalent model of DC drives for power system dynamic studies (Model derivation is presented in Appendix B)

The input variable of the model is the bus voltage V (line-to-ground) at the locations of the DC drive; the output variables are $P+jQ$, the active and reactive power absorbed by the DC drive. P_0, Q_0, and V_0 are the active power, reactive power, and bus voltage at the initial condition. $H(s)$, $D(s)$ are the fourth-order transfer functions that describe the dynamic characteristics of the DC drive. The complete expression of the model is given as follows,

$$\frac{P}{P_0}=1+\left[\alpha_p\frac{V-V_0}{V_0}+\beta_p\left(\frac{V-V_0}{V_0}\right)^2+\gamma_p\left(\frac{V-V_0}{V_0}\right)^3\right]+H(s)\frac{V-V_0}{V_0} \quad (4.1)$$

$$\frac{Q}{Q_0}=1+\left[\alpha_q\frac{V-V_0}{V_0}+\beta_q\left(\frac{V-V_0}{V_0}\right)^2+\gamma_q\left(\frac{V-V_0}{V_0}\right)^3\right]+D(s)\frac{V-V_0}{V_0} \quad (4.2)$$

where,

$$\alpha_p=0,\ \beta_p=0,\ \text{and}\ \gamma_p=0 \quad (4.3)$$

$$\alpha_q = \frac{S_0^{\,2}}{Q_0^{\,2}}, \quad \beta_q = -0.5\frac{S_0^{\,2}}{Q_0^{\,2}}\frac{P_0^{\,2}}{Q_0^{\,2}}, \text{ and } \gamma_q = 0.5\frac{S_0^{\,4}}{Q_0^{\,4}}\frac{P_0^{\,2}}{Q_0^{\,2}} \tag{4.4}$$

$$H(\mathrm{s}) = \frac{s^4 L_d + s^3\left(R_d + V_{dc0}/I_{dc0}\right) + s^2 K_E^{\,2} J^{-1}}{s^4 L_d + s^3\left(K_{pc}R_{eq} + R_d\right) + s^2\left(K_{eq1}R_{eq} + K_E^{\,2}J^{-1}\right) + sK_{eq2}R_{eq} + K_{eq3}R_{eq}} \tag{4.5}$$

$$D(s) = -\frac{P_0^{\,2}}{Q_0^{\,2}}\frac{s^4 L_d + s^3\left[R_d - Q_0^{\,2}V_{dc0}/P_0^{\,2}I_{dc0}\right] + }{s^4 L_d + s^3\left(K_{pc}R_{eq} + R_d\right) + } \rightarrow$$

$$\leftarrow \frac{+s^2 K_E^{\,2} J^{-1}}{+s^2\left(K_{eq1}R_{eq} + K_E^{\,2}J^{-1}\right) + sK_{eq2}R_{eq} + K_{eq3}R_{eq}} \tag{4.6}$$

$$R_{eq} = \frac{3\sqrt{6}}{\pi}\frac{V_{\mathrm{lg0}}}{\lambda I_n}, \quad K_{eq1} = K_{ic} + \frac{\lambda K_E I_n K_{pc} K_{ps}}{J\omega_n} \tag{4.7}$$

$$K_{eq2} = \frac{\lambda I_n K_E}{J\omega_n}\left(K_{ic}K_{ps} + K_{pc}K_{is}\right), \quad K_{eq3} = \frac{\lambda K_E I_n K_{ic} K_{is}}{J\omega_n} \tag{4.8}$$

Input data that are needed to construct the equivalent model are presented as follows:

- V_{lg0} - Utility bus voltage (base case), phase-to-ground
- P_0 - Active power consumption of the drive (base case)
- Q_0 - *R*eactive power consumption of the drive (base case)
- P_n - Rated Motor Power
- I_n - Nominal DC-motor armature current
- ω_n - Nominal motor speed
- R_d - DC armature circuit resistance (total)
- L_d - DC armature circuit inductance (total)
- K_{pc} - Proportional constant of PI current controller
- K_{ic} - Integral constant of PI current controller
- K_{ps} - Proportional constant of PI speed controller
- K_{is} - Integral constant of PI speed controller
- λ - Over-loading factor

K_E - Voltage constant of the DC motor

J - Moment of inertia of the DC motor

The DC-side state variables for initial condition can be obtained from those input data, as described below [55, 59].

$$I_{dc0} \approx \sqrt{\frac{3}{2}} I_{ac0} = \sqrt{\frac{3}{2}} \frac{\sqrt{P_0^{\,2} + Q_0^{\,2}}}{3V_{\lg 0}} \tag{4.9}$$

$$V_{dc0} = V_{\lg 0} \cdot \frac{3\sqrt{6}}{\pi} \frac{P_0}{\sqrt{P_0^{\,2} + Q_0^{\,2}}} \tag{4.10}$$

Note that the saturation effect of the limiters in the controller blocks is disregarded. This is because only small voltage disturbances are considered in this model. In addition, the commutating inductance L_C resulted from cables and transformers is disregarded. This is to avoid repeated calculation of the network impedance because the commutation inductance of each DC drive involves the Thevenin equivalence of the rest of the distribution network. Instead, the commutation inductance is considered as series impedance, the effect of which is discussed separately in the model aggregation sections.

4.3.4 Summary of Modeling Requirements and Procedures

This subsection summaries the general requirements and procedures for constructing the equivalent dynamic model of DC drives.

Input data requirement:

Input data required to construct the DC drive equivalent model is given by Table 4.3. Among the required input, the parameters V_{lg0}, P_0, and Q_0 are determined by the operating conditions of the drives. The initial conditions can be taken from either preset values, or from the load flow results of an actual network. Typical or sample values may be used if any of the drive parameter is unknown.

Table 4.3 Input data and typical values

Symbol	Parameters	Typical or Sample Value
V_{lg0}	Utility-side bus voltage at the drive terminal, phase-to-ground (base case)	User-defined (in V rms), or taken from load flow results (base-case)
P_0, Q_0	*R*eal and reactive power consumption of the drive (base case)	User-defined (in kW) or taken from load flow results (base-case)
P_n	Motor HP (horsepower)	User-defined (in HP)
I_n	Nominal DC-motor armature current	User-defined (in A)
ω_n	Nominal motor speed	User-defined (in RPM)
R_d	DC armature circuit resistance (total)	Typical value is given by Figure 4.10
L_d	DC armature circuit inductance (total), including the smoothing inductance and the motor inductance	$L_d \approx 0.693\frac{V_{lg0}}{I_n \times 5\%} = 13.8\frac{V_{lg0}}{I_n}$ (mH)
K_{pc}	Proportional constant of PI current controller	10.5 (sample)
K_{ic}	Integral constant of PI current controller	120.5 (sample)
K_{ps}	Proportional constant of PI speed controller	2.48 (sample)
K_{is}	Integral constant of PI speed controller	37.3 (sample)
λ	Over-loading factor	Typical value 1.5

K_E	Voltage constant of the DC motor	$K_E = K_T \approx \frac{P_n}{I_n \omega_n}$ (V•sec)
J	Moment of inertia of the DC motor	$J = 6.79 \times 10^4 \frac{H(\text{in sec}) \times P_n(\text{in HP})}{\omega_n{}^2(\text{in rpm})}$, in $\text{kg} \cdot \text{m}^2$ Typical inertia constant of DC motors: $H \approx 0.5$sec [60]

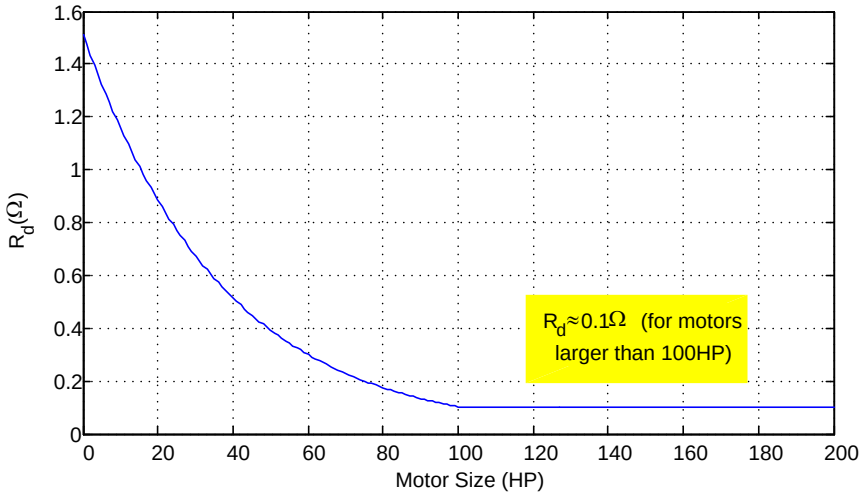

Figure 4.10 Typical value of DC armature circuit resistance (R_d)

Some parameters of the equivalent model are not given in Table 4.3, and can be calculated with following equations

$$I_{dc0} \approx \sqrt{\frac{3}{2}} I_{ac0} = \sqrt{\frac{3}{2}} \frac{\sqrt{P_0{}^2 + Q_0{}^2}}{3V_{\text{lg}0}} \tag{4.11}$$

$$V_{dc0} = V_{\text{lg}0} \cdot 2.4495 \frac{P_0}{\sqrt{P_0{}^2 + Q_0{}^2}} \tag{4.12}$$

$$R_{eq} = \frac{3\sqrt{6}}{\pi} \frac{V_{\text{lg}0}}{\lambda I_n} \tag{4.13}$$

$$K_{eq1} = K_{ic} + \frac{\lambda K_T I_n K_{pc} K_{ps}}{J \omega_n}, \quad K_{eq2} = \frac{\lambda I_n K_T}{J \omega_n} \left(K_{ic} K_{ps} + K_{pc} K_{is} \right). \tag{4.14}$$

$$K_{eq3} = \frac{\lambda K_T I_n K_{ic} K_{is}}{J \omega_n} \tag{4.15}$$

$$\alpha_p = 0, \quad \beta_p = 0, \text{ and } \gamma_p = 0 \tag{4.16}$$

$$\alpha_q = \frac{S_0^{\,2}}{Q_0^{\,2}}, \quad \beta_q = -0.5 \frac{S_0^{\,2}}{Q_0^{\,2}} \frac{P_0^{\,2}}{Q_0^{\,2}}, \text{ and } \gamma_q = 0.5 \frac{S_0^{\,4}}{Q_0^{\,4}} \frac{P_0^{\,2}}{Q_0^{\,2}} \tag{4.17}$$

Matlab program for generating the proposed model

Appendix E presents a Matlab function "Build_DD" to convert the input data into an equivalent model. The input of the function is an array of the parameters as shown in Table 4.3. Two formats of input are supported in this program: standard user input and minimal user input, as seen below. The output of the function is a structure, which contains the parameters of the DC drive equivalent model. Please find more details in Appendix E.

Format 1 (standard user input):

V_{lg0}	P_0	Q_0	P_n	I_n	ω_n	R_d	L_d	K_{pc}	K_{ic}	K_{ps}	K_{is}	λ	K_E	J

Format 2 (minimal user input):

V_{lg0}	P_0	Q_0	P_n	I_n	ω_n

(Parameters are defined in Table 4.3)

Modeling Procedures

(1) Determine the initial operating conditions (V_{lg0}, P_0, and Q_0) of the DC drive from either preset values or from load flow calculation of an actual network.

(2) Prepare the input data as specified in Table 4.3. If the detailed parameters are unavailable, user might prepare a minimal user input (V_{lg0}, P_0, Q_0, P_n, I_n, ω_n). Enter the input data as specified in standard format (format 1) or minimal user input (format 2) accordingly.

(3) Run the Matlab function "Build_DD".

(4) Save the output "DD_output" for dynamic simulation, or for model aggregation program.

(5) For dynamic simulation, the output DC drive model can be implemented as a user-defined model (UDM). In some simulation software, UDM supports transfer function models.

(6) If the software doesn't support UDM, one may ignore the dynamic part H(s) & D(s), and represent DC drives simply as the static polynomial load model (polynomial terms).

4.3.5 Model Verification

The proposed model is simulated and verified by comparing against the detailed model. Two case studies are presented and conducted under *Simulink*. The equivalent model of DC drives is represented with transfer functions plus polynomial static load characteristics, as seen in Figure 4.11. In the simulation study, a three-phase voltage sag (depth: 95%, duration: 15 cycles) is applied to the

AC-side terminal of the DC drive. The fault starts at 0.5 sec and are cleared after 0.25 sec. The motor is running at 100% full speed.

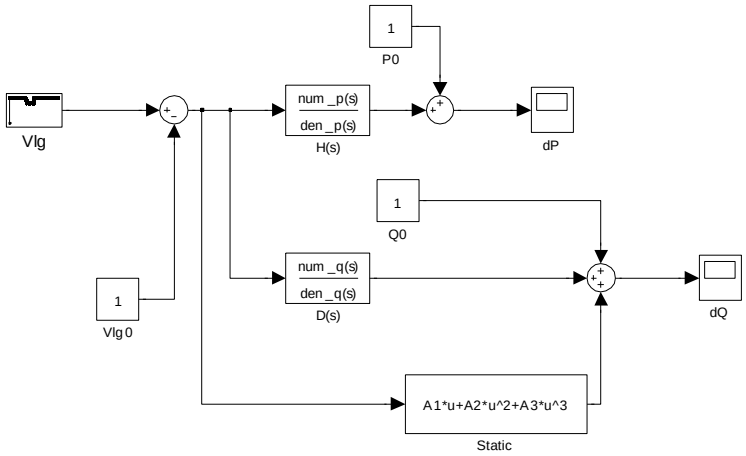

Figure 4.11 Simulation block diagram of equivalent model of DC drives

Case Study 1

Case 1 involves a 40HP DC drive (the simulation specification are given in Table 4.4). Following the given in subsection 4.3.3, the equivalent model can be established as given by Table 4.5. Simulation results are shown for 95% voltage sag (Figure 4.12 (*a*)) and 90% voltage sag (Figure 4.12 (*b*)).

Table 4.4 Simulation parameters for DC drives (40 HP)

Rated Power (HP)	40	Commutation Inductance L_c(H)	0
Nominal Voltage (V)	220	Armature Resistance R_d (Ω)	0.21
Nominal Current (A)	136	Smoothing Inductance L_d (mH)	20
Nominal Speed (rpm)	1500	Mutual Inductance L_{df} (H)	2.621
Motor Inertia (kg·m^2)	0.57	Field Current I_f (A)	1.5
Controller parameter	PI Speed controller: K_p=10.5, K_i=120.5 PI Current controller: K_p=2.48, K_i=37.3 Overload factor λ=1.5		
Mechanical Load	TL=239.36N·m		

Base Case Status	46.0kW+j27.2kVar, Supply voltage: 208V(L-L), 1500rpm (full speed)

Table 4.5 Parameters of equivalent model (Case 1)

Parameters	**Value**
V_0	1.0
P_0, Q_0	45.90kW, 27.2kVar
α_p, β_p, γ_p	[0, 0, 0]
α_q, β_q, γ_q	[3.849, -5.484, 21.109]
$H(s)$	$\frac{0.015\,s^4 + 1.491s^3 + 2.785\,s^2}{0.015s^4 + 3.625\,s^3 + 157.1\,s^2 + 2729s + 1.78e4}$
$D(s)$	$\frac{0.0427\,s^4 + 0.6828s^3\ s^2 - 7.936s^2}{0.015s^4 + 3.625\,s^3 + 157.1\,s^2 + 2729s + 1.78e4}$

*(Note: in this Table, the symbol "e" denotes the exponential of 10. For example "0.5e3" means 0.5*10^3.)*

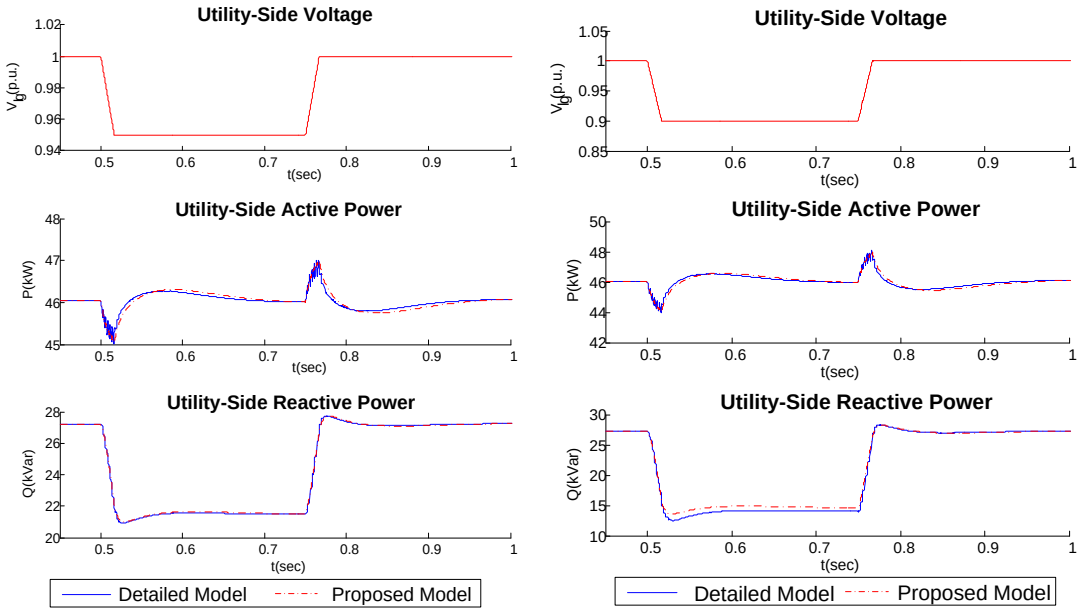

(*a*) 95% voltage sag (*b*) 90% voltage sag

Figure 4.12 Comparison between the detailed model and the proposed model (Case1)

Good agreement between the response of the detailed model and that of the proposed models is observed. The comparison has confirmed the accuracy and usefulness of the proposed DC drive models. However, there are still slight discrepancies in the active and reactive power between proposed model and detailed model.

Case Study 2

Case 2 involves a 120HP DC drive [57] (the specifications are shown in Table 4.6). The parameters of the equivalent model can be calculated and presented in Table 4.7. Simulation studies are conducted for 90% voltage sag (Figure 4.13(a)) and 85% voltage sag (Figure 4.13(b)).

Table 4.6 Simulation parameters for DC drives (120HP)

Rated horsepower P_n (HP)	120	Commutation Inductance L_c(H)	0
Nominal Voltage V_n (V)	220	Armature Resistance R_d (Ω)	0.06
Nominal Current I_n (A)	462	Smoothing Inductance L_d (mH)	4.3
Nominal Speed N_n (rpm)	560	Voltage constant K_E (V·sec)	3.59
Motor Inertia J (kg·m^2)	14.7	Overload factor λ	1.5
Controller parameter	PI Speed controller: K_p=118.4, K_i=1369 PI Current controller: K_p=1.36, K_i=0.072		
Mechanical Load	T_L=1750$N{\cdot}m$		
Base Case Status	107.0kW+j87.4$kVar$, supply voltage: 208V(L-L), 80%full speed		

Table 4.7 Parameters of equivalent model (Case 2)

Parameters	**Value**
V_0	1.0
P_0, Q_0	107.0kW, 87.4kVar

$\alpha_p, \beta_p, \gamma_p$	[0, 0, 0]
$\alpha_q, \beta_q, \gamma_q$	[2.534, -1.944, 4.928]
$H(s)$	$\frac{0.005\,s^4 + 0.474s^3 + 0.874s^2}{0.005s^4 + 0.57s^3 + 208.2s^2 + 5.08e3s + 3.21e4}$
$D(s)$	$\frac{-0.0077\,s^4 + 0.423s^3 - 1.341s^2}{0.005s^4 + 0.57s^3 + 208.2s^2 + 5.08e3s + 3.21e4}$

It's shown in Figure 4.13 (a) and (b) that there is a good agreement between detailed model and proposed model. Similar to case 1, one may observe that the accuracy of the model under small system disturbances scenario (Figure 4.13 (*a*)) is slightly better than that under large system disturbances scenario (Figure 4.13 (*b*)).

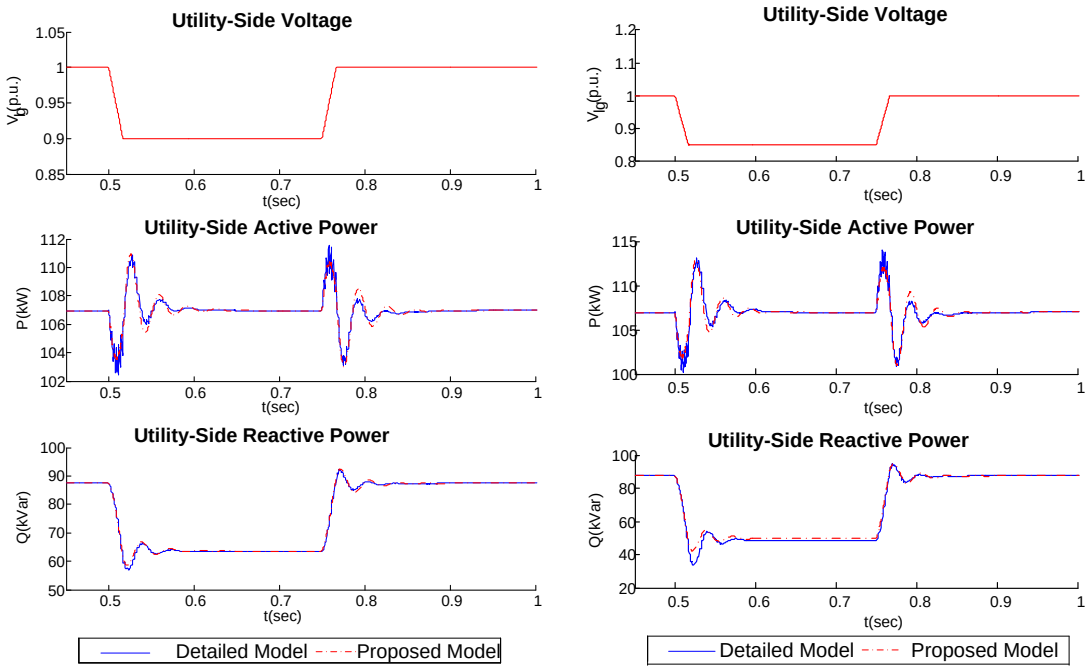

(*a*) 90% voltage sag (*b*) 85% voltage sag

Figure 4.13 Comparison between the detailed model and the proposed model

(Case2)

In summary, for the both case 1 and case 2, one can observe that the proposed equivalent model can capture the dynamic behavior of the detailed model adequately. But slight discrepancy between the two models is also observed; the discrepancy is getting larger as voltage sag goes deeper. In other words, the equivalent model works accurately only in the case of small voltage disturbances, which is resulted from the small-signal nature of the equivalent model. In fact, the scenario of large voltage disturbances (over ±15%) is omitted, since DC drives will be tripped and excluded from the dynamic simulation in this case.

In addition, if voltage drops deeply (i.e. by 20%), the firing angle will reach its lower limit. Since the proposed model doesn't consider the effect of limiters, the model is not able to capture the dynamic response well under this circumstance. Figure 4.14 presents an example of large disturbance scenario where the limiter is reached. This phenomenon is more likely to occur on DC drives with high power factor.

However, since DC drives are usually tripped when voltage drop below 90%, we don't need to consider the modeling of DC drives for voltage disturbances larger than 10%. As a result, the proposed equivalent model is sufficient to simulate the dynamic behavior of ride-through DC drives.

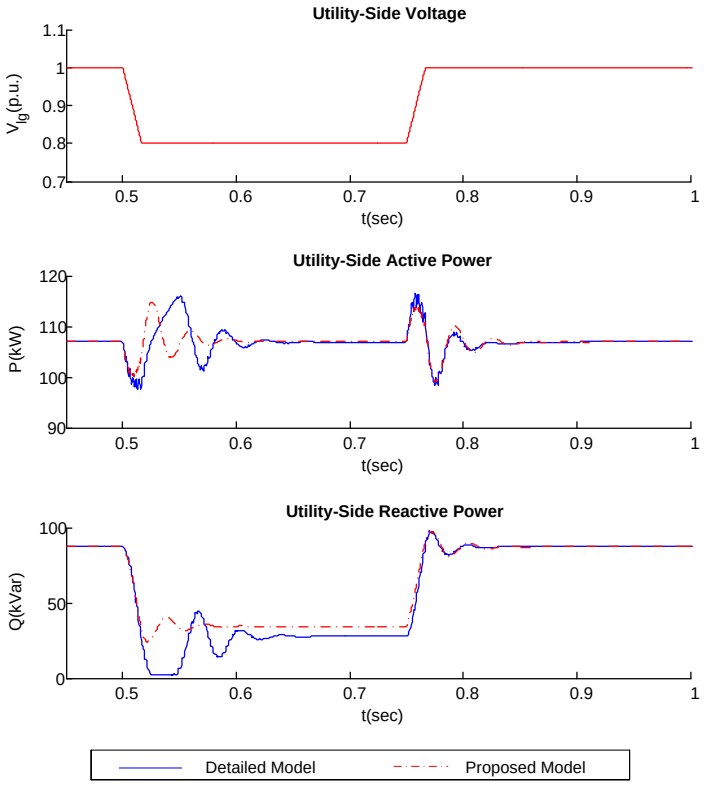

Figure 4.14 Large disturbance (80% voltage sag) scenario (case2)

4.4 Aggregating DC Drive Loads

This chapter mainly investigates the issue of aggregating DC drives, based on the proposed model. Two techniques are discussed hereby: 1) Technique for aggregating DC drives at the same bus; 2) Technique for incorporating cables and transformers connected to the DC drives.

4.4.1 Aggregating DC Drive Loads at the Same Bus

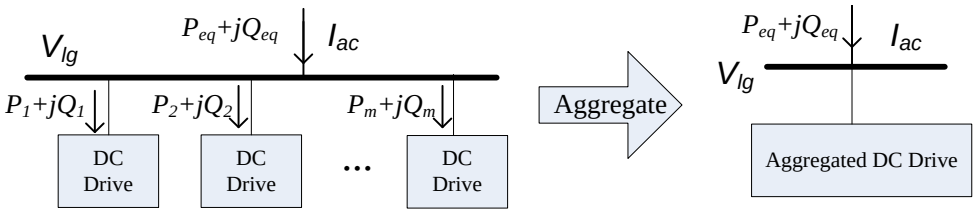

Figure 4.15 Aggregating a group of DC drives on the same bus

The objective of this subsection is to represent a group of DC drives on the same as one aggregated DC drive, as shown in Figure 4.15. Firstly, suppose the load characteristics of any single drive can be represented with:

$$P_i = P_{0i}\left[1+\alpha_{pi}\frac{V-V_0}{V_0}+\beta_{pi}\left(\frac{V-V_0}{V_0}\right)^2+\gamma_{pi}\left(\frac{V-V_0}{V_0}\right)^3+H_i(\mathrm{s})\frac{V-V_0}{V_0}\right] \quad (4.18)$$

$$Q_i = Q_{0i}\left[1+\alpha_{qi}\frac{V-V_0}{V_0}+\beta_{qi}\left(\frac{V-V_0}{V_0}\right)^2+\gamma_{qi}\left(\frac{V-V_0}{V_0}\right)^3+D_i(\mathrm{s})\frac{V-V_0}{V_0}\right] \quad (4.19)$$

where, $H(s)$ and $D(s)$ are in the form of fourth-order transfer functions:

$$H_i(s)=\frac{p_{4i}s^4+p_{3i}s^3+p_{2i}s^2+p_{3i}s+p_{0i}}{q_{4i}s^4+q_{3i}s^3+q_{2i}s^2+q_{3i}s+q_{0i}} \quad (4.20)$$

$$D_i(s)=\frac{w_{4i}s^4+w_{3i}s^3+w_{2i}s^2+w_{1i}s+w_{0i}}{v_{4i}s^4+v_{3i}s^3+v_{2i}s^2+v_{1i}s+v_{0i}} \quad (4.21)$$

Let's first consider aggregating active power of the model. Note that the active power P_{eq} for the aggregated DC drive must be equal to the sum of the active power of all the drives before aggregation. Therefore, we obtain:

$$P_{eq}=\sum_{i=1}^{m}P_{0i}\left[1+\alpha_{pi}\frac{V-V_0}{V_0}+\beta_{pi}\left(\frac{V-V_0}{V_0}\right)^2+\gamma_{pi}\left(\frac{V-V_0}{V_0}\right)^3+H_i(\mathrm{s})\frac{V-V_0}{V_0}\right] \quad (4.22)$$

Then it can be simplified as,

$$P_{eq}=P_{eq0}\left[1+\alpha_p'\frac{V-V_0}{V_0}+\beta_p'\left(\frac{V-V_0}{V_0}\right)^2+\gamma_p'\left(\frac{V-V_0}{V_0}\right)^3+\frac{V-V_0}{V_0}H_{eq}(\mathrm{s})\right] \quad (4.23)$$

where,

$$\alpha_p' = \frac{1}{P_{eq0}} \sum_{i=1}^{m} P_{0i}\alpha_{pi}, \quad \beta_p' = \frac{1}{P_{eq0}} \sum_{i=1}^{m} P_{0i}\beta_{pi}, \quad \text{and} \quad \gamma_p' = \frac{1}{P_{eq0}} \sum_{i=1}^{m} P_{0i}\gamma_{pi} \tag{4.24}$$

$$P_{eq0} = \sum_{i=1}^{m} P_{0i}, \text{ and } H_{eq}(\mathrm{s}) = \frac{1}{P_{eq0}} \sum_{i=1}^{m} P_{0i} H_i(\mathrm{s}) \tag{4.25}$$

For the purpose of model aggregation, we must represent $H_{eq}(s)$ with a fourth-order transfer function like $H_i(s)$. According to reference [61], any rational transfer functions like $H_i(s)$ can be approximated by a Taylor series about s=0 as shown by (4.26). Note that only up to 8th order terms are kept, because only 8th order terms are required to construct the Pade approximation of a 4th-order rational function like $H_{\mathrm{eq}}(s)$.

$$H_i(\mathrm{s}) = \frac{p_{4i}s^4 + p_{3i}s^3 + p_{2i}s^2 + p_{1i}s + p_{0i}}{q_{4i}s^4 + q_{3i}s^3 + q_{2i}s^2 + q_{1i}s + q_{0i}} \approx a_{0i} + a_{1i}s + a_{2i}s^2 + \ldots + a_{8i}s^8 \tag{4.26}$$

where, a_{ki} are Taylor expansion coefficients as calculate by,

$$a_{0i} = \frac{p_{0i}}{q_{0i}}, \quad \text{and} \quad a_{ki} = \frac{1}{q_{0i}}\left[p_{ki} - \sum_{h=1}^{k} q_{hi} a_{(k-h)i} \right] \quad (k = 1,\ 2,\ \ldots,8) \tag{4.27}$$

With $$p_{ki} = q_{ki} = 0, \ \forall k > 4$$

Therefore, $H_{eq}(s)$ can be approximated with power series using (4.26),

$$H_{eq}(\mathrm{s}) = \frac{1}{P_{eq0}} \sum_{i=1}^{m} P_{0i} H_i(\mathrm{s}) = \frac{1}{P_{eq0}} \sum_{i=1}^{m} P_{0i} \left(a_{0i} + a_{1i}s + a_{2i}s^2 + \ldots + a_{8i}s^2 \right) \tag{4.28}$$

Further simplifying (4.28) yields,

$$H_{eq}(\mathrm{s}) = A_0 + A_1 s + A_2 s^2 + \ldots + A_8 s^2 \tag{4.29}$$

where,

$$A_k = \frac{1}{P_{eq0}} \sum_{i=1}^{m} P_{0i} a_{ki} \quad (k = 1,\ 2,\ \ldots,8\ ) \tag{4.30}$$

Using Pade Approximation, $H_{eq}(s)$ in (4.29) can be approximated by a fourth-order rational function as shown by,

$$H_{eq}(\mathrm{s}) \approx A_0 + A_1 s + A_2 s^2 + \ldots + A_8 s^2 \approx \frac{p_4' s^4 + p_3' s^3 + p_2' s^2 + p_1' s + p_0'}{q_4' s^4 + q_3' s^3 + q_2' s^2 + q_1' s + 1} \tag{4.31}$$

where, p_1', p_2', p_3', p_4' and q_1', q_2', q_3', q_4' can be calculated from the coefficients A_1, A_2, …A_8 by solving the following linear equations (Please see details Pade approximation in the Appendix C).

$$\sum_{i=0}^{h} A_i q_{h-i}' - p_h' = 0 \quad (h=0,\ 1,\ \ldots\ 8) \tag{4.32}$$

$$p_h' = 0, \text{ and } q_h' = 0 \quad (h > 8) \tag{4.33}$$

Finally, the active power of the aggregated model can be represented as,

$$P_{eq} = P_{eq0}\left[1 + \alpha_p' \frac{V - V_0}{V_0} + \beta_p' \left(\frac{V - V_0}{V_0}\right)^2 + \gamma_p' \left(\frac{V - V_0}{V_0}\right)^3 + \frac{V - V_0}{V_0} H_{eq}(\mathrm{s})\right] \tag{4.34}$$

where,

$$H_{eq}(\mathrm{s}) = \frac{p_4' s^4 + p_3' s^3 + p_2' s^2 + p_3' s + p_0'}{q_4' s^4 + q_3' s^3 + q_2' s^2 + q_3' s + q_0'} \tag{4.35}$$

$$\alpha_p' = \frac{1}{P_{eq0}} \sum_{i=1}^{m} P_{0i} \alpha_{pi}, \quad \beta_p' = \frac{1}{P_{eq0}} \sum_{i=1}^{m} P_{0i} \beta_{pi}, \quad \text{and} \quad \gamma_p' = \frac{1}{P_{eq0}} \sum_{i=1}^{m} P_{0i} \gamma_{pi} \tag{4.36}$$

Similarly, the reactive power of the aggregated model can be represented as,

$$Q_{eq}=Q_{eq0}\left[1+\alpha_q{}'\frac{V-V_0}{V_0}+\beta_q{}'\left(\frac{V-V_0}{V_0}\right)^2+\gamma_q{}'\left(\frac{V-V_0}{V_0}\right)^3+D_{eq}(\mathrm{s})\frac{V-V_0}{V_0}\right] \quad (4.37)$$

where,

$$D_{eq}(\mathrm{s})=\frac{w_4{}'s^4+w_3{}'s^3+w_2{}'s^2+w_1{}'s+w_{0i}{}'}{v_{4i}{}'s^4+v_{3i}{}'s^3+v_{2i}{}'s^2+v_{1i}{}'s+v_{0i}{}'} \quad (4.38)$$

$$\alpha_{eq}=\frac{1}{Q_{eq0}}\sum_{i=1}^{m}Q_{0i}\alpha_i,\ \ \beta_{eq}=\frac{1}{Q_{eq0}}\sum_{i=1}^{m}Q_{0i}\beta_i,\ \text{ and }\ \gamma_{eq}=\frac{1}{Q_{eq0}}\sum_{i=1}^{m}Q_{0i}\gamma_i \quad (4.39)$$

4.4.2 Incorporating Series Impedance

After the DC drives connected to the same bus are aggregated into one DC drive model (equivalent), we need to incorporate the upstream series impedance (i.e. transmission line, cables or transformers connected to the bus) with this equivalent model. In such a manner, the DC drive model can represented at a higher-level bus with a new DC drive model (EM1), as seen in Figure 4.16.

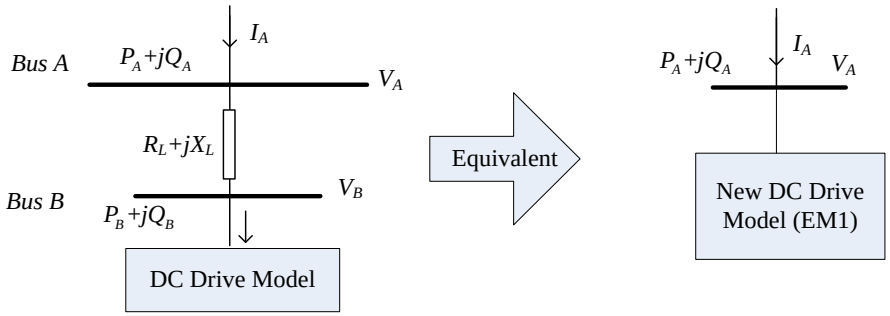

Figure 4.16 Incorporating cables or transformers with DC drive model

Incorporating Cables or Transmission Line:

Figure 4.16 illustrates a DC drive model (at Bus B) connected to the upstream bus

(Bus A) by an underground cable or overhead transmission line, which is represented by the impedance (R_L+jX_L). Suppose the original load characteristics at node B is given by:

$$\frac{\Delta P_B}{P_{B0}} = H(s)\frac{\Delta V_B}{V_{B0}} + L(\Delta V_B), \text{ and } \frac{\Delta Q_B}{Q_{B0}} = D(s)\frac{\Delta V_B}{V_{B0}} + W(\Delta V_B), \quad (4.40)$$

where, $H(s)$ and $D(s)$ are fourth-order transfer functions, and $L(\Delta V_B)$, $W(\Delta V_B)$ is the algebra polynomial function of ΔV_B as given by,

$$L(\Delta V_B) = \alpha_p \frac{\Delta V_B}{V_{B0}} + \beta_p \left(\frac{\Delta V_B}{V_{B0}}\right)^2 + \gamma_p \left(\frac{\Delta V_B}{V_{B0}}\right)^3 \quad (4.41)$$

$$W(\Delta V_B) = \alpha_q \frac{\Delta V_B}{V_{B0}} + \beta_q \left(\frac{\Delta V_B}{V_{B0}}\right)^2 + \gamma_q \left(\frac{\Delta V_B}{V_{B0}}\right)^3 \quad (4.42)$$

According to power invariant property, the active power observed at Bus A is equal to the sum of the active power observed at Bus A and power loss in the resistor R_L. (Calculated in three phases)

$$P_A \approx P_B + \frac{P_B^{\,2} + Q_B^{\,2}}{3V_B^{\,2}} R_L \quad (4.43)$$

Similarly, the reactive power observed at Bus A is given by,

$$Q_A \approx Q_B + \frac{P_B^{\,2} + Q_B^{\,2}}{3V_B^{\,2}} X_L \quad (4.44)$$

For a small voltage drop ΔV_A at the Bus A, taking the total derivative of (4.43), and (4.44), one can obtain the change in active and reactive power observed at Bus *A*, as shown by,

$$\begin{pmatrix}\Delta P_A\\ \Delta Q_A\end{pmatrix}=\begin{pmatrix}1+\dfrac{2R_L P_{B0}}{3V_{B0}^{\ 2}} & \dfrac{2R_L Q_{B0}}{3V_{B0}^{\ 2}}\\ \dfrac{2X_L P_{B0}}{3V_{B0}^{\ 2}} & 1+\dfrac{2X_L Q_{B0}}{3V_{B0}^{\ 2}}\end{pmatrix}\begin{pmatrix}\Delta P_B\\ \Delta Q_B\end{pmatrix}+\begin{pmatrix}\dfrac{-2R_L S_{B0}^{\ 2}}{3V_{B0}^{\ 3}}\\ \dfrac{-2X_L S_{B0}^{\ 2}}{3V_{B0}^{\ 3}}\end{pmatrix}\Delta V_B \quad (4.45)$$

Substituting (4.40) into (4.45) yields,

$$\begin{pmatrix}\Delta P_A\\ \Delta Q_A\end{pmatrix}=\begin{pmatrix}K_1(\mathrm{s})\\ K_2(\mathrm{s})\end{pmatrix}\frac{\Delta V_B}{V_{B0}}+\begin{pmatrix}P_{B0}\alpha_p-\dfrac{2R_L S_{B0}^{\ 2}}{3V_{B0}^{\ 2}}\\ Q_{B0}\alpha_q-\dfrac{2X_L S_{B0}^{\ 2}}{3V_{B0}^{\ 2}}\end{pmatrix}\frac{\Delta V_B}{V_{B0}}+\begin{pmatrix}P_{B0}\beta_p\\ Q_{B0}\beta_q\end{pmatrix}\left(\frac{\Delta V_B}{V_{B0}}\right)^2+\begin{pmatrix}P_{B0}\gamma_p\\ Q_{B0}\gamma_q\end{pmatrix}\left(\frac{\Delta V_B}{V_{B0}}\right)^3 \quad (4.46)$$

where,

$$K_1(\mathrm{s})=\left(P_{B0}+\frac{2R_L P_{B0}^{\ 2}}{3V_{B0}^{\ 2}}\right)H(\mathrm{s})+\left(\frac{2R_L Q_{B0}^{\ 2}}{3V_{B0}^{\ 2}}\right)D(\mathrm{s}) \quad (4.47)$$

$$K_2(\mathrm{s})=\left(\frac{2X_L P_{B0}^{\ 2}}{3V_{B0}^{\ 2}}\right)H(\mathrm{s})+\left(Q_{B0}+\frac{2X_L Q_{B0}^{\ 2}}{3V_{B0}^{\ 2}}\right)D(\mathrm{s}) \quad (4.48)$$

According to reference [62], for two buses that are connected by an impedance R_L+jX_L, and with a delivered power of P_B+jQ_B, the difference of voltage magnitude (phase-to-ground) between Bus A and Bus B can be expressed by,

$$V_A \approx V_B+\frac{P_B R_L+Q_B X_L}{3V_B} \quad (4.49)$$

where, P, Q are total-three-phase variables, and V_A, V_B are phase voltage.

Taking total derivative of (4.49) yields,

$$\Delta V_A \approx \frac{R_L}{3V_{B0}}\Delta P_B+\frac{X_L}{3V_{B0}}\Delta Q_B+\left(1-\frac{P_{B0}R_L+Q_{B0}X_L}{3V_{B0}^{\ 2}}\right)\Delta V_B \quad (4.50)$$

For the convenience of model reduction, we assume a linear relationship between

ΔV_A and ΔV_B. Hence, we will neglect the 2nd and 3rd order polynomial terms and the dynamic part of ΔP_B and ΔQ_B as given by (4.50). In such a manner, one can obtain:

$$\Delta V_A \approx \frac{R_L}{3V_{B0}} P_{B0}\alpha_p \left(\frac{\Delta V_B}{V_{B0}}\right) + \frac{X_L}{3V_{B0}} Q_{B0}\alpha_q \left(\frac{\Delta V_B}{V_{B0}}\right) + \left(1 - \frac{P_{B0}R_L + Q_{B0}X_L}{3V_{B0}^{\ 2}}\right)\Delta V_B \qquad (4.51)$$

Simplifying (4.51) yields,

$$\Delta V_B \approx \eta \Delta V_A \qquad (4.52)$$

where,

$$\eta = \left[1 + \left(\alpha_p - 1\right)\frac{P_{B0}R_L}{3V_{B0}^{\ 2}} + \left(\alpha_q - 1\right)\frac{Q_{B0}X_L}{3V_{B0}^{\ 2}}\right]^{-1} \qquad (4.53)$$

Combining (4.46) and (4.52) yields,

$$\frac{\Delta P_A}{P_{A0}} = G(\mathrm{s})\frac{\Delta V_A}{V_{A0}} + \alpha_p{}'\frac{\Delta V_B}{V_{B0}} + \beta_p{}'\left(\frac{\Delta V_B}{V_{B0}}\right)^2 + \gamma_p{}'\left(\frac{\Delta V_B}{V_{B0}}\right)^3 \qquad (4.54)$$

$$\frac{\Delta Q_A}{Q_{A0}} = J(\mathrm{s})\frac{\Delta V_A}{V_{A0}} + \alpha_q{}'\frac{\Delta V_B}{V_{B0}} + \beta_q{}'\left(\frac{\Delta V_B}{V_{B0}}\right)^2 + \gamma_q{}'\left(\frac{\Delta V_B}{V_{B0}}\right)^3 \qquad (4.55)$$

where,

$$G(\mathrm{s}) = \frac{\eta V_{A0}}{P_{A0}}\left(\frac{P_{B0}}{V_{B0}} + \frac{2R_L P_{B0}^{\ 2}}{3V_{B0}^{\ 3}}\right)H(\mathrm{s}) + \frac{\eta V_{A0}}{P_{A0}}\left(\frac{2R_L Q_{B0}^{\ 2}}{3V_{B0}^{\ 3}}\right)D(\mathrm{s}) \qquad (4.56)$$

$$J(\mathrm{s}) = \frac{\eta V_{A0}}{Q_{A0}}\left(\frac{2X_L P_{B0}^{\ 2}}{3V_{B0}^{\ 3}}\right)H(\mathrm{s}) + \frac{\eta V_{A0}}{Q_{A0}}\left(\frac{Q_{B0}}{V_{B0}} + \frac{2X_L Q_{B0}^{\ 2}}{3V_{B0}^{\ 3}}\right)D(\mathrm{s}) \qquad (4.57)$$

$$\alpha_p{}' = \frac{\eta V_{A0}}{V_{B0}}\left(\frac{P_{B0}}{P_{A0}}\alpha_p - \frac{2R_L S_{B0}^{\ 2}}{3V_{B0}^{\ 2}P_{A0}}\right),\ \beta_p{}' = \left(\frac{\eta V_{A0}}{V_{B0}}\right)^2\frac{P_{B0}}{P_{A0}}\beta_p,\ \gamma_p{}' = \left(\frac{\eta V_{A0}}{V_{B0}}\right)^3\frac{P_{B0}}{P_{A0}}\gamma_p \qquad (4.58)$$

$$\alpha_q{}' = \frac{\eta V_{A0}}{V_{B0}}\left(\frac{Q_{B0}}{Q_{A0}}\alpha_q - \frac{2X_L S_{B0}^{\ 2}}{3V_{B0}^{\ 2}Q_{A0}}\right),\ \beta_q{}' = \left(\frac{\eta V_{A0}}{V_{B0}}\right)^2\frac{Q_{B0}}{Q_{A0}}\beta_q,\ \gamma_p{}' = \left(\frac{\eta V_{A0}}{V_{B0}}\right)^3\frac{Q_{B0}}{Q_{A0}}\gamma_q \qquad (4.59)$$

Note that H(s) and D(s) are fourth-order transfer functions. Recall that in the previous section, we proposed a technique to approximate the sum of a number of fourth-order transfer functions using an equivalent transfer function in the same order. As a result, $G(s)$ and $J(s)$ can be approximated with a new fourth-order transfer functions in the form of,

$$G_{eq}(\mathrm{s}) \approx \frac{p_4's^4+p_3's^3+p_2's^2+p_3's+p_0'}{q_4's^4+q_3's^3+q_2's^2+q_3's+q_0'} \tag{4.60}$$

$$J_{eq}(\mathrm{s}) \approx \frac{w_4's^4+w_3's^3+w_2's^2+w_1's+w_{0i}'}{v_{4i}'s^4+v_{3i}'s^3+v_{2i}'s^2+v_{1i}'s+v_{0i}'} \tag{4.61}$$

Consequently, the final DC drive model with the cable cooperated can be represented with the following equations,

$$\frac{P_A}{P_{A0}} = \left[1+\alpha_p'\frac{V_A-V_{A0}}{V_{A0}}+\beta_p'\left(\frac{V_A-V_{A0}}{V_{A0}}\right)^2+\gamma_p'\left(\frac{V_A-V_{A0}}{V_{A0}}\right)^3\right]+G_{eq}(\mathrm{s})\frac{V_A-V_{A0}}{V_{A0}} \tag{4.62}$$

$$\frac{Q_A}{Q_{A0}} = \left[1+\alpha_q'\frac{V_A-V_{A0}}{V_{A0}}+\beta_q'\left(\frac{V_A-V_{A0}}{V_{A0}}\right)^2+\gamma_q'\left(\frac{V_A-V_{A0}}{V_{A0}}\right)^3\right]+J_{eq}(\mathrm{s})\frac{V_A-V_{A0}}{V_{A0}} \tag{4.63}$$

where, the coefficients (α, β, γ) are given in (4.58) (4.59).

Incorporating Transformers:

Figure 4.17 illustrates a step-down transformer (ratio 1:n) that supplies multiple DC drives connected to the same bus. Using the methods in the sub-section 4.1, the DC drives have been aggregated into one lumped DC drive model. In this figure, a transformer can be represented with an ideal transformer and a leakage

inductor jX_T, as seen in Figure 4.17. The nominal voltage of the primary side is donated as V_A and the nominal voltage of the secondary side is donated as V_B.

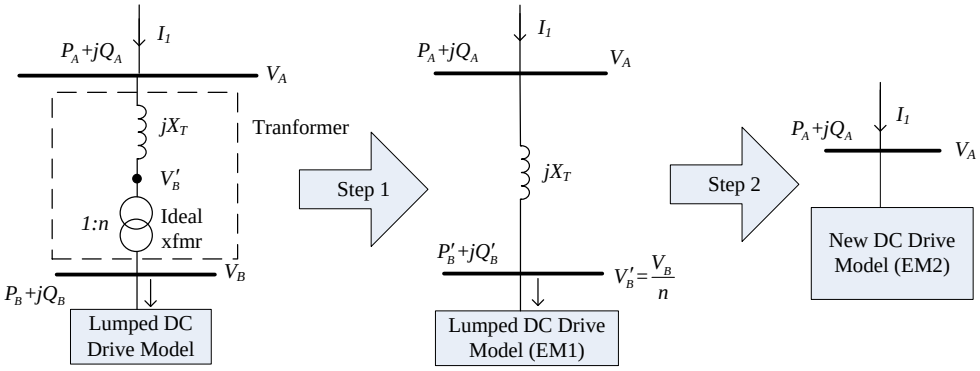

Figure 4.17 Incorporating transformers with DC drive model

The proposed method has been divided into two steps as described as follows.

Step 1: The first step is to incorporate the ideal transformer by referring the DC drive model to the primary side. For an ideal transformer, the active/reactive power loss is zero and the voltage relationship is linear. Suppose the original load dynamics at node B is given by:

$$\frac{P_B}{P_{B0}}=\left[1+\alpha_p\frac{V_B-V_{B0}}{V_{B0}}+\beta_p\left(\frac{V_B-V_{B0}}{V_{B0}}\right)^2+\gamma_p\left(\frac{V_B-V_{B0}}{V_{B0}}\right)^3\right]+G(\mathrm{s})\frac{V_B-V_{B0}}{V_{B0}} \quad (64)$$

Therefore, from the primary side, one can obtain $P_B'=P_B$. Then we have,

$$\frac{P_B'}{P_{B0}'}=\left[1+\alpha_p\frac{V_B'-V_{B0}'}{V_{B0}'}+\beta_p\left(\frac{V_B'-V_{B0}'}{V_{B0}'}\right)^2+\gamma_p\left(\frac{V_B'-V_{B0}'}{V_{B0}'}\right)^3\right]+G(\mathrm{s})\frac{V_B'-V_{B0}'}{V_{B0}'} \quad (65)$$

where, $V_{B0}'=V_{B0}/n$ and $V_B'=V_B/n$.

Consequently, the model given by step 1 (EM1) can be simply obtained by replacing the initial-condition voltage V_B with (V_B/n), and V_B' with (V_B'/n). In other words, the parameters [H(s) D(s) α β γ] won't change when the ideal transformer is incorporated.

Step 2: incorporating the leakage inductor jX_T. The technique to incorporate leakage inductor is exactly the same as incorporating a cable with the same impedance. One can obtain the final equivalent model (EM2) using the technique for incorporating cables.

4.4.3 Case Studies

In this sub-section, two comprehensive case studies are presented to verify the proposed aggregation techniques. Appendix E presents a package of Matlab functions to implement the proposed aggregation techniques. These Matlab functions can be utilized as elementary modules, which the users can use to develop a case-specific aggregation program. The aggregation program may be developed based on the concept of bottom-up approaches. The bottom-up approach allows the user to apply equivalence techniques from the bottom level up to the top level until a single-unit model is obtained. Please see Appendix E for more details.

Description of Simulation Setup

Simulation study is used to compare the dynamic response of the original models and the aggregated model. For this purpose, a voltage sag (sag depth: 90%, duration: 15 cycles) is applied to the main bus. The dynamic response of the active and reactive power P_{tot} and Q_{tot} is used to compare the original models and the aggregated model. Figure 4.18 illustrates the comparison study between original models and the aggregated model.

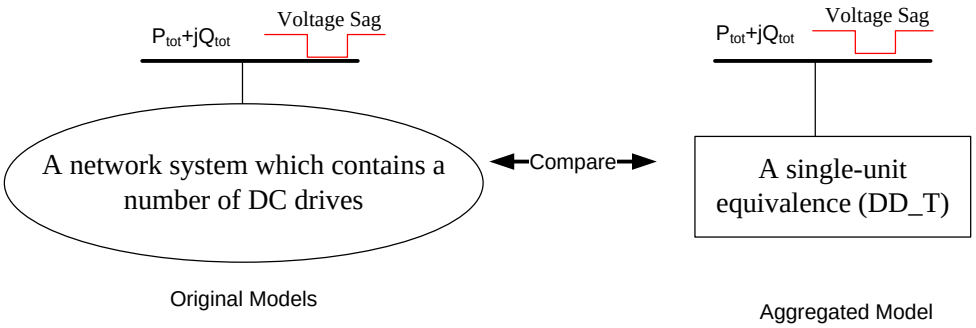

Figure 4.18 Comparison between original models and aggregated model

Case studies are conducted using Simulink software (SimPowerSystem toolbox). In the simulation study, each DC drive (for the original models and aggregated model) is represented with the proposed equivalent model, which is implemented with the "user-defined dynamic load model" block. The active and reactive power of this block is controlled by the proposed equivalent model as shown in Figure 4.19.

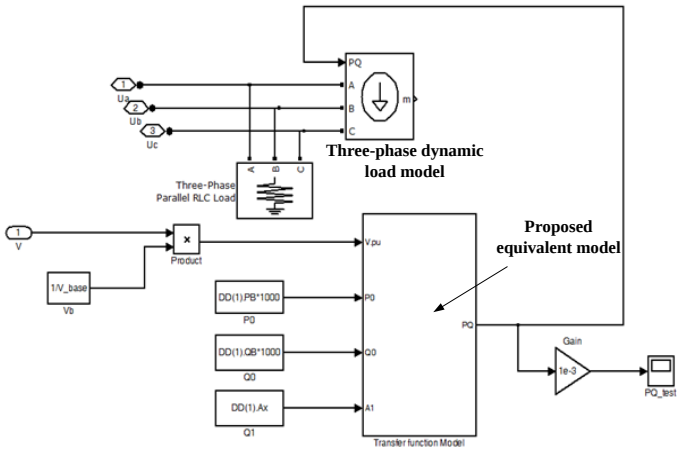

Figure 4.19 Representation of one single DC drive

Case 1. Aggregating the DC drive models at the same bus

Figure 4.20 present the schematic diagram of case 1, in which a group of DC drives (DD1~DD4) are connected to the same bus. The aggregated model is represented with "DD_T". The specifications for the original model are attached in the Appendix C. The specifications for the aggregated model are given in the Table 4.8.

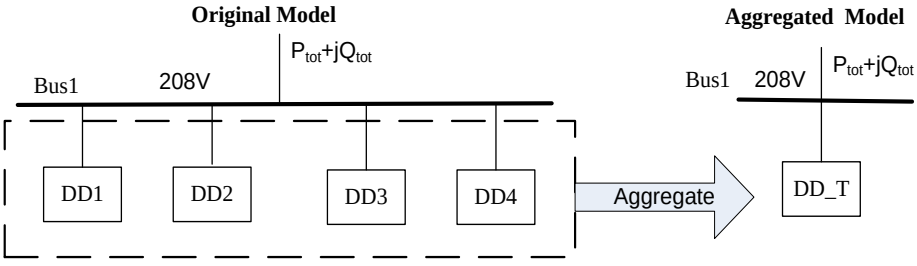

Figure 4.20 Schematic diagram (Case 1)

Table 4.8 Parameters of the aggregated model (Case 1)

Parameters	**Value**
V_0	1.0
P_0, Q_0	142.13kW, 133.42kVar
$\alpha_p, \beta_p, \gamma_p$	[0, 0, 0]
$\alpha_q, \beta_q, \gamma_q$	[2.2199, -1.5861, 4.4620]
$H(s)$	$\frac{s^4 + 25.30\,s^3 + 35.48\,s^2}{s^4 + 157.20\,s^3 + 5.28e3\,s^2 + 7.61e4\,s + 4.014e5}$
$D(s)$	$\frac{-1.22s^4 + 194.58\,s^3 - 553.4s^2}{s^4 + 987.24\,s^3 + 4.32e4\,s^2 + 7.62e5\,s + 4.67e6}$

Figure 4.21 (*a*) presents the comparison between the original model and the aggregated model in terms of the dynamic response (P_{tot} and Q_{tot}) subjected to a voltage sag of 90%. The simulation result shows that there's a good agreement between the dynamic response of aggregated model and that of the original models.

It's also observed that there's some discrepancy between the aggregated model and original model. Figure 4.21 (*b*) reveals that the discrepancy can be reduced without using the order-reduction technique. This result is meaningful in revealing that the order-reduced technique is the major source of the model errors.

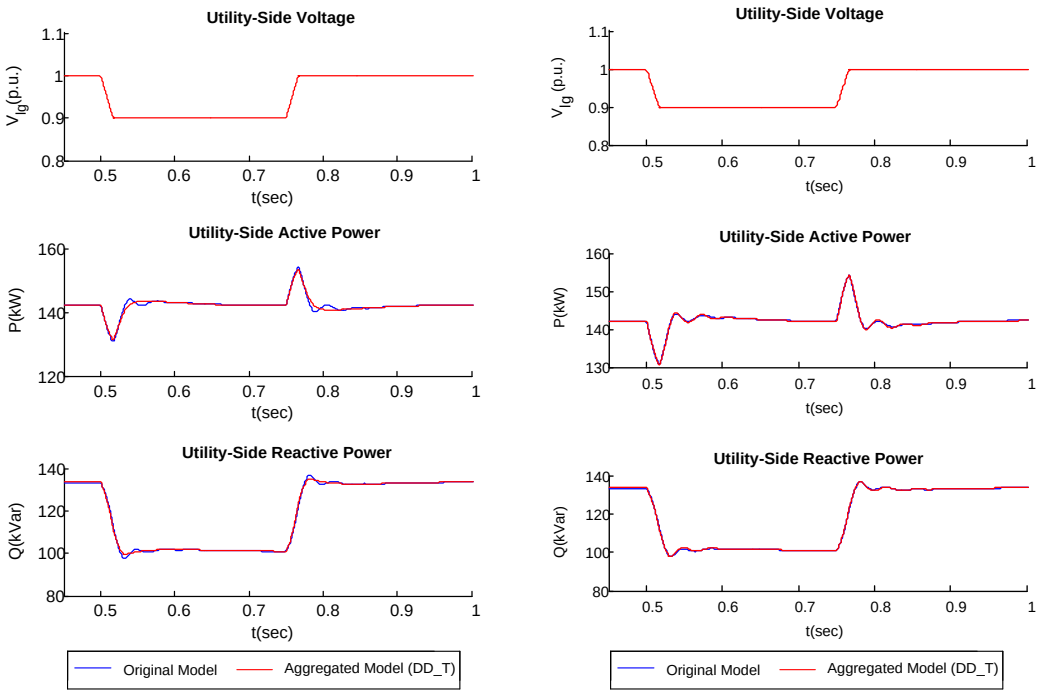

(*a*) with order-reduction techniques (b) without order-reduction techniques

Figure 4.21 Comparison between the individual models and the aggregated model (Case 1)

Case 2. Aggregating DC drive models at the different buses

Figure 4.22 shows the schematic diagram of a 6-bus comprehensive industrial system containing DC drive loads. The detailed specifications are attached in the Appendix C. The specification of

In the system, DD1~DD4 are DC drive loads which are represented with proposed equivalence models. Using the proposed aggregation techniques, this comprehensive system can be aggregated and represent with one lumped DC drive model DD_T.

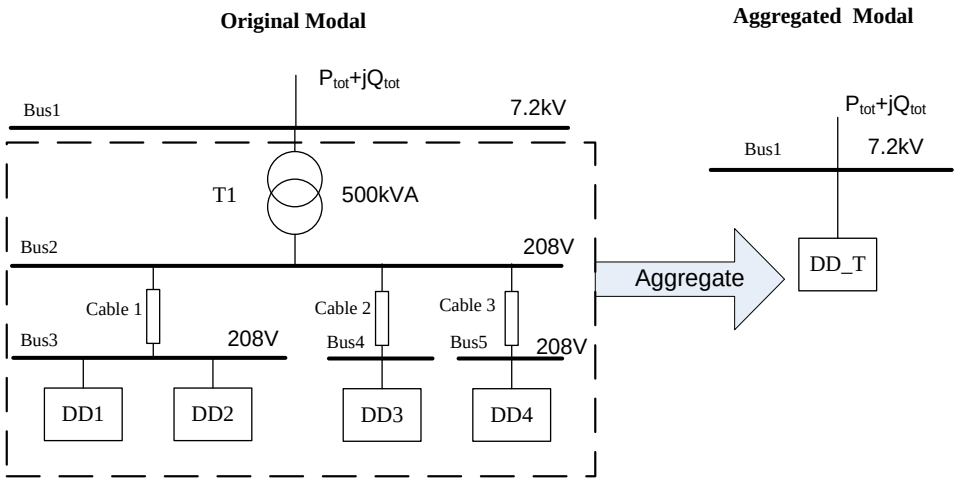

Figure 4.22 Schematic diagram (Case 2)

Table 4.9 Parameters of the aggregated model (Case 2)

Parameters	**Value**
V_0	1.0
P_0, Q_0	150.49kW, 136.77kVar
$\alpha_p, \beta_p, \gamma_p$	[0, 0, 0]
$\alpha_q, \beta_q, \gamma_q$	[2.192, -1.622, 4.799]
$H(s)$	$\frac{s^4 + 25.57\,s^3 + 33.88\,s^2}{s^4 + 145.60\,s^3 + 4.83e3\,s^2 + 6.94e4\,s + 3.66e5}$
$D(s)$	$\frac{-1.19s^4 + 278.35\,s^3 - 695.65s^2}{s^4 + 1266.1\,s^3 + 5.57e4\,s^2 + 9.85e5\,s + 6.02e6}$

In order to test the aggregated model (DD_T), a 90% voltage sag is applied to the main bus. Figure 4.23 (a) presents the comparison between the original models and the aggregated model.

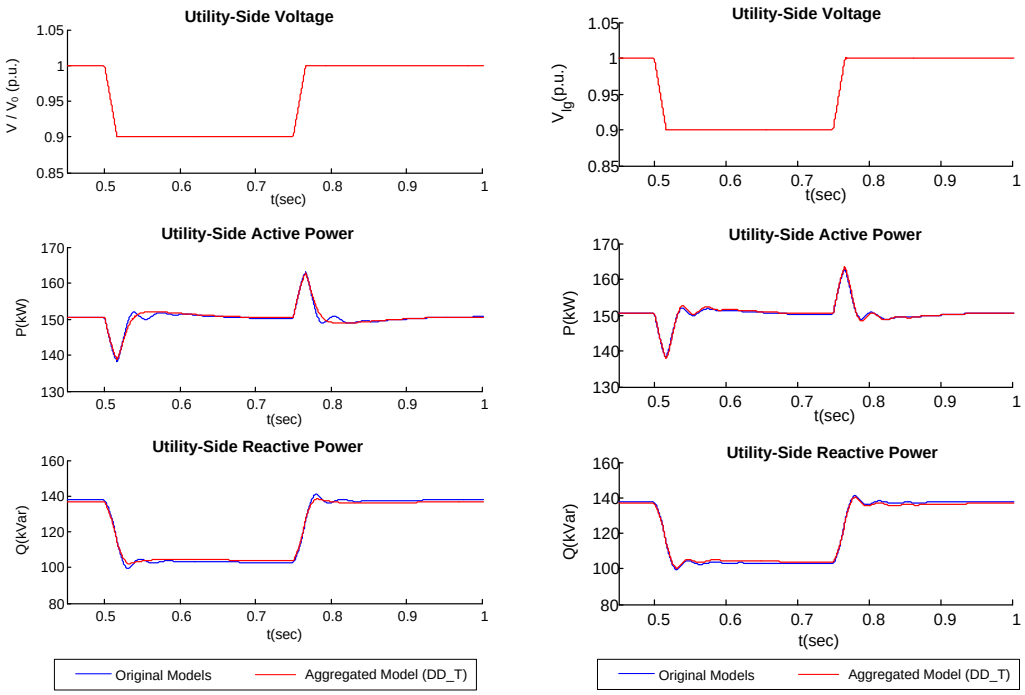

(a) with order-reduction techniques (b) without order-reduction techniques

Figure 4.23 Comparison between the individual models and the equivalent circuit model (Case 2)

The simulation result has revealed that the aggregated model can sufficiently capture the dynamic characteristics of the the original models. One may observe some discrepancies between aggregated model and original model. In comparison, the simulation result without the order-reduction technique (Figure 4.23 (*b*)) has a better accuracy. This study result also reveals that the order-reduction technique can lead to the loss in model accuracy. In addition, other minor source of errors can be the simplifying conditions assumed in incorporating series impedance.

4.5 Summary

This chapter investigates the issue of modeling and aggregating DC motor drives for power system dynamic performance studies. The major achievement of this chapter is summarized as below:

- A DC drive trip curve is proposed to determine if a given voltage sag will cause nuisance tripping of DC drives.

- For the ride-through DC drives, a dynamic load model is proposed, which is based on the average-value model (AVM) of DC drives and in the form of fourth-order transfer functions.

- Techniques to aggregate DC drive loads at the same bus and to incorporate cables and transformers with the proposed models are proposed and verified through the simulation studies. It’s found that the order-reduction technique is the major source of errors.

Chapter 5

A Synchrophasor-Based Technique for Analysis and Monitoring of Small-Signal Angle Stability

This chapter presents another stability-related project conducted during my Master period. Some of this chapter are taken from reference [63], one of my unpublished paper. This chapter mainly develops a synchrophasor-based technique for analysis and monitoring of small-signal angle stability.

5.1 Introduction

With the increasing installations of phasor measurement units (PMU), a large amount of phasor data, which have the great potential to enhance the situational awareness of power systems, are available. To fulfill the potential of phasor data, this chapter presents a new real-time method for analysis and monitoring of small-signal angle stability. This method is based on real-time phasor data and a new network decoupling transform, which is called Channel Components Transform (CCT).

The CCT is conceived from the observation that a power network can be represented as a multi-node, multi-branch Thévenin equivalent circuit, which in

turn can be eigen-decomposed into a set of two-node, single-branch equivalent circuits (the channels). Since these channels are very simple power systems, they can be used to readily and analytically extract valuable information regarding the stability conditions of complex networks in real-time.

This CCT technique has been successfully applied to monitor and analyze voltage stability in reference [64]. In this chapter, the CCT is applied to analyze the small-signal angle stability. The major advantage of the proposed method is that the transformation of a complex power network into a set of elementary decoupled circuits facilitates considerably the small-signal angle stability analysis.

5.2 Basic Ideas of Proposed Method

5.2.1 Mathematical Basis of Channel Component Transform

A general multi-machine power network, as shown in Figure 5.1(a), consists of *n+1* generators, *m* loads and *p* lines. This network can then be represented by a Thevenin equivalent circuit model as given by,

$$\begin{bmatrix} \hat{V}_{G_1} \\ \hat{V}_{G_2} \\ \vdots \\ \hat{V}_{G_n} \end{bmatrix} = \begin{bmatrix} k_1 \\ k_2 \\ \vdots \\ k_n \end{bmatrix} \cdot \hat{V}_S + \begin{bmatrix} z_{11} & z_{12} & \cdots & z_{1n} \\ z_{21} & z_{22} & \cdots & z_{2n} \\ \vdots & \vdots & \ddots & \vdots \\ z_{n1} & z_{n2} & \cdots & z_{nn} \end{bmatrix} \cdot \begin{bmatrix} \hat{I}_{G_1} \\ \hat{I}_{G_2} \\ \vdots \\ \hat{I}_{G_n} \end{bmatrix} \tag{5.1}$$

or,

$$[\hat{V}_G] = [K] \cdot \hat{V}_S + [Z] \cdot [\hat{I}_G] \tag{5.2}$$

where, $\hat{V}_{G_n}$ and $\hat{I}_{G_n}$ denotes the voltage and current phasors at the *n-th* generation bus, respectively, $\hat{V}_S$ denotes the voltage phasor at the reference bus (normally an extremely large power plant or a large external power system), and [*Z*] donates the nodal impedance matrix of the power network. The [*Z*] matrix can contain many components as transmission lines, transformers, all the loads modeled as constant impedance and even the generator internal impedances.

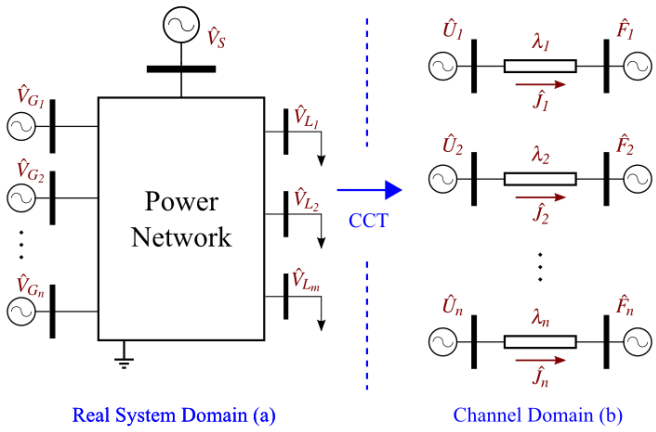

Figure 5.1 A general electric power network and its representation in the channel domain

Applying the eigen-decomposition of matrix [*Z*] in (5.2) yields:

$$[Z] = [T]^{-1} \cdot [\Lambda] \cdot [T] \tag{5.3}$$

where [*Λ*] and [*T*] are the eigenvalues and eigenvectors matrices of [*Z*], respectively. Substituting (5.3) into (5.2) yields:

$$[\hat{V}_G] = [K] \cdot \hat{V}_S + \left([T]^{-1} \cdot [\Lambda] \cdot [T]\right) \cdot [\hat{I}_G] \tag{5.4}$$

Multiplying [*T*] on the both sides of (5.4) yields:

$$[T]\cdot[\hat{V}_G]=[T]\cdot[K]\cdot\hat{V}_S+[\Lambda]\cdot[T]\cdot[\hat{I}_G] \tag{5.5}$$

Equation (5.5) can be simply represented as:

$$[\hat{U}]=[\hat{F}]+[\Lambda]\cdot[\hat{J}] \tag{5.6}$$

or,

$$\begin{bmatrix}\hat{U}_1\\ \hat{U}_2\\ \vdots\\ \hat{U}_n\end{bmatrix}=\begin{bmatrix}\hat{F}_1\\ \hat{F}_2\\ \vdots\\ \hat{F}_n\end{bmatrix}+\begin{bmatrix}\lambda_1 & 0 & 0 & 0\\ 0 & \lambda_2 & 0 & 0\\ 0 & 0 & \ddots & \vdots\\ 0 & 0 & \cdots & \lambda_n\end{bmatrix}\cdot\begin{bmatrix}\hat{J}_1\\ \hat{J}_2\\ \vdots\\ \hat{J}_n\end{bmatrix} \tag{5.7}$$

where,

$U=[T]V_G$ donates the generators voltage phasors (channel systems)

$F=[T][K]V_S$ donates the reference voltage phasors (channel systems)

$J=[T]I_G$ donates the generators current phasors (channel systems)

The results in (5.7) are essentially equivalent to a group of Single-Machine Infinite-Bus (SMIB) systems, as shown in Figure 5.1(b). In this method, each SMIB system is corresponding to a "channel". These SMIB systems are called "channel systems".

Therefore, applying this transformation, a complex network of *n+1* generators, *m* loads, *p* lines can now be represented by a set of *n* two-node, single-branch equivalent circuits (the channels), which can be further simplified for angle

stability analysis to a Single-Machine Infinite-Bus (SMIB) system. Since these SMIB systems are simpler, important information can be readily and analytically extracted about the angle stability, as will be discussed in the next subsection.

Note that, in the equation (5.2), all the loads were represented by a constant impedance model so that they were included into the impedance matrix and a model reduced to the generator buses was used to simplify the explanations. Later, a more complex model for the load will be discussed.

5.2.2 Appling CCT for Small-Signal Angle Stability Study

This subsection briefly discusses how the channel systems can be used for small-signal angle stability analysis and monitoring. As a comprehensive example, the simple 3-bus, 3-generator system shown in Figure 5.2 (a) will be used. The data of this comprehensive system is summarized in Table 5.1. Using the CCT technique introduced in the previous subsection, we can obtain the corresponding channel systems as seen in Figure 5.2 (b).

Table 5.1 Test system parameters

P_1	1.2 pu	$2H_1$	10.0 s
P_2	1.2 pu	$2H_2$	10.0 s
V_1	1.0 pu	$2H_3$	50.0 s
V_2	1.0 pu	Z_{12}	j0.8162 pu

$\boldsymbol{V_3}$	$1.0\angle 0.0\,°$pu	$\boldsymbol{Z_{13}}$	$j0.5632$ pu
$\boldsymbol{D_{1,2,3}}$	0	$\boldsymbol{Z_{23}}$	$j0.7022$ pu

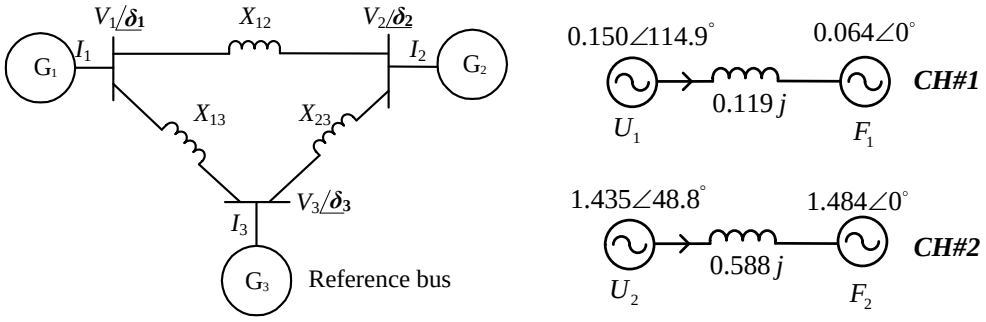

(a) real system (b) channel systems

Figure 5.2 A simple comprehensive 3-bus, 3-generator system

Since this system has 3 generators, the application of the CCT decouples the real system into two SMIB systems in the channel domain, which are called Channel 1 (CH#1) and Channel 2 (CH#2). The parameters of the channel systems are given in the circuit diagram in Figure 5.2 (b).

With regard to the two SMIB systems in Figure 5.2 (b), the transfer power of generators can be characterized by the traditional $P\delta$ curves:

$$P_{CH_i} = \text{Real}\left\{\hat{U}_i \cdot \hat{J}_i^*\right\} = \frac{\left|\hat{U}_i\right|^2}{\left|\lambda_i\right|}\cos\left(\angle\lambda_i\right) - \frac{\left|\hat{U}_i\right|\left|\hat{F}_i\right|}{\left|\lambda_i\right|}\cos\left(\delta_{CH_i} + \angle\lambda_i\right) \qquad (5.8)$$

where, P_{CHi} is the active power transferred by the *i-th* channel, $\angle\lambda_i$ is the angle of the impedance of the *i-th* channel, and δ_{CHi} is the angle difference between the voltage phasors of the *i-th* channel, i.e. $\delta_{CH_i} = \angle\hat{U}_i - \angle\hat{F}_i$.

Using (5.8), Pδ curves for each channel can be obtained. Figure 5.3 shows the Pδ

curves for the channel systems seen in Figure 5.2 (b). The operating points of each channels related to the base case are represented by blue dots.

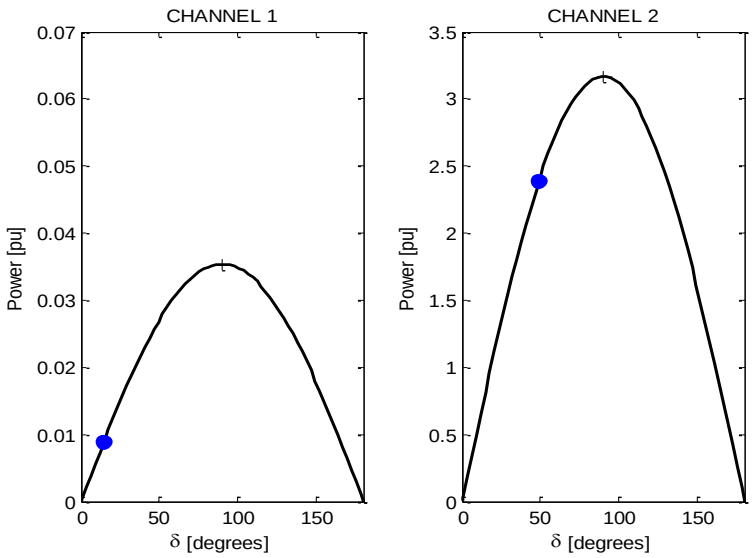

Figure 5.3 $P\delta$ curves of channel systems

It's observed in extensive simulation studies that the real system is stable if all the corresponding channel systems are stable. (This observation will be verified in our following subsection) Recall that for the criterion for small-signal stability of a SMIB system is given by:

$$\frac{dP}{d\delta} > 0 \tag{5.9}$$

According to this criterion, the $P\delta$ curves in Figure 5.3 reveal that both of the SMIB channel systems are small-signal stable, indicating that the base case of the comprehensive system in Figure 5.2 (a) is stable as well.

The correlation between the real system and the channel systems will be

confirmed by modal analysis of the real system, as described below.

- The most critical eigenvalue of the state matrix [*A*] is used as the stability indicator of the real system.
- The operating points of channel $P\delta$ curves are used as the stability indicator of the channel systems.
- In order to obtain a trajectory of operating points for comparison, the system generation was gradually increased and, for each new operation point, the channel Pδ curves and the eigenvalue of the state matrix [*A*] of the real system were calculated.

Figure 5.4 shows the trajectory of the eigenvalues of the matrix [*A*]. In this figure, green dots represent stable operating points (all the eigenvalues of state matrix [*A*] have negative real parts) and red crosses represent unstable operating points (there is at least one eigenvalue of state matrix [*A*] that has a positive real part).

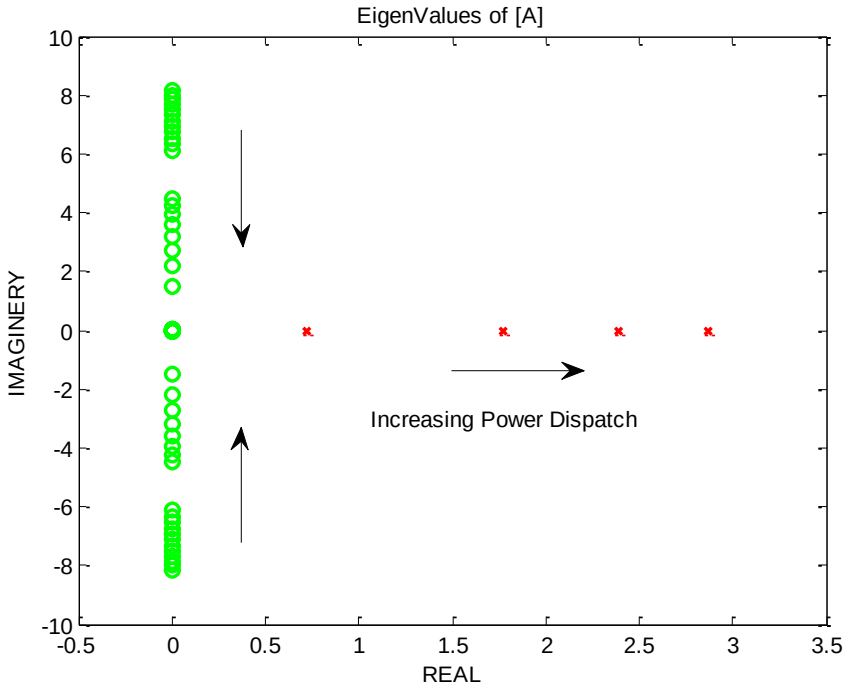

Figure 5.4 Most critical eigenvalue of state matrix [*A*]

Figure 5.5 shows the channel Pδ curves and the operating points for successive increases in the generation of the channel systems. Note that when the operating conditions changes in the real system, in the channel domain, the generators voltage phasors also change since they are defined by $[\hat{U}]=[T]\cdot[\hat{V}_G]$. Therefore, instead of a single Pδ curve, one has a family of Pδ curves in the channel domain, one for each operating condition of the real system. In addition, in these figures, green dots represent stable operating points and red crosses represent unstable operating points as determined by the modal analysis of the real system.

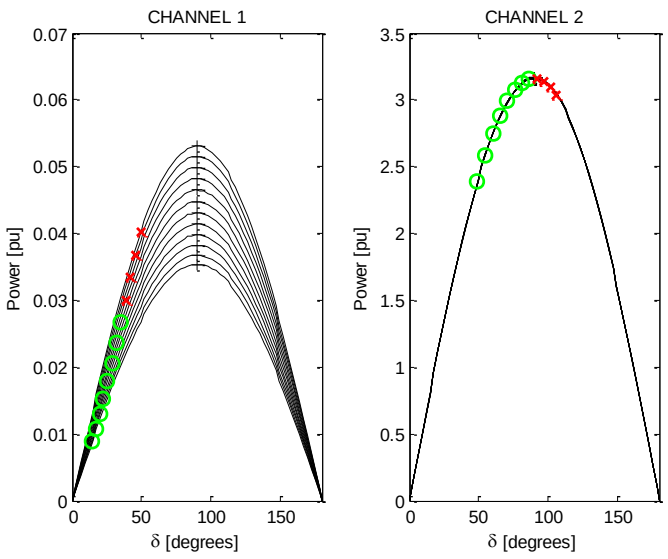

Figure 5.5 Operating points of channel $P\delta$ curves

Figure 5.4 and Figure 5.5 together have reveal that, when one eigenvalue moves to the right part of the real-imaginary plan, the operating point of one channel (Channel 2) moves to the right part of the Pδ curve. Therefore, the monitoring of the operating points into the channel domain was able to predict the behavior of the real system.

An analytical stability index in the channel system can be derived based on the signal of the sensitivity $S_{CH}=\partial P_{CH}/\partial\delta_{CH}$, as for any SMIB system. If S_{CH} is positive for a given operating point, this point is stable (*i.e.*, it is located in the left side of the corresponding channel Pδ curve). Otherwise, if S_{CH} is negative, the operating point is unstable. The sensitivity S_{CH} is analytically given by:

$$S_{CH}=\frac{\partial P_{CH_i}}{\partial \delta_{CH_i}}=\frac{\left|\hat{U}_i\right|\left|\hat{F}_i\right|}{\left|\lambda_i\right|}\sin\left(\delta_{CH_i}+\angle\lambda_i\right) \qquad (5.10)$$

Figure 5.1 shows the comparison of the real part of the critical eigenvalue of the state matrix [A] of the real system and the channel index S_{CH} of Channel 2, which is defined as the critical channel (as will be discussed in the next section), for different system generation level β. For the real system, the operating points and the generation increase pattern was determined by using a continuation power flow.

Table 5.2 Small-signal stability limits given by the real system index and by the channel system index

Generation Level β	**Real System Index Real(eig([A]))**	**Channel System Index ($\partial P_{CH}/\partial \delta_{CH}$)**
1.2887	0.0000	0.2400
1.3174	0.0000	0.1283
1.3293	0.0000	0.0171
1.3251	1.5766	-0.0923
1.3058	2.3747	-0.1985
1.2726	2.9440	-0.3003

From this table, one can see that the proposed index is able to determine the maximum stability limit with good accuracy, as compared. More details and validations will be presented in the next sub-sections.

5.3 Issues for Practical Implementation

In order to apply the proposed technique to the practical power systems, more issues for practical implementation should be considered. This subsection will

discuss the essential issues for practical implementation such as decoupling generators in channels, selecting load models, and identifying critical channels for stability analysis.

5.3.1 Generator Decoupling Technique

Although the CCT decouples the transmission network into several independent channel circuits, when it is applied to the generators, which are already physically decoupled in the real domain, the channel generators becomes coupled. This coupling can be better understood by representing the generators, which are modeled as PV buses, by an equivalent variable shunt negative admittance Y_G. Thus, just for the reason of the easy explanation, we can represent the PV buses as an equivalent admittance, as follows.

$$[\hat{I}_G] = [Y_G] \cdot [\hat{V}_G] \tag{5.11}$$

where, $[Y_G]$ is a diagonal matrix and each diagonal element can be calculated by $Y_{Gii} = -P_{Gi}/|V_{Gi}|^2 + \mathrm{j}Q_{Gi}/|V_{Gi}|^2$.

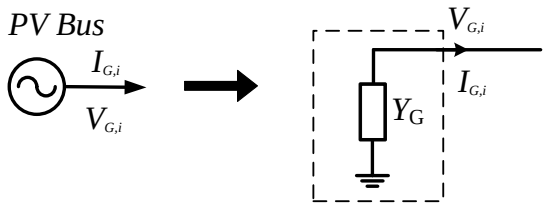

Figure 5.6 Negative admittance equivalence of PV generator

Applying CCT on the both sides of (5.11) yields:

$$[T]\cdot[\hat{I}_G]=\left([T]\cdot\left[Y_G\right]\cdot[T]^{-1}\right)\cdot[T]\cdot[\hat{V}_G] \tag{5.12}$$

Then,

$$[\hat{J}]=\left[Y_C\right]\cdot[\hat{U}] \tag{5.13}$$

or,

$$\begin{bmatrix} J_1 \\ J_2 \\ \vdots \\ J_M \end{bmatrix}=\begin{bmatrix} Y_{C11} & Y_{C12} & \cdots & Y_{C1M} \\ Y_{C21} & Y_{C22} & \cdots & Y_{C2M} \\ \vdots & \vdots & \ddots & \vdots \\ Y_{CM1} & Y_{CM2} & \cdots & Y_{CMM} \end{bmatrix}\begin{bmatrix} U_1 \\ U_2 \\ \vdots \\ U_M \end{bmatrix} \tag{5.14}$$

Although $[Y_G]$ is a diagonal matrix, representing the generators decoupling in the real domain, $[Y_C]$ is a full matrix, representing the generators coupling in the channel domain.

Our observation reveals that the generators coupling in the channel domain is very weak, but still causes unpredicted behavior of channel systems. In order to solve this problem, the proposed solution is to represent the coupling from all others channels into each channel generators by a Norton Equivalent Circuit, as shown in Figure 5.7, since for the *i-th* channel the coupling depends only of the others *j-th* channels, with $i\neq j$. Thus, mathematically, Equation (5.14) can be decomposed as follows:

$$[\hat{J}]=\left(\begin{bmatrix} Y_{C11} & 0 & \cdots & 0 \\ 0 & Y_{C22} & \cdots & 0 \\ \vdots & \vdots & \ddots & \vdots \\ 0 & 0 & \cdots & Y_{Cnn} \end{bmatrix}+\begin{bmatrix} 0 & Y_{C12} & \cdots & Y_{C1n} \\ Y_{C21} & 0 & \cdots & Y_{C2n} \\ \vdots & \vdots & \ddots & \vdots \\ Y_{Cn1} & Y_{Cn2} & \cdots & 0 \end{bmatrix}\right)\cdot[\hat{U}] \tag{5.15}$$

or,

$$\hat{J}_i = \hat{J}_{G_i} + \hat{J}_{C_i} = diag\left(\left[Y_C\right]\right)\cdot[\hat{U}] + \hat{J}_{C_i} \tag{5.16}$$

where,

$$[\hat{J}_G] = diag\left(\left[Y_C\right]\right)\cdot[\hat{U}] \tag{5.17}$$

$$[\hat{J}_C] = [\hat{J}] - diag\left(\left[Y_C\right]\right)\cdot[\hat{U}] \tag{5.18}$$

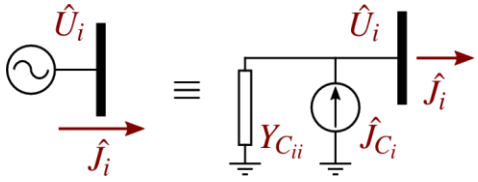

Figure 5.7 Channel generator represented by the Norton Equivalent

By converting the admittance Y_{Cii} back into PV bus, the equivalent circuit for channel systems is obtained in Figure 5.8 (*a*). For the reason of simplicity, Thevenin equivalence is applied to the dashed box as seen in Figure 5.8 (*a*). Then the voltage of the reference bus is modified as $F_{eqi} = F_i + \lambda_i J_{Ci}$. As seen in Figure 5.8 (*b*), the final equivalent circuit is therefore obtained, which has no generator coupling in channel domain.

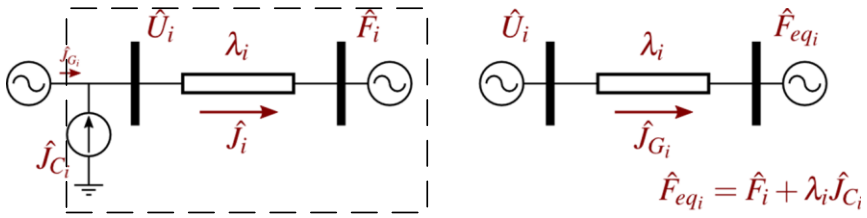

(*a*) Current sources equivalent circuit (*b*) Final equivalent circuit

Figure 5.8 Equivalent circuit for i^{th} channel system

In summary, the procedures to decouple the generators in channel domain are given as follows:

Step 1: Calculate the equivalent negative admittances Y_G for each *PV* bus in real system;

Step 2: Obtain $[Y_C]$ using the equation $[Y_C] = [T][Y_G][T]^{-1}$;

Step 3: Compute $[J_c]$ using $[\hat{J}_C] = [\hat{J}] - diag([Y_C]) \cdot [\hat{U}]$;

Step 4: Compute the modified channel reference voltage $F_{eqi} = F_i + \lambda_i J_{Ci}$, and obtain the final equivalent circuit as seen in Figure 5.8 (b);

5.3.2 Load Model Selection

In the previous explanation, the load are converted to constant impedance and integrated into the [*Z*] matrix as given in equation (5.2). However, it is well recognized that the load model has a large impact on the angle stability analysis. On the other hand, accurate representation of all loads in a large system is impractical due to lack of adequate load information. Therefore, it is recommended by IEEE in reference [65] that the load for small-signal stability analysis be modeled as Z-I model. Z-I model assumes that the active power of loads is modeled as constant current source (I), and that the reactive power of loads is modeled as constant impedance (Z). Thus, for a *PQ* load bus, its circuit representation seen in Figure 5.9 is given by:

$$[\hat{I}_L] = -\left([\hat{I}_{LP}] + [Y_{LQ}] \cdot [\hat{V}_L]\right) \tag{5.19}$$

where,

$$Y_{LQ_m} = -j\frac{Q_m}{\left|\hat{V}_{L_m}\right|^2}, \quad \hat{I}_{LP_m} = -\frac{\hat{V}_{L_m}}{\left|\hat{V}_{L_m}\right|^2} P_m \tag{5.20}$$

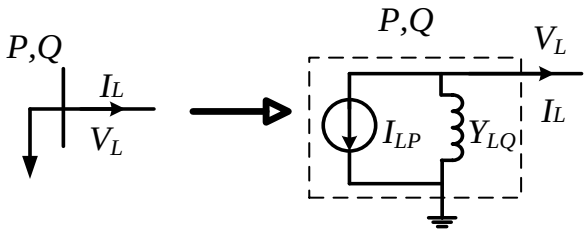

Figure 5.9 Converting *PQ* load to Z-I model

In order to include this load model into the network equation (5.2) as presented in subsection 5.2, equation (5.2) should be rewritten as follows:

$$[\hat{V}_G] = [\hat{V}_K] + [Z]\cdot[\hat{I}_G] \tag{5.21}$$

where,

$$[\hat{V}_K] = [K]\cdot\hat{V}_S + [Z]\cdot[Y_{GL}]\cdot\left([Y_{LL}]+[Y_{LQ}]\right)^{-1}\cdot[\hat{I}_{LP}]$$

$$[K] = -[Z]\cdot\left([Y_{GS}]-[Y_{GL}]\cdot\left([Y_{LL}]+[Y_{LQ}]\right)^{-1}\cdot[Y_{LS}]\right)$$

$$[Z] = \left([Y_{GG}]-[Y_{GL}]\cdot\left([Y_{LL}]+[Y_{LQ}]\right)^{-1}\cdot[Y_{LG}]\right)^{-1}$$

The admittance sub-matrixes Y_{GL}, Y_{GS}, Y_{GG}, Y_{LL}, Y_{LS}, and Y_{LG} are obtained from the nodal network equations:

$$\begin{bmatrix}[\hat{I}_L]\\ [\hat{I}_S]\\ [\hat{I}_G]\end{bmatrix} = \begin{bmatrix}[Y_{LL}] & [Y_{LS}] & [Y_{LG}]\\ [Y_{SL}] & [Y_{SS}] & [Y_{SG}]\\ [Y_{GL}] & [Y_{GS}] & [Y_{GG}]\end{bmatrix}\cdot\begin{bmatrix}[\hat{V}_L]\\ [\hat{V}_S]\\ [\hat{V}_G]\end{bmatrix} \tag{5.22}$$

and, the load constant susceptances and currents are put as,

$$[Y_{LQ}] = diag\left(Y_{LQ_1}, Y_{LQ_2}, ..., Y_{LQ_m}\right)$$

$$[\hat{I}_{LP}] = \begin{bmatrix} \hat{I}_{LP_1} \\ \vdots \\ \hat{I}_{LP_m} \end{bmatrix}$$

5.3.3 Critical Channel Identification

Although CCT can decouple the complicated power network into a family of SMIB channel systems, it's not necessary to monitor the behavior of all the channel systems. This is because only a channel or a few channels are responsible for transferring most of the power in the channel domain.

For example, for the case analyzed in Subsection 5.2.2, one can see that Channel 2 transfer much more power than Channel 1, as seen in Figure 5.10. Thus, only Channel 2 must be monitored to infer about the stability of the real system, as can be seen in Figure 5.5.

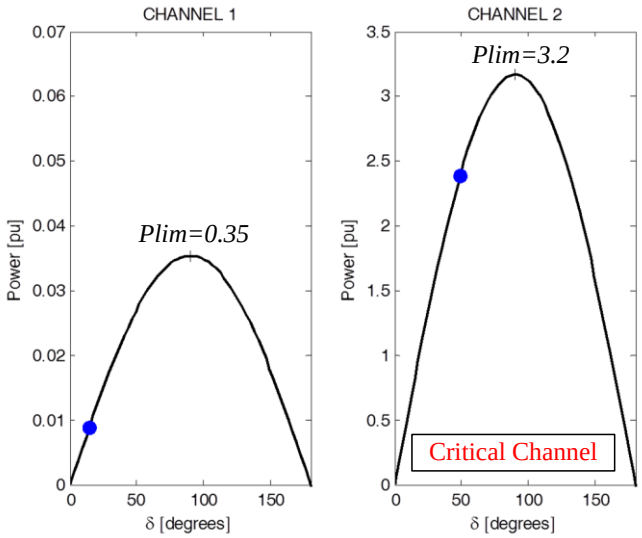

Figure 5.10 Critical channel identification of comprehensive system

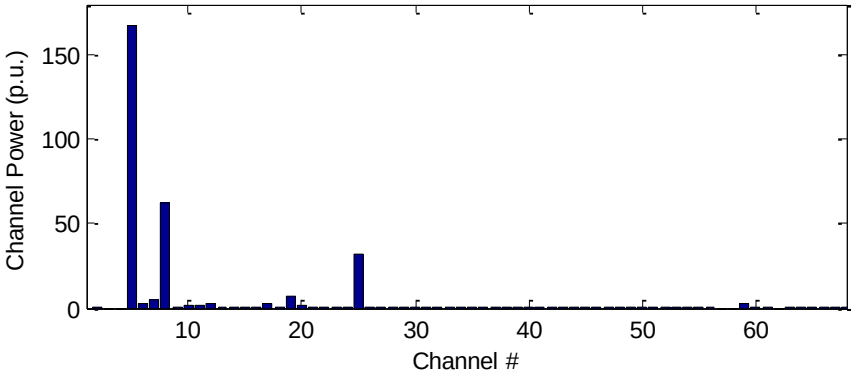

Figure 5.11 Transferring power of channels (IEEE 300 bus system)

Another example is the IEEE 300 Bus system with 69 generators (therefore 68 channels). Figure 5.11 shows the power transfer of the channel systems. It's observed that only 4 channels are responsible for transferring more than 95% of all power in the channel domain. Hence, only these channels must be monitored to analyze the small-signal angle stability of the real network.

Consequently, only the channel or a set of channels with considerably large power transfer limit must be monitored to analyze the small-signal angle stability of the real network. These channels are called “critical channels”, which contribute to the real system’s stability most effectively.

Another possibility of defining the critical channels is based on the stability margin by using the Pδ curves. The channels with the smallest stability margin are defined as “critical channels”, which must be monitored. Based on the example of the 3-generator system, the stability margin in the channel domain can be defined as:

$$M_s = \frac{\Delta P}{|P_{\text{base}}|} \times 100\% = \frac{P_{\text{lim}} - P_{\text{base}}}{|P_{\text{base}}|} \times 100\% \qquad (5.23)$$

Our experience with several different systems is that any of the previous criteria, i.e., power transfer limit or stability margin, will select the same critical channels. So that the criteria based on power transfer limit will be used to identify the critical channels in the rest of this work.

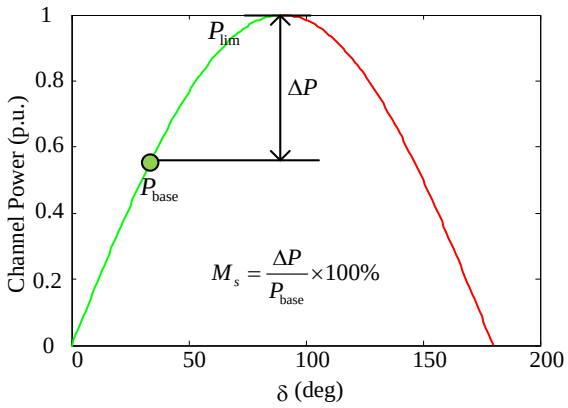

Figure 5.12 Representation of the stability margin in the channel domain

5.4 General Procedures

Based on the previous sections, the general procedure to use the CCT for small-signal stability analysis and monitoring can be summarized as follows:

Step 1: Obtain [Z] and [K] from the network bus nodal admittance matrix [Y] and from the load parameters [Y_{LQ}] and [$\hat{\boldsymbol{I}}_{LP}$];

Step 2: Compute the transform [T] and the channel impedance matrix [Λ] – since this transform depends only on the network impedance and load parameters, it should be recomputed only when there is a change in the loading or network topology.

Step 3: Obtain the phasor voltages in the generators buses and in the slack bus.

These voltages can be measured by PMUs or collected from modern EMSs in real time. If the method is intended to be applied in offline analysis, these values can be obtained from a power flow calculation.

Step 4: Calculate the channel systems operating points $[\hat{U}]$, $[\hat{F}_{eq}]$ and identify the critical channels based on the power transfer level or stability margin.

Step 5: Computes the power, the angle and the channel sensitivity stability indicator given by (5.10).

Step 6: Obtain the $P\delta$ curves if the stability margin should be estimated.

Step 7: Analyze the small-signal stability of the critical channels and concludes about the stability of the operating point of the real system.

Step 8: Scale up the generation level (offline analysis) or Rescan PMU measurement (online monitoring). Then continue the iteration from Step 3 to Step 7, if the channel sensitivity stability indicator is positive.

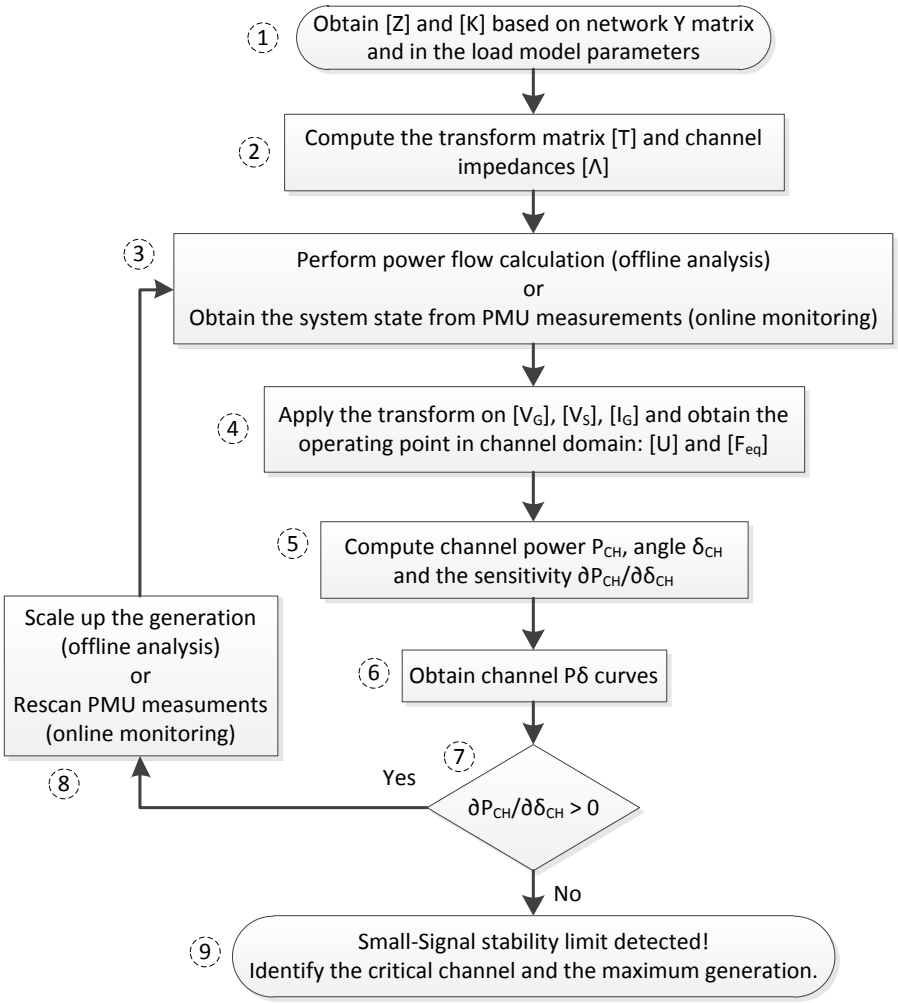

Figure 5.13 Procedures of the proposed method

This procedure can be further summarized in Figure 5.13. Note that this procedure can be used for either offline studies or online monitoring. The differences of these two scenarios are seen in step 3 and step 8.

5.5 Further Validation of Proposed Method

This subsection presents further case studies, using larger test systems to validate the proposed method. Firstly, The New England system, as seen in Figure 5.14, is selected for the analysis since it has been considered as a benchmark system for stability studies.

In order to obtain the small-signal stability limit of the test systems, the continuation power flow (CPF) program is utilized, which can gradually increase the power flow until it reaches the maximum power flow (normally referred to as CPF "nose point"). In the meanwhile, the generation parameter β is gradually increased from 1.0 (base case) to its maximum value β_{max}. Normally, during this process, the small-signal stability limit will be detected and identified by the state matrix [*A*] in modal analysis.

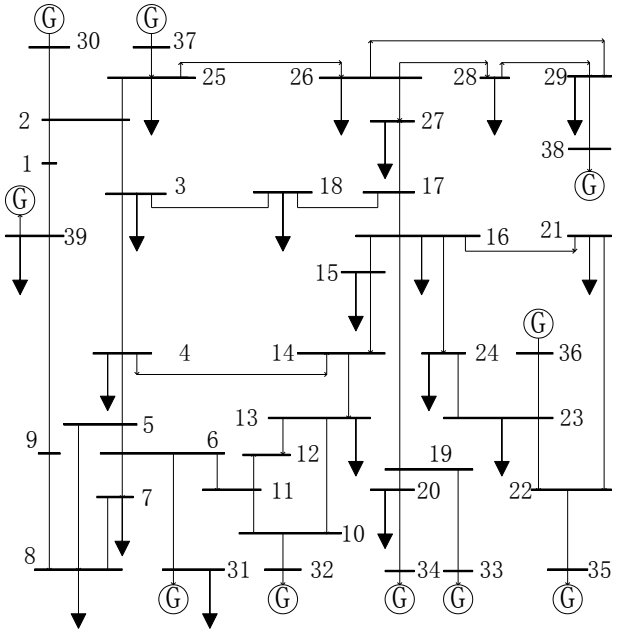

Figure 5.14 One-line diagram of New England system

Note that load power is not increased in this analysis, since if we increase load and generation together, the test system will usually reach voltage collapse before the small-signal angle stability limit. Worth of mention is that, in the real domain, the system load reactive power was modeled as constant impedance the and active power as constant current, as suggested in [8].

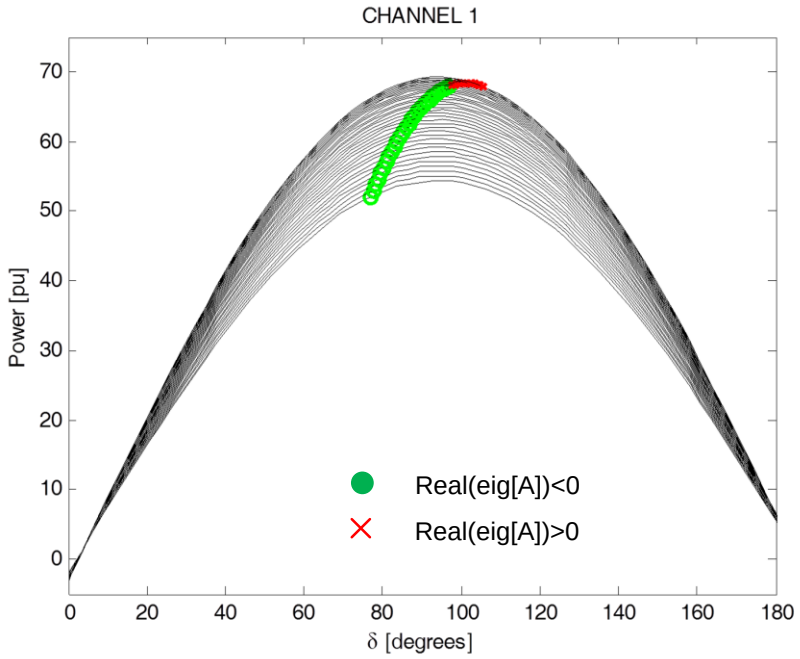

Figure 5.15 Critical channel small-signal stability analysis for the New England syste

Then we can apply proposed technique to analyze small-signal stability of the New England system. The P-δ curves in the channel domain for the critical channel are shown in Figure 5.15. The green circle and the red crosses indicate the operating point for each value of generation. In addition, the green circles means

that the model analysis of the dynamic matrix [*A*] for the real system classified the system as stable for the corresponding operating point, while the red crosses means that the real system is unstable based on modal analysis. Based on this figure, one can see that when the real system becomes unstable, the critical channel operates in the right part of the curve, indicating that, in the channel system is also unstable.

Table 5.3 Small-signal stability limits for the real system and for the channel system: New England system

Generation Parameter β	Re[eig([A])]	Channel Index ($\partial P_{CH.}/\partial \delta_{CH.}$)
1.2953	0	0.0337
1.3043	0	0.02
1.3127	0	0.0064
1.3205	0	-0.0072
1.3277	0	-0.0208
1.3341	0	-0.0344
1.34	0	-0.0479
1.3451	0.5099	-0.0614
1.3495	0.9304	-0.0748
1.3532	1.217	-0.088

Table 5.3 shows the variation of the real part of the critical eigenvalue of the dynamic matrix [*A*] of the real system and the index $\partial P_{CH}/\partial \delta_{CH}$ of the critical channel, for different system generation levels β. The real part of the critical eigenvalue becomes positive for a generation parameter β_{max} equals 1.3451, while using the critical channel to monitor this maximum generation, the sensitivity $\partial P_{CH}/\partial \delta_{CH}$ becomes negative for the critical channel when the generation

parameter β_{max} is equal 1.3205. The maximum generation without the system becomes unstable estimated by the proposed method is slightly lower than the obtained by the modal analysis. Our experience with other systems shows that the proposed method is a little bit conservative in estimating that limit.

To further validate the proposed method, we conduct more case studies on test systems that have been widely used in other technical literatures. Table 5.4 shows the small-signal stability limits of those test systems, calculated by modal analysis of the dynamic matrix and by the proposed method. The calculation results have revealed that the proposed method can estimate the maximum generation with good accuracy.

Table 5.4 Small-signal stability limits for the real system and for the channel domain load represented by current/impedance I/Z

Test system	Small-signal stability limit $\beta_{\max}$	
	Modal analysis	Proposed method
WSCC 9-bus system	2.570	2.566
New England system	1.341	1.314
IEEE 57-bus system	4.286	3.693
IEEE 300-bus system	0.798	0.703

5.6 Potential Applications

This subsection will present two potential applications based on the proposed method: N-1 contingency analysis constrained by small-signal stability, and

visualization of small-signal stability index.

5.6.1 N-1 Contingency Analysis

To further validate the proposed method, this section presents a *N*-1 contingency analysis taking into consideration small-signal angle issues by using the New England system. The maximum generation determined by the modal analysis of the dynamic matrix [*A*] was compared with the value determined by monitoring the critical channel.

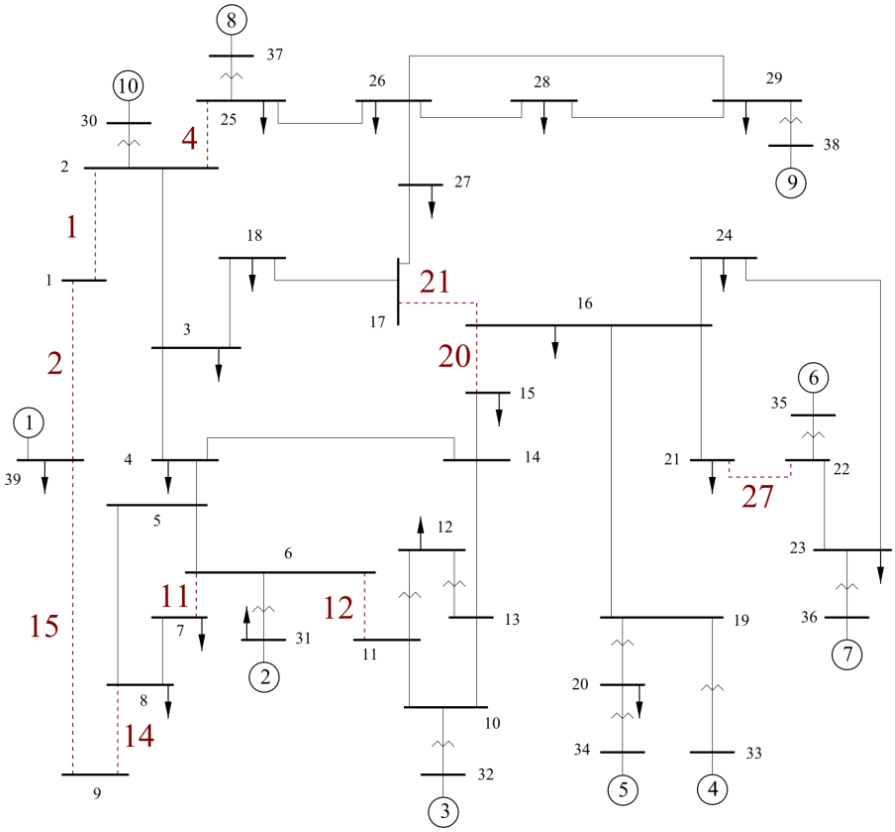

Figure 5.16 New England system and contingencies of interest

The idea is to see if the proposed method can be used as a screening tool for N-1

contingency analysis from the viewpoint of the small-signal angle stability. Thus, besides comparing the maximum generation value, the contingencies were classified from the most critical to the less critical, where the most critical single contingency is the one with the smaller stability margin. The stability margin was calculated as the difference between the maximum generation parameter β_{max} and the base case generation parameter β_{base} = 1. The system was simulated for each one of all the N-1 possible contingencies that does not split the system into two electric islands.

The severity ranking of the contingencies is presented in Figure 5.5 for the top ten most severe contingencies. The “Real System” ranking was built monitoring the eigenvalues of the [*A*] matrix while the “Channel Domain” ranking was built monitoring the channel circuit sensitivity. Independently of the used method, the rank is practically the same. Therefore, the channel domain monitoring is effective in detect the critical contingencies from the viewpoint of small-signal stability. The most several line contingencies are also indicated in Table 5.5.

Table 5.5 Contingency ranking using modal analysis and proposed method from the viewpoint of small-signal angle stability

	Rank of the Top Severe N-1 Contingencies
Real System	1, 2, 14, 15, 4, 21, 27, 11, 12, 20
Channel Domain	1, 2, 15, 14, 27, 4, 21, 20, 12, 11

The maximum loading for each N-1 contingency scenario is also presented in Table 5.6. The small-signal stability margin estimated by the channel monitoring is always slightly conservative when compared to the one predictable by the modal analysis.

Table 5.6 Small-signal stability limits for the critical contingencies

Contingency in Line	Maximum Generation β_{max} Real System	Maximum Generation β_{max} Channel Domain
1	1.09275	1.08127
2	1.09827	1.08129
14	1.14581	1.11943
15	1.15153	1.11899
4	1.27167	1.21496
21	1.27879	1.2332
27	1.27884	1.20017
11	1.30787	1.28987
12	1.31001	1.27882
20	1.31437	1.26904

5.6.2 Visualization of Stability Index

Small-signal stability margin is a key index to be monitored in the area of power system operation and control. Traditionally, the small-signal stability margin is evaluated by gradually increase the power flow (i.e. continuation power flow study) until it reaches the stability limit as indicated by modal analysis or general practical criterion (i.e. Crary's criterion) [66]. Obviously, this method is computationally expensive for real-time applications.

One of the main advantages of the proposed technique is the possibility of readily and easily visualizing the information about the stability margin based on the Pδ curves of the critical channel. By the proposed method, the stability index as shown in (5.23) can be obtained easily without heavy continuation power flow (CPF) computation. Therefore, this stability index can be used to monitor the system stability margin as a powerful visualization tool.

As an example, Figure 5.17 shows the variation of the power margin of the critical channel as the generators dispatch is increased for the New England system. One can see that the system limit as pointed by CCT method is very close to but a little bit conservative than that pointed by the modal analysis. Hence, the power margin for the critical channel can be used as quantitative indicator of the system stability to enhance the situational awareness.

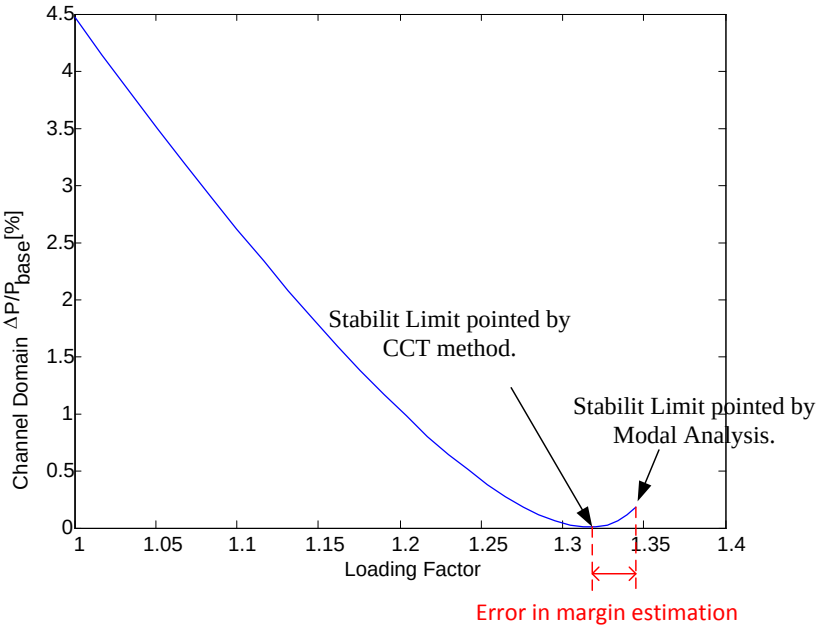

Figure 5.17 Power margin reduction in the critical channel with the increasing in system loading

Other real-time applications and visualization techniques can be developed to monitor the conditions of system operation using the phasor data through the decomposition of the power network into the channels. For instance, an approach for visualizing the system loading is presented in Figure 5.18. For this approach, the following index Γ is defined:

$$\Gamma = \frac{P_{\text{base}}}{P_{\text{limit}}} = \frac{1}{M_P + 1} = \frac{1}{\beta_{\max}} \tag{5.24}$$

where, $0 \leq \Gamma \leq 100\%$.

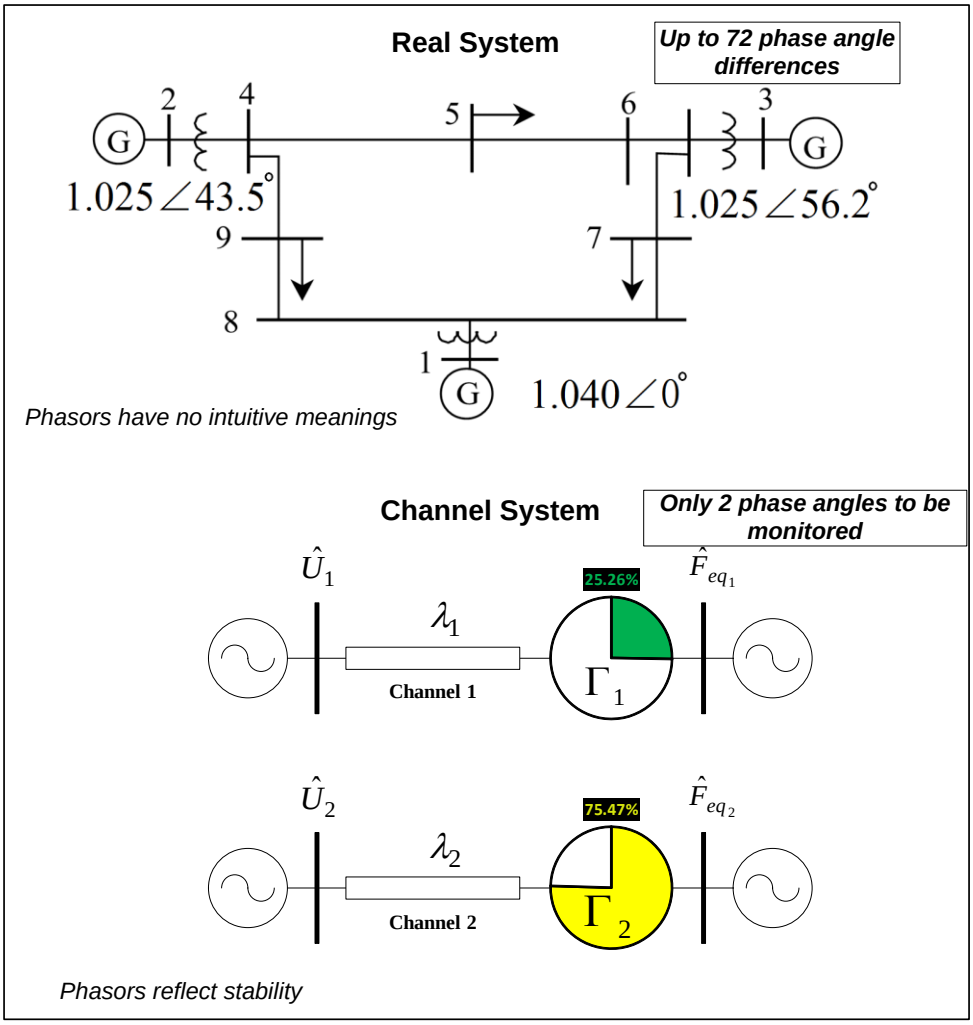

Figure 5.18 Monitoring small-signal stability in real system and channel system

The index Γ indicates how close a given channel, and consequently the real system, is to the maximum power transfer from the viewpoint of small-signal angle stability. If Γ = 100% for one channel, the system is in the vicinity of the instability, since one channel has reached their limit. The values visualized reflect the conditions from the base case operation point shown in Figure 5.18. For this case, the system loading is such that the power flowing through Channel 2 is around 75% of its transfer limit.

From the example as shown in Figure 5.18, it's observed that the proposed technique has an obvious advantage that the variables to be monitored are highly reduced. For example, if PMU devices are installed at X buses, phasor measurement yields as many as $X \times (X\text{-}1)$ phase angle differences. Such a large data volume makes it very hard and even infeasible to extract useful information directly from phasor data. However, as mentioned, the proposed technique only requires a small portion of channels (critical channels) to be monitored for the purposed of stability analysis. As a result, the proposed technique considerably reduces the number of variables to be monitored, as compared to the regular phase angle visualizing tools.

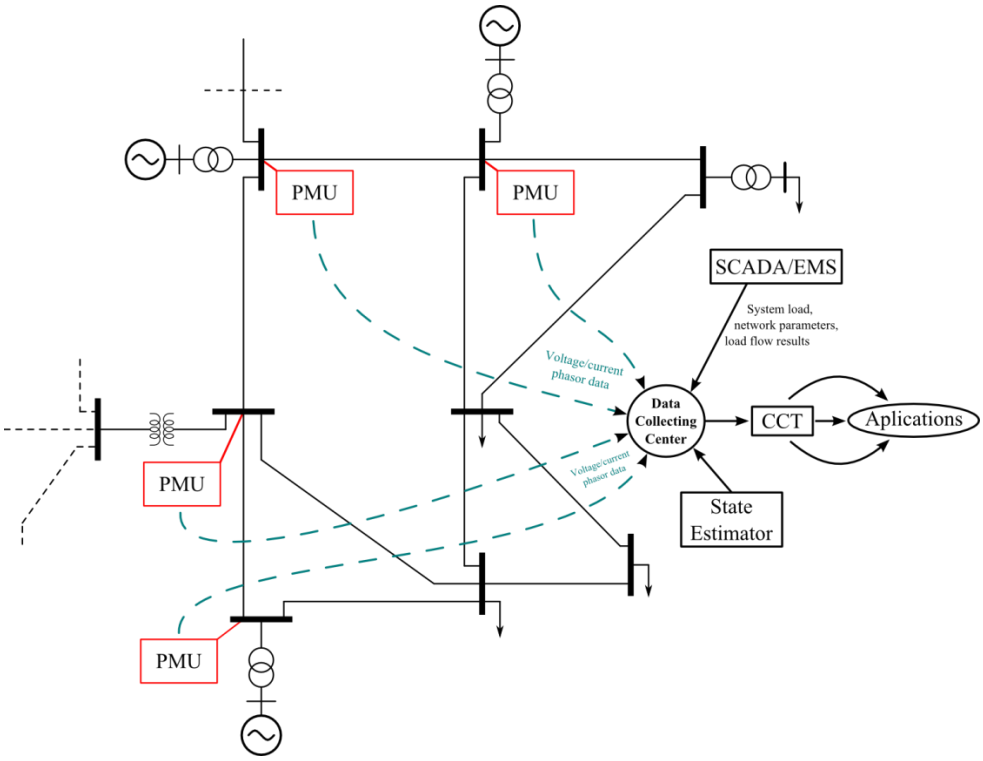

Figure 5.19 System architecture for CCT-based real-time angle stability monitoring.

A possible architecture for real-time angle stability monitoring is shown in Figure 5.19. The data collected from PMU are transmitted to the system control center, along with other information provided by the SCADA/EMS and from state estimator such as network parameters and load models, which are processed through the application of the Channel Components Transform. After applying the proposed decomposition method, the conditions of the system in the channel domain can readily be displayed in the form of Pδ curves or other intuitive visualized forms as shown in Figure 5.18 to increase the situational awareness.

5.7 Summary

This chapter has proposed and demonstrated a phasor-based method to analyze and monitor the small-signal stability of a complex power system. The proposed method is based on the observation that a generic power network can be represented by a Thevenin equivalent circuit and decoupled by eigen-decomposition into a set of two-node, single-branch equivalent circuits. This technique has been successfully applied to small-signal stability study by providing intuitive P-δ curve and yielding the stability margin without heavy computation. The case study results have shown that the proposed method provides the same information on small-signal stability as the modal analysis with slight conservativeness. Further, potential applications based on the proposed method are proposed, including N-1 contingency analysis and visualization of stability index.

The main advantage of the proposed technique is its simplicity and the possibility of using visualization techniques for monitoring. On the other hand, the major drawback of this proposed method is that it may be difficult to consider complex control schemes in the channel domain. However, it is still a useful supplement for regular small-signal stability analysis program.

Chapter 6

Conclusions and Future Work

This thesis discussed the topics related to modeling power system loads, especially those for large industrial facilities. A systematic approach using the template-based concept was established for constructing the equivalent dynamic model of paper mills (the Kraft Type). In addition, this thesis also investigated the issues of modeling and aggregating DC drive loads. The major conclusions and achievement of this thesis are summarized as follows:

- An extensive survey on paper mills was conducted to extract the common features of their electrical systems. The features such as the typical industrial processes, the typical structures, and parameters of the system circuit load composition are extracted and determined.

- Based on these common features identified from the survey, a template for paper mills (Kraft type) was established. The template-based load model of paper mills was developed and verified through ETAP simulation. The simulation results demonstrated the accuracy of the obtained model as compared to that of the WECC guideline models.

- The issue of modeling and aggregating DC drive loads was discussed. A DC drive trip curve was proposed to determine the tripping criteria of DC drives. For the ride-through DC drives, a dynamic load model was developed from the average-value model (AVM) of DC drives and represented in the form of the transfer function. Techniques to aggregate the proposed model and incorporate the models with series impedance were proposed and verified through simulation.

In addition, another stability-related research work of mine was presented in Chapter 5. This work developed a method to analyze and monitor the small-signal stability based on a network decomposition technique. The mathematical basis, Implementation requirements and general procedures of the proposed method were introduced. Simulation studies were conducted and verified the usefulness of the proposed method by using IEEE test systems. The potential applications of the proposed method in the EMS system were also discussed.

More work is needed to extend and modify the findings of this thesis in the future. The suggestions for future work are summarized as follows:

- A complete template database needs to be established. This thesis builds only the template for paper mills. In the future, it would be desirable to include in

the template database other facilities such as the TMP-type paper mill, aluminum smelter, and steel mills.

- In this thesis, VFDs are regarded as transparent devices, because of the lack of an adequate load model. In the future, the equivalent model of VFDs could be developed by following a method similar to the modeling of DC drives. As a result, the dynamic characteristics of VFDs could be included in the template-based load model.

- The technique for aggregating DC drive models is based on the model order reduction method with Pade approximation. Its major drawback is that it cannot guarantee the stability of the reduced model. In other words, the reduced model may become unstable even if the original model is stable. For this reason, other model order reduction methods might be considered, for example, Routh method and optimization-based method.

- The PI controller parameters for DC drives are chosen as sample values in the thesis. In fact, it is more appropriate to design the controller parameters based on the user input data. In the future, the typical data generator should adopt an additional module to design the controller parameters by following the engineering controller tuning procedures.

References

[1] V. Knyazkin, *et al.*, "On the parameter estimation and modeling of aggregate power system loads," *Ieee Transactions on Power Systems,* vol. 19, pp. 1023-1031, May 2004.

[2] C. W. Taylor, *et al.*, "Concepts of Undervoltage Load Shedding for Voltage Stability," *Ieee Transactions on Power Delivery,* vol. 7, pp. 480-488, Apr 1992.

[3] W. S. Xu and Y. Mansour, "Voltage Stability Analysis Using Generic Dynamic Load Models," *Ieee Transactions on Power Systems,* vol. 9, pp. 479-486, Feb 1994.

[4] D. Karlsson and D. J. Hill, "Modelling and identification of nonlinear dynamic loads in power systems," *Power Systems, IEEE Transactions on,* vol. 9, pp. 157-166, 1994.

[5] X. Wang, "Modern power system analysis [M]," ed. Beijing: Science Press, 2003.

[6] L. Pereira, *et al.*, "An interim dynamic induction motor model for stability studies in the WSCC," *IEEE Transactions on Power Systems,* vol. 17, pp. 1108-1115, Nov 2002.

[7] A. Ellis, *et al.*, "Dynamic Load Models: Where Are We?," in *Transmission and Distribution Conference and Exhibition, 2005/2006 IEEE PES*, 2006, pp. 1320-1324.

[8] C. Concordia and S. Ihara, "Load Representation in Power System Stability Studies," *Power Apparatus and Systems, IEEE Transactions on,* vol. PAS-101, pp. 969-977, 1982.

[9] Y. Li, *et al.*, "Representative static load models for transient stability analysis: development and examination," *Iet Generation Transmission & Distribution,* vol. 1, pp. 422-431, May 2007.

[10] W. W. Price, *et al.*, "Load modeling for power flow and transient stability computer studies," *Power Systems, IEEE Transactions on,* vol. 3, pp. 180-187, 1988.

[11] W. W. Price, *et al.*, "Standard Load Models for Power-Flow and Dynamic Performance Simulation," *Ieee Transactions on Power Systems,* vol. 10, pp. 1302-1313, Aug 1995.

[12] A. Borghetti, *et al.*, "Generic dynamic load models in long-term voltage stability studies," *International Journal of Electrical Power & Energy Systems,* vol. 22, pp. 291-301, May 2000.

[13] W. S. Xu and Y. Mansour, "Voltage Stability Analysis Using Generic Dynamic Load Models," *Power Systems, IEEE Transactions on* vol. 9, pp.

479-486, Feb 1994.

[14] A. Borghetti, *et al.*, "On dynamic load models for voltage stability studies," *Power Systems, IEEE Transactions on* vol. 12, pp. 293-299, Feb 1997.

[15] J. M. Undrill and T. F. Laskowski, "Model Selection and Data Assembly for Power System Simulations," *Power Apparatus and Systems, IEEE Transactions on,* vol. PAS-101, pp. 3333-3341, 1982.

[16] D. C. Franklin and A. Morelato, "Improving Dynamic Aggregation of Induction-Motor Models," *IEEE Transactions on Power Systems,* vol. 9, pp. 1934-1941, Nov 1994.

[17] W. Xu and Y. Mansour, "Voltage stability analysis using generic dynamic load models," *Power Systems, IEEE Transactions on,* vol. 9, pp. 479-493, 1994.

[18] E. Welfonder, *et al.*, "Investigations of the Frequency and Voltage Dependence of Load Part Systems Using a Digital Self-Acting Measuring and Identification System," *IEEE Transactions on Power Systems,* vol. 4, pp. 19-25, Feb 1989.

[19] T. Omata and K. Uemura, "Effects of series impedance on power system load dynamics," *Power Systems, IEEE Transactions on,* vol. 14, pp. 1070-1077, 1999.

[20] I. A. Hiskens and J. V. Milanovic, "Load modelling in studies of power system damping," *Power Systems, IEEE Transactions on,* vol. 10, pp. 1781-1788, 1995.

[21] R. M. He, *et al.*, "Composite load modeling via measurement approach," *IEEE Transactions on Power Systems,* vol. 21, pp. 663-672, May 2006.

[22] J. Ma, *et al.*, "Load modeling by finding support vectors of load data from field measurements," *Power Systems, IEEE Transactions on,* vol. 21, pp. 726-735, 2006.

[23] A. A. Stankovic and A. T. Saric, "Transient power system analysis with measurement-based gray box and hybrid dynamic equivalents," *IEEE Transactions on Power Systems,* vol. 19, pp. 455-462, Feb 2004.

[24] A. Qian, *et al.*, "New Load Modeling Approaches Based on Field Tests for Fast Transient Stability Calculations," *Power Systems, IEEE Transactions on,* vol. 21, pp. 1864-1873, 2006.

[25] W. Jin-Cheng, *et al.*, "Development of a frequency-dependent composite load model using the measurement approach," *Power Systems, IEEE Transactions on,* vol. 9, pp. 1546-1556, 1994.

[26] S. A. Arefifar and W. Xu, "Online Tracking of Power System Impedance Parameters and Field Experiences," *Power Delivery, IEEE Transactions on,* vol. 24, pp. 1781-1788, 2009.

[27] J. Y. Lim, *et al.*, "Component-based load modeling including capacitor

banks," in *Power Engineering Society Summer Meeting, 2001*, 2001, pp. 1199-1204 vol.2.

[28] X. Liang, *et al.*, "Dynamic Load Models for Industrial Facilities," *Power Systems, IEEE Transactions on*, vol. PP, pp. 1-12, 2011.

[29] G. J. Rogers, *et al.*, "An Aggregate Induction-Motor Model for Industrial-Plants," *IEEE Transactions on Power Apparatus and Systems*, vol. 103, pp. 683-690, 1984.

[30] S. Lu, "MVWG Report to TSS," WECC Load Modeling Task Force, 2012.

[31] Pulp and Paper Institue of Canada, "Benchmarking Energy Use in Canadian Pulp and Paper Mills," Pulp and Paper Research Institute of Canada, Pointe-Claire, QC2006.

[32] S. Sabir and D. Lee, "Dynamic Load Models Derived from Date Acquired During System Transients," *Power Apparatus and Systems, IEEE Transactions on*, pp. 3365-3372, 1982.

[33] Council of Forest Industries, "BRITISH COLUMBIA FOREST INDUSTRY FACT BOOK - 1998," Council of Forest Industries, Ed., ed. Vancouver, 1998.

[34] OTI Inc. (2012). *ETAP User Guide*. Available: http://etap.com/support/faqs-tutorials-topic.htm#transstabanalysis

[35] N. S. Tunaboylu, *et al.*, "Ride-through Issues for Dc Motor Drives during Voltage Sags," *Ieee Southeastcon '95 - Visualize the Future, Proceedings*, pp. 52-58, 1995.

[36] G. A. Smook, *Handbook for pulp & paper technologists*: Angus Wilde Publications, 1992.

[37] Pulp and Paper Canada, "Pulp and Paper Mill Annual Directory," in *Pulp and Paper Mill Annual Directory*, M. Cindy, Ed., ed. Toronto, 2012.

[38] S. Scott and M. Lott, "Northwest Industrial Motor Database Summary " Oregon State University2008.

[39] US Department of Energy. (1999), MOTOR SYSTEM USAGE IN FOREST PRODUCTS. Available: www.energystar.gov/ia/business/industry/pulpmtr.pdf

[40] S. Saarela, *et al.*, "The First Year of Operation of the Botnia Fray Bentos Pulp Mill in Uruguay," Ruta Puente Puerto, Botnia S.A.2007.

[41] B. L. Vuan, *et al.*, "Load Shedding Scheme for a Large Pulp Mill," Fray Bentos, 2008.

[42] North West Clean Energy Center, "Simpson Tacoma Kraft 60 MW Biomass Combined Heat and Power Plant ", 2012.

[43] M. Rylander, *et al.*, "Power Electronic Transient Load Model for Use in Stability Studies of Electric Power Grids," *Ieee Transactions on Power Systems*, vol. 25, pp. 914-921, May 2010.

[44] P. J. Link, "Application requirements for ASDs in the pulp and paper

industry," in *Industry Applications Conference, 2002. 37th IAS Annual Meeting. Conference Record of the*, 2002, pp. 1244-1249 vol.2.

[45] OTI Coop. (2012). *ETAP tutorials*.

[46] M. L. Ourari, *et al.*, "Dynamic equivalent modeling of large power systems using structure preservation technique," *Power Systems, IEEE Transactions on*, vol. 21, pp. 1284-1295, 2006.

[47] Siemens PTI, "PSS/E Model Library of PSS/E-32," ed. Schenectady, NY, USA, 2009.

[48] C. A. Michael and A. N. Safacas, "Dynamic and vibration analysis of a multimotor DC drive system with elastic shafts driving a tissue paper machine," *Industrial Electronics, IEEE Transactions on*, vol. 54, pp. 2033-2046, 2007.

[49] J. Pedra, *et al.*, "Effects of balanced and unbalanced voltage sags on DC adjustable-speed drives," *Electric Power Systems Research*, vol. 78, pp. 957-966, Jun 2008.

[50] Y. HUANG, *et al.*, "HVDC MODELS OF PSS/E AND THEIR APPLICABILITY IN SIMULATIONS [J]," *Power System Technology*, vol. 5, 2004.

[51] ABB Inc. (2012). *ABB Product Guide: Standard DC Drives DSC 550*. Available: http://www.abb.us/product/seitp322/0bc6c126f67c0c2bc1256e0000700ad9.aspx?productLanguage=us&country=US&tabKey=2

[52] J. Lamoree, *et al.*, "Voltage sag analysis case studies," *Industry Applications, IEEE Transactions on*, vol. 30, pp. 1083-1089, 1994.

[53] Electric Power Research Institute (EPRI), "Printing Press Shutdowns Caused By Sensitivity of DC Drive to Voltage Sags," Knoxville, 2000.

[54] X. Liang, "Implication of VFD Trip Characteristics on Dynamic Simulation," University of Alberta, Edmonton2011.

[55] P. C. Sen, *Thyristor DC drives*: Wiley, 1981.

[56] P. C. Krause, *et al.*, *Analysis of electric machinery and drive systems*: New York, 2002.

[57] S. Zhang, *DC Converter Electric Drive System 2nd edition (in Chinese)*. Wuhan: Huazhong University of Science and Technology Press, 1995.

[58] N. Hong, *Modeling and Simulation of Power Electronics and Electrical Machine Drive Systems (in Chinese)*. Beijing: China Machine Press, 2010.

[59] W. Xu, *et al.*, "Modelling of DC drives for power system harmonic analysis," *Iee Proceedings-Generation Transmission and Distribution*, vol. 146, pp. 217-222, May 1999.

[60] T. Wildi, *Electrical Machines, Drives, and Power Systems*: Prentice Hall, 2007.

[61] Y. Shamash, "Linear-System Reduction Using Pade Approximation to

Allow Retention of Dominant Modes," *International Journal of Control*, vol. 21, pp. 257-272, 1975.

[62] Z. Han, *Power System Analysis (Third Version)*, 3rd ed. Hangzhou: Zhejiang University Press, 2005.

[63] S. Li, *et al.*, "Analysis and Monitoring of Small-Signal Angle Stability by Using the Channel Components Transform and Phasor Data (Submitted)," *IEEE Trans. Smart Grid*, 2012.

[64] W. Xu, *et al.*, "A Network Decoupling Transform for Phasor Data Based Voltage Stability Analysis and Monitoring," *Smart Grid, IEEE Transactions on*, vol. 3, pp. 261-270, 2012.

[65] IEEE Task Force on Load Representation for Dynamic Performance, "Load representation for dynamic performance analysis of power systems," *Power Systems, IEEE Transactions on*, vol. 8, pp. 472-482, 1993.

[66] State Economic and Trade Commission (China), "Guide on Security and Stability for Power System," vol. DL 755-2001, ed: State Grid (China), 2001.

[67] T. Omata and K. Uemura, "Effects of series impedance on power system load dynamics," *Ieee Transactions on Power Systems*, vol. 14, pp. 1070-1076, Aug 1999.

Appendix A

Summary of Data Sources

The data resources for the survey on paper mills are mainly taken from technical reports, design manuals and the professionals who are working or used to work in the paper mills.

I’d like to express my sincere thanks to the electrical engineering experts from paper industry, who shared with me their valuable experience and assisted me in finding useful information in paper mills. Due to the reason of confidentiality, we don’t list their name and working units here.

The technical reports and other documents about the industrial loads and paper mills is mainly obtained from the below reference.

- USA Department of Energy (DOE), United States Industrial Electric Motor Systems Market Opportunities Assessment, 2002
- PAPTAC, Pulp and Paper Mill Annual Directory, 2012
- Technical Association of the Pulp and Paper Industry (TAPPI), TAPPI Online database, 2012
- Washington State University, Northwest Industrial Motor Database Summary, 2008

- IEEE IAS (Industry Application Society), Proceedings of Annual Pulp and Paper Industry Conference, 1960s-2000s

The data sources for the templates are extracted from the real plant data seen inTable A.1 and Table A.2. They are taken from technical publications, industry directory and industry fact books.

Table A.1 Major Kraft-Type Paper Mills at B.C., (Data Source: B.C. Forest Industry Fact Book 1997)

Company name	**Production (10^3 t/year)**	**Capacity in MW (calculated)**
1 Avenor Inc. Gold River	258.8	33.5
2 Canfor Corp. Prince George	622.8	80.6
3 Cariboo Pulp & Paper Co. Ltd. Quesnel	322.6	41.7
4 Celgar Pulp Ltd. Castlegar	414	53.6
5 Crestbrook Forest Ind. Ltd. Skookumchuk	224.3	29.0
6 Crown Packaging Ltd. Burnaby	163.9	21.2
7 Eurocan Pulp & Paper Co. Kitimat	455.4	58.9
8 Fiberco Pulp Inc. Taylor	213.2	27.6
9 Finlay Forest Industries Ltd.. Mackenzie	189.8	24.6
10 Fletcher Challenge Canada Ltd. Crofton	740	95.8
11 Fletcher Challenge Canada Ltd. Duncan Bay	814.2	105.4
12 Fletcher Challenge Canada Ltd. Mackenzie	207	26.8
13 Harmac Pacific Inc. Cedar	386.4	50.0
14 Howe Sound Pulp & Paper Ltd. Port Melon	500.3	64.7
15 Island Paper Mills Company	172.5	22.3

Annacis Island		
16 Louisiana Pacific Corp. Chetwyn	172.5	22.3
17 MacMillian Bloedel Ltd.. Port Alberni	288.1	37.3
18 MacMillan Bloedel Ltd. Powell River	633.1	81.9
19 Newstech Recycling Inc. New Westminister	165.6	21.4
20 Northwood Pulp & Timber Prince George	517.5	67.0
21 Quesnel River Pulp Co. Quesnel	313.9	40.6
22 Scott Paper Ltd. New Westminster	108.7	14.1
23 Skeena Cellulose Prince Rupert	448.5	58.0
24 Western Pulp Ltd. Partnership Port Alice	162.2	21.0
25 Western Pulp Ltd. Partnership Woodfibre	257	33.3
26 Weyerhaeuser Canada Ltd. Kamloops	446.8	57.8

Table A.2 Other Real Cases of Paper Mills

Mill Name	MW
BC Mill_1990*	30.8
Linerboard Mill_1*	55.4
Linerboard Mill_2*	113.7
Fine paper_1*	78.3
Suzano Mill*	88.0
Fray Bentos Mill	122.0
Simpson Tacoma Mill	55.0

Appendix B

Derivation of DC Drive Equivalent Model

The dynamics of DC drives can be generally described by the following six differential or algebraic equations.

1) The average-value model (AVM) for the DC-side circuits:

The AVM model of DC drives is given by,

$$\left(L_d + 2L_C\right)\frac{dI_{dc}}{dt} = V_{dc} - E_g - \left(R_d + \frac{3}{\pi}\omega_e L_C\right)I_{dc} \qquad \text{(B.1)}$$

where, I_{dc} , E_g, V_{dc} are averaged current or voltage, and ω_e is the fundamental frequency.

For convenience of model aggregation, the commutating inductance L_C is neglected in this model. The effects of series impedance (including L_C) will be discussed in our later chapters. Hence, (B.1)can be simplified as,

$$L_d \frac{dI_{dc}}{dt} = V_{dc} - E_g - R_d I_{dc} \qquad \text{(B.2)}$$

2) The mechanical dynamic equation of the motor:

$$J\frac{d\omega_m}{dt} = T_e - T_m \qquad \text{(B.3)}$$

where, the electromagnetic torque T_e is given by $T_e = K_T I_{dc}$, and the mechanical (load) torque T_e is assumed to be constant.

3) The relationship between Back EMF E_g and motor rotating speed ω_m:

$$E_g = K_E \omega_m \tag{B.4}$$

where, K_E is the voltage constant ($K_E = K_T$) and ω_m is the machine speed.

4) The equations for PI current controller (cosine firing angle control mode):

$$\alpha = \arccos\left[-K_{pc} \frac{(I_{dc} - \lambda I_n I_{dc}^*)}{\lambda I_n} - K_{ic} \int_0^t \frac{(I_{dc} - \lambda I_n I_{dc}^*)}{\lambda I_n} dt + \cos\alpha_0 \right] \tag{B.5}$$

where, α is the firing angle of the SCR bridge.

5) The equations for PI speed controller:

$$I_{dc}^* = \left[-K_{ps} \frac{(\omega_m - \omega_m^*)}{\omega_n} - K_{is} \int_0^t \frac{(\omega_m - \omega_m^*)}{\omega_n} dt \right] \tag{B.6}$$

where, ω_n is the nominal speed, λ is the over-loading factor, and I_{dc}^* is the reference current for PI current controller.

6) Output of SCR bridge converter:

The average output voltage of the SCR bridge converter (neglecting commutation inductance L_C) presented by Krause's book [56] is expressed as,

$$V_{dc} = \frac{3\sqrt{6}}{\pi} V_{\lg} \cos\alpha \tag{B.7}$$

Let's assume that there is a small utility-side voltage disturbance ΔV_{lg}. As a result, the linearized small-signal model for the above six equations can be expressed as follows.

$$L_d \frac{d\Delta I_{dc}}{dt} = \Delta V_{dc} - \Delta E_g - R_d \Delta I_{dc} \tag{B.8}$$

$$J \frac{d\Delta \omega_m}{dt} = K_T \Delta I_{dc} \tag{B.9}$$

$$\Delta E_g = K_E \Delta \omega_m \tag{B.10}$$

$$\Delta V_{dc} = \frac{V_{dc0}}{V_{\lg 0}} \Delta V_{\lg} + \frac{3\sqrt{6}}{\pi} V_{\lg 0} \left[-K_{pc} \frac{(\Delta I_{dc} - \lambda I_n \Delta I_{dc}^*)}{\lambda I_n} - K_{ic} \int_0^t \frac{(\Delta I_{dc} - \lambda I_n \Delta I_{dc}^*)}{\lambda I_n} dt \right] \tag{B.11}$$

$$\Delta I_{dc}^* = \left(-K_{ps} \frac{\Delta \omega_m}{\omega_n} - K_{is} \int_0^t \frac{\Delta \omega_m}{\omega_n} dt \right) \tag{B.12}$$

For the reason of convenience, we will use Laplace transform to represent those equations for the following deviation. Substituting (B.9) into (B.12) yields,

$$\Delta I_{dc}^* = \left[-\frac{K_{ps} K_T}{J \omega_n} \frac{1}{s} \Delta I_{dc} - \frac{K_{is} K_T}{J \omega_n} \frac{1}{s^2} \Delta I_{dc} \right] \tag{B.13}$$

Substituting (B.13) into (B.11) yields,

$$\begin{aligned} \Delta V_{dc} = \frac{V_{dc0}}{V_{\lg 0}} \Delta V_{\lg} - \frac{3\sqrt{6}}{\pi} \frac{V_{\lg 0}}{\lambda I_n} \Bigg[K_{pc} + \left(K_{ic} + \frac{\lambda K_T I_n K_{pc} K_{ps}}{J \omega_n} \right) \frac{1}{s} + \ldots \\ \frac{\lambda I_n K_T}{J \omega_n} \left(K_{ic} K_{ps} + K_{pc} K_{is} \right) \frac{1}{s^2} + \frac{\lambda K_T I_n K_{ic} K_{is}}{J \omega_n} \frac{1}{s^3} \Bigg] \Delta I_{dc} \end{aligned} \tag{B.14}$$

Alternatively, (B.14) can also be simplified as,

$$\Delta V_{dc} = \frac{V_{dc0}}{V_{\lg 0}} \Delta V_{\lg} - \left[K_{pc} + K_{eq1} \frac{1}{s} + K_{eq2} \frac{1}{s^2} + K_{eq3} \frac{1}{s^3} \right] R_{eq} \Delta I_{dc} \qquad \text{(B.15)}$$

where,

$$R_{eq} = \frac{3\sqrt{6}}{\pi} \frac{V_{\lg 0}}{\lambda I_n}, \qquad \text{(B.16)}$$

$$K_{eq1} = K_{ic} + \frac{\lambda K_T I_n K_{pc} K_{ps}}{J \omega_n}. \qquad \text{(B.17)}$$

$$K_{eq2} = \frac{\lambda I_n K_T}{J \omega_n} \left(K_{ic} K_{ps} + K_{pc} K_{is} \right) \qquad \text{(B.18)}$$

$$K_{eq3} = \frac{\lambda K_T I_n K_{ic} K_{is}}{J \omega_n} \qquad \text{(B.19)}$$

Substituting (B.10) into (B.9) yields,

$$\Delta E_g = \frac{K_E K_T}{J} \frac{1}{s} \Delta I_{dc} \qquad \text{(B.20)}$$

Substituting (B.15) (B.20) into (B.8) yields,

$$sL_d \Delta I_{dc} + R_d \Delta I_{dc} = \frac{V_{dc0}}{V_{\lg 0}} \Delta V_{\lg} - \left[K_{pc} + K_{eq1} \frac{1}{s} + K_{eq2} \frac{1}{s^2} + K_{eq3} \frac{1}{s^3} \right] R_{eq} \Delta I_{dc} - \frac{K_E K_T}{J} \frac{1}{s} \Delta I_{dc} \qquad \text{(B.21)}$$

Re-organizing (B.21) yields,

$$\frac{\Delta I_{dc}}{\Delta V_{\lg}} = \frac{I_{dc0}}{V_{\lg 0}} \frac{s^3 V_{dc0} / I_{dc0}}{s^4 L_d + s^3 \left(K_{pc} R_{eq} + R_d \right) + s^2 \left(K_{eq1} R_{eq} + \frac{K_E K_T}{J} \right) + s K_{eq2} R_{eq} + K_{eq3} R_{eq}} \qquad \text{(B.22)}$$

Similarly, by substituting (B.22) into (B.15), we can obtain the transfer function of ΔV_{dc} as shown by,

$$\frac{\Delta V_{dc}}{\Delta V_{\lg}} = \frac{V_{dc0}}{V_{\lg 0}} \frac{s^4 L_d + s^3 R_d + s^2 \frac{K_E K_T}{J}}{s^4 L_d + s^3 \left(K_{pc} R_{eq} + R_d \right) + s^2 \left(K_{eq1} R_{eq} + \frac{K_E K_T}{J} \right) + s K_{eq2} R_{eq} + K_{eq3} R_{eq}} \qquad \text{(B.23)}$$

Note that the relationship between DC-side armature current I_{dc} and AC-side phase current I_{ac} (RMS value) can be expressed by,

$$I_{ac}(t) = \sqrt{\frac{2}{3}} I_{dc}(t) \tag{B.24}$$

Therefore, from the utility side, the apparent power *S*, active power *P* and reactive power *Q* consumed by the DC drive can be simply calculated from these DC-side variables,

$$S(t) = 3V_{\lg}(t) I_{ac}(t) = 3V_{\lg}(t) \sqrt{\frac{2}{3}} I_{dc}(t) = \sqrt{6} V_{\lg}(t) I_{dc}(t) \tag{B.25}$$

$$P(t) \approx P_{dc} = V_{dc}(t) I_{dc}(t) \tag{B.26}$$

$$Q(t) = \sqrt{S(t)^2 - P(t)^2} = I_{dc}(t) \sqrt{6V_{\lg}(t)^2 - V_{dc}(t)^2} \tag{B.27}$$

Considering the formula (B.26) from small-signal perspective, one can obtain the following results,

$$\frac{\Delta P}{\Delta V_{\lg}} = \frac{\Delta(V_{dc} I_{dc})}{\Delta V_{\lg}} \approx I_{dc0} \frac{\Delta V_{dc}}{\Delta V_{\lg}} + V_{dc0} \frac{\Delta I_{dc}}{\Delta V_{\lg}} \tag{B.28}$$

Substituting (B.22) (B.23) into (B.28) yields,

$$\frac{\Delta P}{\Delta V_{\lg}} = \frac{P_0}{V_{\lg 0}} \frac{s^4 L_d + s^3 \left(\frac{V_{dc0}}{I_{dc0}} + R_d \right) + s^2 \frac{K_E K_T}{J}}{s^4 L_d + s^3 \left(K_{pc} R_{eq} + R_d \right) + s^2 \left(K_{eq1} R_{eq} + \frac{K_E K_T}{J} \right) + s K_{eq2} R_{eq} + K_{eq3} R_{eq}} \tag{B.29}$$

For the reactive power *Q*, we can expand the equation (B.27) with multi-variable

Taylor series at the initial condition as given by,

$$\Delta Q = Q - Q_0 \approx \frac{\partial Q}{\partial I_{dc}}\Delta I_{dc} + \frac{\partial Q}{\partial V_{dc}}\Delta V_{dc} + \frac{\partial Q}{\partial V_{\lg}}\Delta V_{\lg} + \text{high order terms...} \qquad \text{(B.30)}$$

Since V_{dc} and I_{dc} are small disturbances and can converge to the initial condition (zero), we can neglect the higher-order ($\geq 2^{nd}$ order) terms containing ΔV_{dc} and ΔI_{dc}. But the terms containing only ΔV_{lg} are not negligible, because ΔV_{lg} might be as large as 10%~20% and won't converge to its initial state. Hence, we must keep the higher order term of ΔV_{lg} (up to the third order). Therefore (B.30) can be further expressed as,

$$\frac{\Delta Q}{Q_0} = \left(\frac{\Delta I_{dc}}{I_{dc0}} - \frac{P_0^{\,2}}{Q_0^{\,2}}\frac{\Delta V_{dc}}{V_{dc0}}\right) + \left[\alpha\frac{\Delta V_{\lg}}{V_{\lg 0}} + \beta\left(\frac{\Delta V_{\lg}}{V_{\lg 0}}\right)^2 + \gamma\left(\frac{\Delta V_{\lg}}{V_{\lg 0}}\right)^3\right] \qquad \text{(B.31)}$$

where,

$$\alpha = \frac{S_0^{\,2}}{Q_0^{\,2}}, \quad \beta = -\frac{0.5S_0^{\,2}}{Q_0^{\,2}}\left(\frac{S_0^{\,2}}{Q_0^{\,2}} - 1\right), \text{ and } \gamma = \frac{0.5S_0^{\,4}}{Q_0^{\,4}}\left(\frac{S_0^{\,2}}{Q_0^{\,2}} - 1\right) \qquad \text{(B.32)}$$

Substituting (B.22) (B.23) into (B.31) yields,

$$\frac{\Delta Q}{Q_0} = D(s)\frac{\Delta V_{\lg}}{V_{\lg 0}} + W\left(\Delta V_{\lg}\right) \qquad \text{(B.33)}$$

where,

$$D(s) = -\frac{P_0^{\,2}}{Q_0^{\,2}}\frac{s^4 L_d + s^3\left[R_d - \dfrac{Q_0^{\,2}}{P_0^{\,2}}\dfrac{V_{dc0}}{I_{dc0}}\right] + s^2\dfrac{K_E K_T}{J}}{s^4 L_d + s^3\left(K_{pc}R_{eq} + R_d\right) + s^2\left(K_{eq1}R_{eq} + \dfrac{K_E K_T}{J}\right) + sK_{eq2}R_{eq} + K_{eq3}R_{eq}} \qquad \text{(B.34)}$$

$$W\left(\Delta V_{\mathrm{lg}}\right)=\alpha\frac{\Delta V_{\mathrm{lg}}}{V_{\mathrm{lg}0}}+\beta\frac{\Delta V_{\mathrm{lg}}{}^{2}}{V_{\mathrm{lg}0}{}^{2}}+\gamma\frac{\Delta V_{\mathrm{lg}}{}^{3}}{V_{\mathrm{lg}0}{}^{3}} \tag{B.35}$$

$$\alpha=\frac{S_0{}^{2}}{Q_0{}^{2}},\quad \beta=\frac{0.5S_0{}^{2}}{Q_0{}^{2}}\left(1-\frac{S_0{}^{2}}{Q_0{}^{2}}\right),\quad \gamma=\frac{0.5S_0{}^{4}}{Q_0{}^{4}}\left(\frac{S_0{}^{2}}{Q_0{}^{2}}-1\right) \tag{B.36}$$

As seen in (B.33), the response of reactive power can be regarded as two parts: dynamic part D(s) and static part $W(\Delta V_{lg})$.

In summary, the proposed model can be expressed by the function of the active power P and reactive power Q with regard to the bus voltage V. The final form of the proposed model is shown as,

$$\frac{P}{P_0}=1+H(\mathrm{s})\frac{V-V_0}{V_0} \tag{B.37}$$

$$\frac{Q}{Q_0}=\left[1+\alpha\frac{V-V_0}{V_0}+\beta\left(\frac{V-V_0}{V_0}\right)^{2}+\gamma\left(\frac{V-V_0}{V_0}\right)^{3}\right]+D(\mathrm{s})\frac{V-V_0}{V_0} \tag{B.38}$$

where,

$$\alpha=\frac{S_0{}^{2}}{Q_0{}^{2}},\quad \beta=-0.5\frac{S_0{}^{2}}{Q_0{}^{2}}\frac{P_0{}^{2}}{Q_0{}^{2}},\ \text{and}\ \ \gamma=0.5\frac{S_0{}^{4}}{Q_0{}^{4}}\frac{P_0{}^{2}}{Q_0{}^{2}} \tag{B.39}$$

$$H(\mathrm{s})=\frac{s^4L_d+s^3\left(\frac{V_{dc0}}{I_{dc0}}+R_d\right)+s^2\frac{K_EK_T}{J}}{s^4L_d+s^3\left(K_{pc}R_{eq}+R_d\right)+s^2\left(K_{eq1}R_{eq}+\frac{K_EK_T}{J}\right)+sK_{eq2}R_{eq}+K_{eq3}R_{eq}} \tag{B.40}$$

$$D(s)=-\frac{P_0{}^{2}}{Q_0{}^{2}}\frac{s^4L_d+s^3\left[R_d-\frac{Q_0{}^{2}}{P_0{}^{2}}\frac{V_{dc0}}{I_{dc0}}\right]+s^2\frac{K_EK_T}{J}}{s^4L_d+s^3\left(K_{pc}R_{eq}+R_d\right)+s^2\left(K_{eq1}R_{eq}+\frac{K_EK_T}{J}\right)+sK_{eq2}R_{eq}+K_{eq3}R_{eq}} \tag{B.41}$$

Hence, the proposed model is represented with the fourth-order transfer function

as shown in (B.29) and (B.33).

In order to unify the form of active and reactive power response, the final form of the equivalent model is given by:

$$\frac{P}{P_0}=1+\left[\alpha_p\frac{V-V_0}{V_0}+\beta_p\left(\frac{V-V_0}{V_0}\right)^2+\gamma_p\left(\frac{V-V_0}{V_0}\right)^3\right]+H(\mathrm{s})\frac{V-V_0}{V_0} \quad \text{(B.42)}$$

$$\frac{Q}{Q_0}=1+\left[\alpha_q\frac{V-V_0}{V_0}+\beta_q\left(\frac{V-V_0}{V_0}\right)^2+\gamma_q\left(\frac{V-V_0}{V_0}\right)^3\right]+D(\mathrm{s})\frac{V-V_0}{V_0} \quad \text{(B.43)}$$

where,

$$\alpha_p=0,\ \beta_p=0,\ \text{and}\ \gamma_p=0 \quad \text{(B.44)}$$

$$\alpha_q=\frac{S_0^{\,2}}{Q_0^{\,2}},\quad \beta_q=-0.5\frac{S_0^{\,2}}{Q_0^{\,2}}\frac{P_0^{\,2}}{Q_0^{\,2}},\ \text{and}\ \gamma_q=0.5\frac{S_0^{\,4}}{Q_0^{\,4}}\frac{P_0^{\,2}}{Q_0^{\,2}} \quad \text{(B.45)}$$

$$H(\mathrm{s})=\frac{s^4L_d+s^3\left(R_d+V_{dc0}/I_{dc0}\right)+s^2K_E^{\,2}J^{-1}}{s^4L_d+s^3\left(K_{pc}R_{eq}+R_d\right)+s^2\left(K_{eq1}R_{eq}+K_E^{\,2}J^{-1}\right)+sK_{eq2}R_{eq}+K_{eq3}R_{eq}} \quad \text{(B.46)}$$

$$D(s)=-\frac{P_0^{\,2}}{Q_0^{\,2}}\frac{s^4L_d+s^3\left[R_d-Q_0^{\,2}V_{dc0}/P_0^{\,2}I_{dc0}\right]+}{s^4L_d+s^3\left(K_{pc}R_{eq}+R_d\right)+}\rightarrow$$

$$\leftarrow\frac{+s^2K_E^{\,2}J^{-1}}{+s^2\left(K_{eq1}R_{eq}+K_E^{\,2}J^{-1}\right)+sK_{eq2}R_{eq}+K_{eq3}R_{eq}} \quad \text{(B.47)}$$

$$R_{eq}=\frac{3\sqrt{6}}{\pi}\frac{V_{\mathrm{lg}0}}{\lambda I_n},\quad K_{eq1}=K_{ic}+\frac{\lambda K_E I_n K_{pc}K_{ps}}{J\omega_n} \quad \text{(B.48)}$$

$$K_{eq2}=\frac{\lambda I_n K_E}{J\omega_n}\left(K_{ic}K_{ps}+K_{pc}K_{is}\right),\quad K_{eq3}=\frac{\lambda K_E I_n K_{ic}K_{is}}{J\omega_n} \quad \text{(B.49)}$$

Appendix C

Pade-Approximation-Based Order Reduction Technique

Pade approximation is a method to equalize the n^{th}-order Maclaurin expansion of an original function and an approximated rational function. This technique has been well developed in [61] and has been applied to model order reduction of load models in [67]. This section will present a technique to reduce the order of transfer function model using Pade approximation. In particular, this appendix will present how to approximate a high-order model with a fourth-order model.

Suppose that an original transfer function (standard form) is given by,

$$H(s)=\frac{w_{n-1}s^{n-1}+w_{n-2}s^{n-2}+\cdots+w_1 s+w_0}{v_n s^n+v_{n-1}s^{n-1}+\cdots+v_1 s+v_0}\left(n>4\right) \qquad \text{(C.1)}$$

According to [61], $H(s)$ can be approximated by a Taylor series about s=0 as shown by (4.26). Note that we only keep up to 8th order terms here.

$$H(s)\approx f(\mathrm{s})=a_0+a_1 s+a_2 s^2+\ldots+a_8 s^2 \qquad \text{(C.2)}$$

where, a_{ki} are Taylor expansion coefficients as given below.

$$a_0=\frac{w_0}{v_0},\quad \text{and}\quad a_k=\frac{1}{v_0}\left[w_k-\sum_{h=1}^{k}v_h a_{(k-h)}\right]\quad (k=1,\ 2,\ \ldots\ ,8\ ) \qquad \text{(C.3)}$$

According to Pade approximation technique, any given function $f(s)$ can be

approximated by a fourth order rational function $R(s)$ of the form (q_0=1),

$$R(s) = \frac{p_4 s^4 + p_3 s^3 + p_2 s^2 + p_1 s + p_0}{q_4 s^4 + q_3 s^3 + q_2 s^2 + q_1 s + q_0} \tag{C.4}$$

Assuming $f(s) = R(s)$, we can obtain,

$$f(s) - R(s) = \frac{\sum_{j=0}^{4} q_j s \sum_{k=0}^{8} a_k s_k - \sum_{i=o}^{4} p_1 s}{\sum_{j=0}^{4} q_j s} \tag{C.5}$$

Hence, the coefficients of x^h in the numerator must be zero, as given by,

$$\sum_{i=0}^{h} a_i q_{h-i} - p_h = 0, \quad h=0, 1, \ldots 8 \tag{C.6}$$

We assume that,

$$p_h = 0, \text{ and } q_h = 0 \quad (h > 8) \tag{C.7}$$

Combining (C.6) and (C.7) yields,

$$\begin{bmatrix} a_0 & 0 & 0 & 0 & -1 & 0 & 0 & 0 \\ a_1 & a_0 & 0 & 0 & 0 & -1 & 0 & 0 \\ a_2 & a_1 & a_0 & 0 & 0 & 0 & -1 & 0 \\ a_3 & a_2 & a_1 & a_0 & 0 & 0 & 0 & -1 \\ a_4 & a_3 & a_2 & a_1 & 0 & 0 & 0 & 0 \\ a_5 & a_4 & a_3 & a_2 & 0 & 0 & 0 & 0 \\ a_6 & a_5 & a_4 & a_3 & 0 & 0 & 0 & 0 \\ a_7 & a_6 & a_5 & a_4 & 0 & 0 & 0 & 0 \end{bmatrix} \begin{bmatrix} q_1 \\ q_2 \\ q_3 \\ q_4 \\ p_1 \\ p_2 \\ p_3 \\ p_4 \end{bmatrix} = \begin{bmatrix} a_1 \\ a_2 \\ a_3 \\ a_4 \\ a_5 \\ a_6 \\ a_7 \\ a_8 \end{bmatrix} \tag{C.8}$$

Solving the linear equations (C.8) can yield the solutions (p_1, p_2, p_3, p_4 and q_1, q_2, q_3, q_4).

Ultimately, the original transfer function $H(s)$ can be approximated with the newly-obtained fourth-order transfer function $R(s)$, as shown by,

$$H(s) \approx R(s) = \frac{p_4 s^4 + p_3 s^3 + p_2 s^2 + p_1 s + p_0}{q_4 s^4 + q_3 s^3 + q_2 s^2 + q_1 s + q_0} \tag{C.9}$$

Sometimes the original transfer function $H(s)$ might have the n^{th} order term in the numerator as given by,

$$H(s) = \frac{w_n s^n + w_{n-1} s^{n-1} + \cdots + w_1 s + w_0}{v_n s^n + v_{n-1} s^{n-1} + \cdots + v_1 s + v_0} \tag{C.10}$$

We can convert it into the standard form as $H'(s)$ shown by,

$$H'(s) = H(s) - \frac{w_n}{v_n} = \frac{w'_{n-1} s^{n-1} + w'_{n-2} s^{n-2} + \cdots + w'_1 s + w'_0}{v_n s^n + v_{n-1} s^{n-1} + \cdots + v_1 s + v_0} \tag{C.11}$$

Appendix D

Simulation Specifications of DC Drives

Appendix D presents the simulation parameters of DC drives and other components (i.e. cables and transformers) that we used for simulation studies in section 4.3.

Case 1:

The schematic diagram for case 1 is given in Figure D.1. The Simulink block diagram is as shown in Figure D.2 (original model) and Figure D.3 (aggregated model). Each of DC drives is represented with the dynamic load model as characterized by the proposed transfer function model. The specifications of DC drives (DD1~DD4) are shown in Table D.1, Table D.2, Table D.3, and Table D.4. Note that the parameters we used for simulation of DD1 and DD2 is taken from N. Hong [58]; the parameters we used for simulation of DD3 and DD4 is taken from S. Zhang [57].

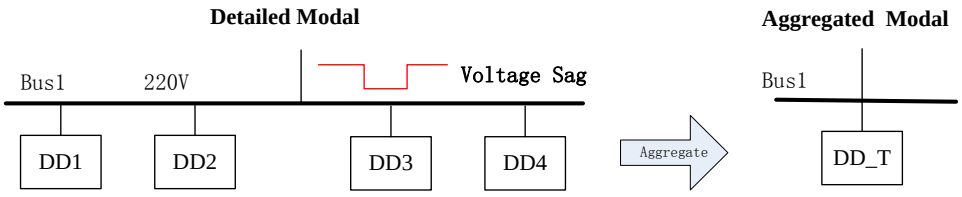

Figure D.1 Schematic diagram for Case 1

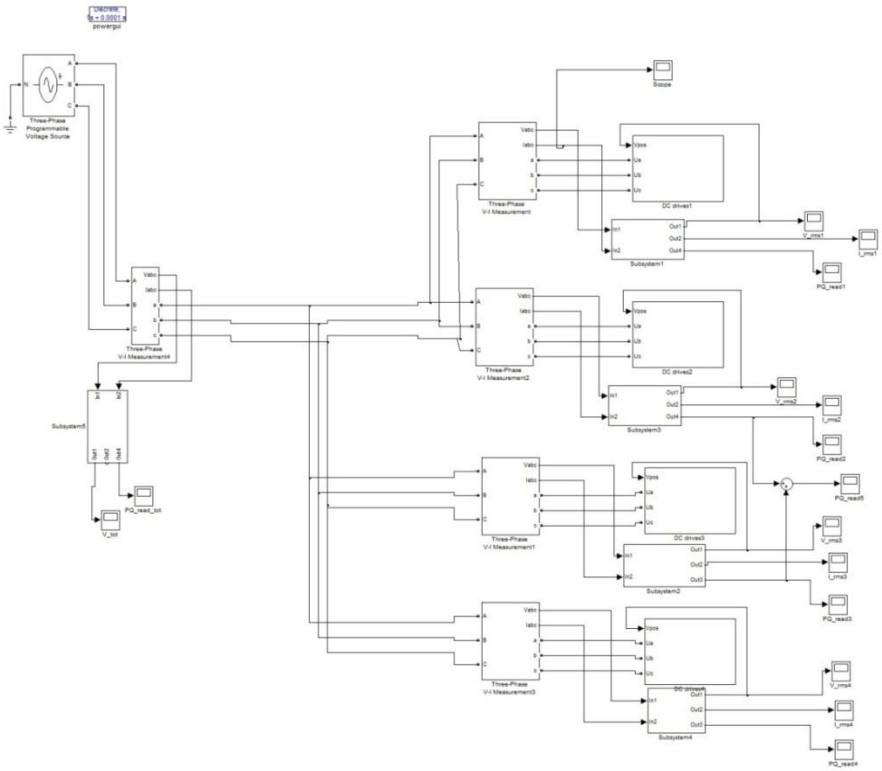

Figure D.2 Simulink block diagram to simulate Case 1 (original models)

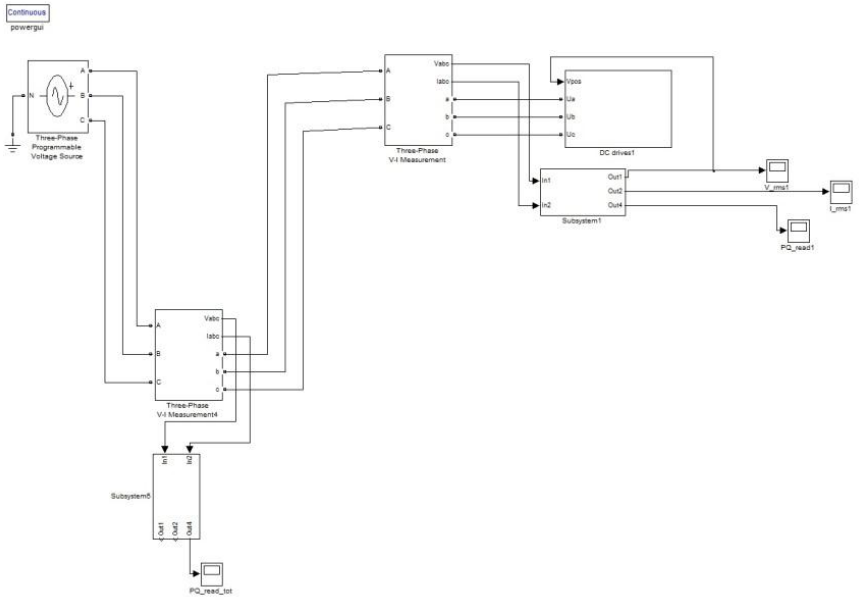

Figure C3 Simulink block diagram to simulate Case 1 (Aggregated model)

Table D.1 Specification of DC Drive#1

Rated Power (HP)	40	Commutation Inductance L_c(H)	0

Nominal Voltage (V)	220	Armature Resistance R_d (Ω)	0.21
Nominal Current (A)	136	Smoothing Inductance L_d (mH)	20
Nominal Speed (rpm)	1500	Mutual Inductance L_{df} (H)	2.621
Motor Inertia (kg·m^2)	0.57	Field Current I_f (A)	1.5
Controller parameter	PI Speed controller: K_p=10.5, K_i=120.5 PI Current controller: K_p=2.48, K_i=37.3 Overload factor λ=1.5		
Mechanical Load	T_L=239.36$N{\cdot}m$		
Base Case Status	40.3kW+j25.6$kVar$, Supply voltage: 208V(L-L)		

Table D.2 Specification of DC Drive#2

Rated Power (HP)	40	Commutation Inductance L_c(H)	0
Nominal Voltage (V)	220	Armature Resistance R_d (Ω)	0.21
Nominal Current (A)	136	Smoothing Inductance L_d (mH)	20
Nominal Speed (rpm)	1500	Mutual Inductance L_{df} (H)	2.621
Motor Inertia (kg·m^2)	0.57	Field Current I_f (A)	1.5
Controller parameter	PI Speed controller: K_p=10.5, K_i=120.5 PI Current controller: K_p=2.48, K_i=37.3 Overload factor λ=1.5		
Mechanical Load	T_L=171.5$N{\cdot}m$		
Base Case Status	25.8kW+j28.2$kVar$, Supply voltage: 208V(L-L)		

Table D.3 Specification of DC Drive#3 (To be updated)

Rated Power (HP)	120	Commutation Inductance L_c(H)	0
Nominal Voltage (V)	220	Armature Resistance R_d (Ω)	0.02
Nominal Current (A)	462	Smoothing Inductance L_d (mH)	5
Nominal Speed (rpm)	560	Mutual Inductance L_{df} (H)	1.79
Motor Inertia (kg·m^2)	14.7	Field Current I_f (A)	2.0
Controller parameter	PI Speed controller: K_p=118.4, K_i=1369 PI Current controller: K_p=1.36, K_i=0.072 Overload factor λ=1.5		
Mechanical Load	T_L=705.5$N{\cdot}m$		
Base Case Status	42.2kW+j35.8$kVar$, Supply voltage: 208V(L-L)		

Table D.4 Specification of DC Drive#4 (To be updated)

Rated Power (HP)	120	Commutation Inductance L_c(H)	0
Nominal Voltage (V)	220	Armature Resistance R_d (Ω)	0.02
Nominal Current (A)	462	Smoothing Inductance L_d (mH)	5
Nominal Speed (rpm)	560	Mutual Inductance L_{df} (H)	1.79

Motor Inertia (kg·m^2)	14.7	Field Current I_f (A)	2.0
Controller parameter	PI Speed controller: K_p=118.4, K_i=1369 PI Current controller: K_p=1.36, K_i=0.072		
Mechanical Load	T_L=705.5$N{\cdot}m$		
Base Case Status	33.9kW+j43.8$kVar$, Supply voltage: 208V(L-L)		

Case 2:

The schematic diagram for case 2 is given in Figure D.4.

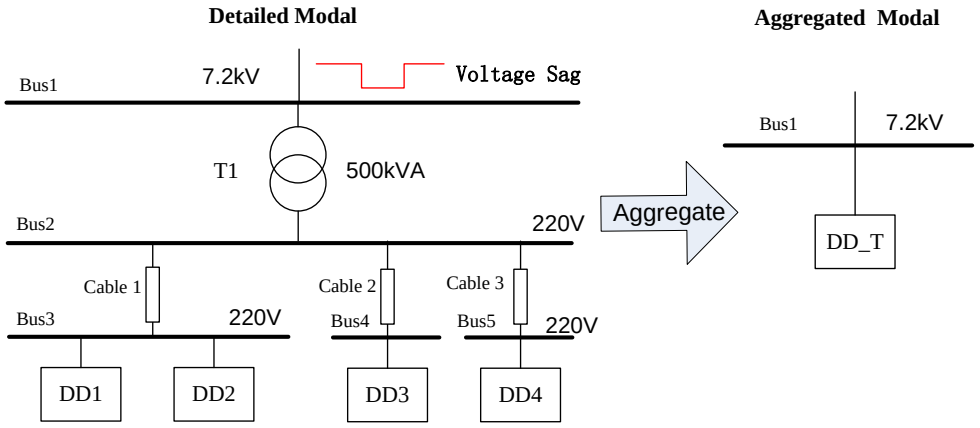

Figure D.4 Schematic diagram for Case 2

The Simulink block diagram is as shown in Figure D.5 (original model) and Figure D.6 (aggregated model). Each of DC drives is represented with the dynamic load model as characterized by the proposed transfer function model as shown in Figure 4.4. In case 2, the specifications of DC drives (DD1~DD4) are the same as Case 1. The specifications for transformers and cables in Case 2 are given below as shown in Table D.2.

Table D.2 Specification of Cables and Transformers

Equipment	Specifications
T1	500kVA, 7200V/220V, R(p.u.)=1.6% , X(p.u.)=6%
Cable 1	Z_L=0.03+0.01 *j* (Ohms), Length=100m
Cable 2	Z_L=0.015+0.005 *j* (Ohms), Length=50m
Cable 3	Z_L=0.015+0.005 *j* (Ohms), Length=50m

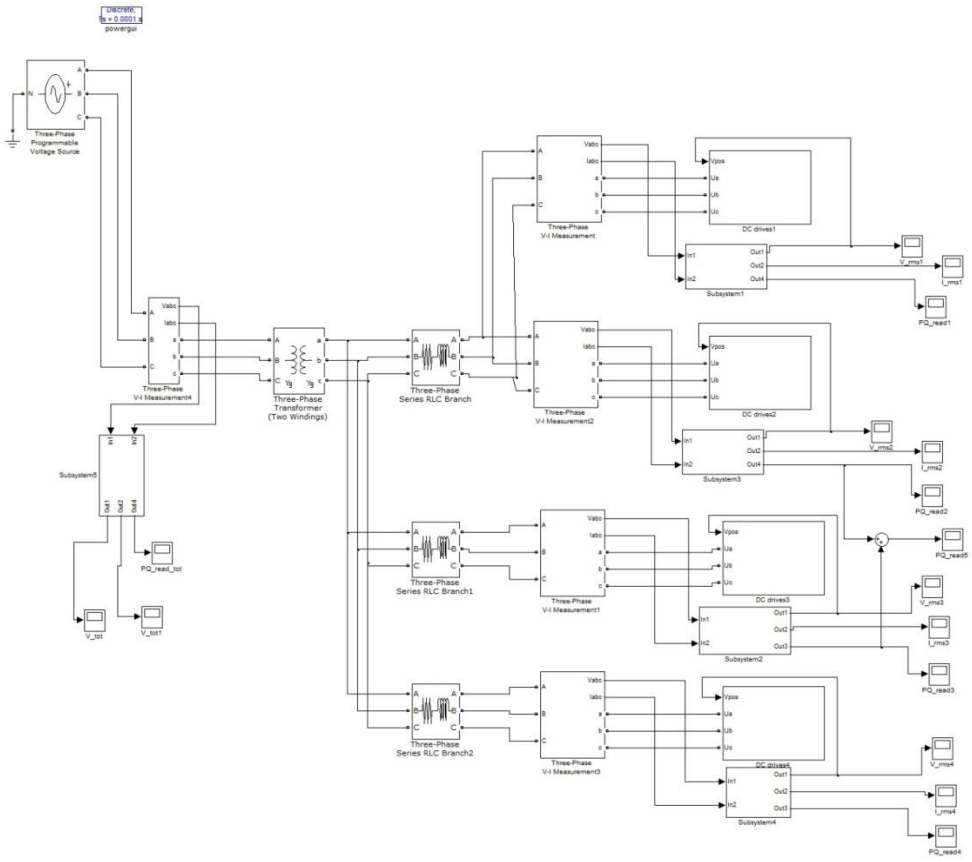

Figure D.5 Simulink block diagram to simulate Case 2

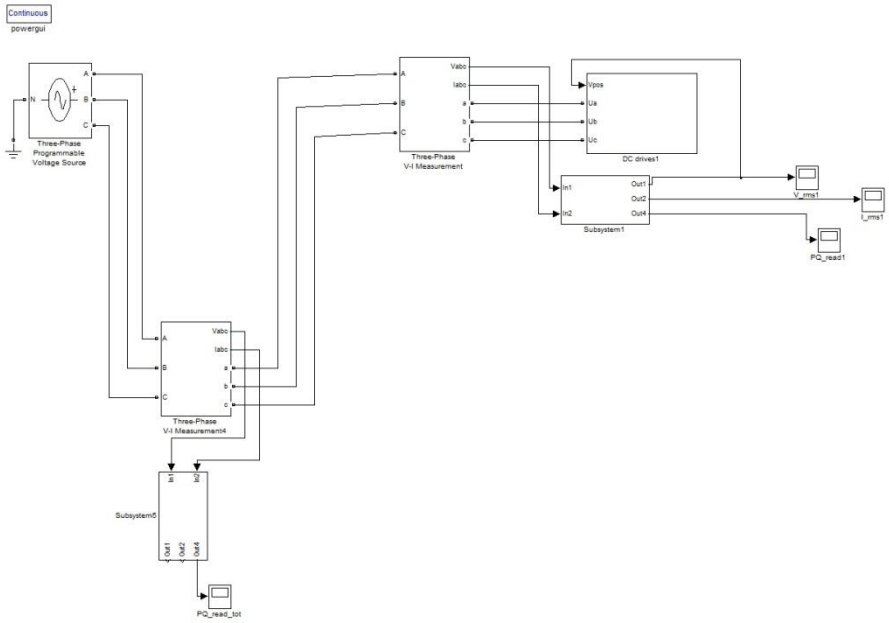

Figure D.6 Simulink block diagram to simulate Case 2 (Aggregated model)

Appendix E

Matlab Program for Generating the Equivalent Model for DC Drives

This Appendix presents a Matlab program ("*.m" files) to convert the input data of DC drives into an equivalent model.

How to represent the equivalent model of DC drives in this program

In this program, the equivalent dynamic model is implemented in the form of a structure variable "DD" (DC Drive). The parameters of the equivalent dynamic model are represented as the fields of DD structures (Table E.1).

Table E.1 Definition of the fields of DD (DC Drives) structure variables

Field	Explanation	Sample data
.PB	Real power at base case (P_0, in kW).	107.0
.QB	Reactive power at base case (Q_0, in kVar).	87.4
.Vt	Utility bus voltage at base case, phase-to-ground (V_{lg0}, in V).	120.9
.Vb	Nominal utility bus voltage, phase-to-ground (V_b, in V).	120
.A123_agg	Polynomial coefficients (P): $[\alpha_p, \beta_p, \gamma_p]$.	[2.3847, -1.6510, 3.9370]
.W123_agg	Polynomial coefficients (Q): $[\alpha_q, \beta_q, \gamma_q]$.	[0, 0, 0]
.P_H	Transfer function $H(s)$ for real power. (Please use	$\frac{0.0063s^4 + 1.123s^3 + 0.8743s^2}{0.0063s^4 + 0.575s^3 + 198s^2 + 4819s + 30410}$

	command “help tf” for more details on constructing a transfer function.)	
.Q_H	Transfer function *D*(s) for reactive power. (Please use command “help tf” for more details on constructing a transfer function.)	$\frac{-0.008723s^4+1.075s^3-1.211s^2}{0.0063s^4+0.575s^3+198s^2+4819s+30410}$

Description of Matlab Function

This program consists of one Matlab function “Build_DD”, the purpose of which is to build the equivalent model from the input data (Table 3.2). The input of the function is an array of numbers “Input_para”. Two formats of the input array “Input_para” are supported as shown below. Note that format 2 (minimal user input) only requires the basic information of the drive, and assumes that all other parameters are taken from sample data or typical data.

Format 1 (standard user input):

V_{lg0}	P_0	Q_0	P_n	I_n	ω_n	R_d	L_d	K_{pc}	K_{ic}	K_{ps}	K_{is}	λ	K_E	J

Format 2 (minimal user input):

V_{lg0}	P_0	Q_0	P_n	I_n	ω_n

Parameters:

V_{lg0} : Utility bus voltage (base case), phase-to-ground, in kV

P_0 : *R*eal and reactive power consumption of the drive (base case), in kW

Q_0 : *R*eal and reactive power consumption of the drive (base case), in kW

P_n : Rated Motor Power, in HP

I_n : Nominal DC-motor armature current, inA

ω_n : Nominal motor speed, in rpm

R_d : DC armature circuit resistance (total), in Ohms

L_d : DC armature circuit inductance (total), in Henry

K_{pc} : Proportional constant of PI current controller

K_{ic} : Integral constant of PI current controller

K_{ps} : Proportional constant of PI speed controller

K_{is} : Integral constant of PI speed controller

λ : Over-loading factor

K_E : Voltage constant of the DC motor

J : Moment of inertia of the DC motor

The output is a DD structure named "DD_output", representing the equivalent model. Note that the calculation of equivalent models requires the initial conditions of DC drives, including initial utility bus voltage (V_{lg0}), initial real power (P_0), and initial reactive power (Q_0). The initial conditions can be either preset values, or obtained from the load flow results of the actual network.

How to use

Step 1: Preset the initial conditions (V_{lg0}, P_0, Q_0) of the DC drives, or determine the initial conditions from the load flow studies of a network.

Step 2: Prepare the input data as specified in standard format (format 1) or minimal user input (format 2).

Step 3: Enter the input, and run the Matlab function "Build_DD".

Step 4: Save the output "DD_output" for dynamic simulation, or for model aggregation program.

Matlab Codes

```
function [DD_output] = Build_DD(Input_para)
% BUILD_DD: Build a DC drive equivlaent model (Strcture)
% Input format 1:[Vlg0 PB QB Pn In wn Rd Ld Kpc Kic Kps Kis lambda KE
J]
% Input format 2:[Vlg0 PB QB Pn In wn]

input_error=0;

if length(Input_para)==15,
    Vlg0=Input_para(1);
    PB=Input_para(2);
    QB=Input_para(3);
    Pn=Input_para(4);
    In=Input_para(5);
    wn=Input_para(6);% wn in rpm
    Rd=Input_para(7);
    Ld=Input_para(8);
    Kpc=Input_para(9);
    Kic=Input_para(10);
    Kps=Input_para(11);
    Kis=Input_para(12);
    lambda=Input_para(13);
    KE=Input_para(14);
    J=Input_para(15);
elseif length(Input_para)==6,
    Vlg0=Input_para(1);
    PB=Input_para(2);
    QB=Input_para(3);
    Pn=Input_para(4);
    In=Input_para(5);
    wn=Input_para(6);% wn in rpm
```

```
    Rd=max(1.5147*exp(-0.027*Pn),0.1);
    Ld=13.8*Vlg0/In*1/1000;%in Henry
    Kpc=2.48;
    Kic=37.3;
    Kps=10.5;
    Kis=120.5;
    lambda=1.5;
    KE=(Pn/1.341*1e3)/In/wn;
    Hsec=0.5;
    J=6.79e4*Hsec*Pn/wn^2;
else
    display('Error! The length of Input array must be 6 or 15. ');
    input_error=1;
end;

if input_error==1,
    DD_output=-1;
else
    wn=wn/9.55;% convert rpm to rad/s
    KT=KE;
    beta=atan(QB/PB);
    Vdc_base=2.34*Vlg0*cos(beta);
    Idc_base=PB*1000/Vdc_base;
    K1=Kic+Kpc*Kps*KT*lambda*In/J/wn;
    K2=(Kic*Kps+Kpc*Kis)*KT*lambda*In/J/wn;
    K3=Kic*Kis*KT*lambda*In/J/wn;
    Req=3*sqrt(6)/pi*Vlg0/In/lambda;
    Rdc=Vdc_base/Idc_base;
    xi=(PB/QB)^2;
    SB=sqrt(PB^2+QB^2);
    A1=(SB/QB)^2;
    A2=-0.5*(SB/QB)^2*(PB/QB)^2;
    A3=0.5*(SB/QB)^4*(PB/QB)^2;

    DD_output.PB=PB;
    DD_output.QB=QB;
    DD_output.Vb=Vlg0;
    DD_output.Vt=Vlg0;
    DD_output.A123_agg=[A1 A2 A3];
    DD_output.W123_agg=[0 0 0];
```

```
    num_px=[Ld Rdc+Rd KE*KT/J 0 0];% P-V relation
    den_px=[Ld Kpc*Req+Rd K1*Req+KE*KT/J K2*Req K3*Req];
    num_qx=[Ld Rd-(1/xi)*Rdc KE*KT/J 0 0]*(-xi);%%% Q-V relastion
    den_qx=[Ld Kpc*Req+Rd K1*Req+KE*KT/J K2*Req K3*Req];
    DD_output.P_H=tf(num_px,den_px);
    DD_output.Q_H=tf(num_qx,den_qx);
end;
```

Appendix F

Matlab Program for Aggregating the Equivalent Models

In the main body, two equivalence techniques are established for aggregating DC drives:

(1) Technique for aggregating DC drives connected at the same bus.

(2) Technique for incorporating the effects of series impedance (i.e. cables and transformers) into the DC drive model.

This Appendix presents a package of Matlab functions ("*.m" files) to implement these two techniques. Using these techniques as elementary modules, users may build a systematic equivalence using the concept of bottom-up approaches. The bottom-up approach allows the user to apply equivalence techniques from the bottom level up to the top level until a single-unit model is obtained. Using such a method, users can develop their own case-specific aggregation program.

This Appendix documents the brief requirement and procedures of using this Matlab program. Note that this Appendix is a follow-up section of Appendix E, and requires the results from Appendix E. So please read Appendix E prior to Appendix F.

Description of Matlab Functions

This Matlab program package includes two functions.

The first Matlab function is “agg_DD.m”, the purpose of which is to aggregate the DC drives connected at the same bus. The required input of the function is an array of DD structures (DD_GROUP) connected at the same bus. The output of the function is a new DD structure (DD_agg), representing the aggregated model.

The second Matlab function is “agg_Z.m”, the purpose of which is to incorporate the effects of series impedance into the existing DC drive model. The required input of the function includes a DD structure (DD), resistance of the impedance (RL), reactance of the impedance (XL). The output of the function is a DD structure (DD_agg), representing the DC drive model with the effects of series impedance considered.

How to Use

Step 1: Prepare the equivalent models (in form of “DD” structures) for all the DC drives that need to be aggregated. The Matlab program for generating such models is presented in Appendix E. the equivalent models are readily to be used by the model aggregation program.

Step 2: Prepare the impedance models (R_L+jX_L) for all the cables and

transformers.

Step 3: Write a case-specific program for generating systematic equivalence. The given Matlab functions ("agg_DD.m" and "agg_Z.m") can be used as elementary modules. A basic methodology is to represent the structure of the distribution system as a multi-branch "tree". By starting from the tips of the tree, one can apply the equivalence techniques from the bottom level up to the top until the single-unit equivalence is obtained.

Step 4: Run the model aggregation program, and output the systematic equivalence (a single-unit DC drive model).

Step 5: Implement the output model as User-Defined Model (UDM) in the dynamic performance simulation of large-scale system studies.

Matlab Codes

~~~~~~~~~~ Begin of file 1: "agg_DD .m " ~~~~~~~~~~~~~~~

```
function [ DD_agg ] = agg_DD(DD_GROUP)
% agg_DD: to aggregate the DC drives connected at the same bus
% DD_GROUP is an array of DD (Struct of DC drives to be aggregated)
% Please name the ".m" file as "agg_DD .m "

Ndd=length(DD_GROUP); % Number of DC Drives
A123=[0 0 0];
W123=[0 0 0];
Px_sys=0;Ptot=0;
Qx_sys=0;Qtot=0;

for hh=1:Ndd,
    DD=DD_GROUP(hh);
    A123=A123+DD.QB*DD.A123_agg; % Polynomial coefficients of Real
```
~~~~~~~~~~

```
Power
    W123=W123+DD.PB*DD.W123_agg; % Polynomial coefficients of
Reactive Power
    Px_sys=Px_sys+DD.PB*DD.P_H;% Sum of dynamic parts H(s)
    Qx_sys=Qx_sys+DD.QB*DD.Q_H;% Sum of dynamic parts D(s)
    Ptot=Ptot+DD.PB; % Sum of real power at base case
    Qtot=Qtot+DD.QB;  % Sum of reactive power at base case
end;

DD_agg.Vt= DD_GROUP(1).Vt; % Terminal voltage of aggregated model
DD_agg.Vb= DD_GROUP(1).Vb; % Base voltage of aggregated model
DD_agg.PB=Ptot;
DD_agg.QB=Qtot;
A123_agg=A123/Ptot;
W123_agg=W123/Qtot;
DD_agg.A123_agg=A123_agg; % Polynomial coefficients of aggregated
model
DD_agg.W123_agg=W123_agg; % Polynomial coefficients of aggregated
model

Px_sys=Px_sys/Ptot;  % Dynamic parts H(s)-before order reduction
Qx_sys=Qx_sys/Qtot;  % Dynamic parts D(s)-before order reduction
Px_sys4=pademod(Px_sys,3,4); % Model order reduction-Pade
approximation
Qx_sys4=pademod(Qx_sys,3,4);
DD_agg.P_H=Px_sys4; % Dynamic parts H(s)- after order reduction
DD_agg.Q_H=Qx_sys4; % Dynamic parts D(s)- after order reduction

function G_r=pademod(G_Sys,r,k) % sub-function
KK1=G_Sys{1}(1)/G_Sys.den{1}(1)
G_Sys=G_Sys-KK1;% convert to standard TF form: num (r),den (k)
c=timmomt(G_Sys,r+k+1);
G_r=pade_app(c,r,k);
G_r=G_r+KK1;% convert to original TF form

function M=timmomt(G,k) % sub-function
%????G??k?????
G=ss(G);C=G.c;B=G.b;iA=inv(G.a);iA1=iA;M=zeros(1,k);
for i=1:k,M(i)=-C*iA1*B;iA1=iA*iA1;end

function Gr=pade_app(c,r,k) % sub-function
```

```
w=-c(r+2:r+k+1)';
vv=[c(r+1:-1:1)';zeros(k-1-r,1)];
W=rot90(hankel(c(r+k:-1:r+1),vv));
V=rot90(hankel(c(r:-1:1)));
x=[1 (W\w)'];
dred=x(k+1:-1:1)/x(k+1);
y=[c(1) x(2:r+1)*V'+c(2:r+1)];
nred=y(r+1:-1:1)/x(k+1);
Gr=tf(nred,dred);
```

========== End of file 1: "agg_DD .m " ==========

~~~~~~~~~~Begin of file 2: "agg_Z.m " ~~~~~~~~~~~~

```
function [ DD_y ] = agg_Z( DD,RL,XL)
%AGGZ_DD: to incorporate the effects of series impedance into the DC
drive model
%DD: the equivalent DC drive model
%RL: resistance of the impedance, XL: reactance of the impedance

PB=1000*DD.PB;
QB=1000*DD.QB;
VB=DD.Vb;

PA=PB+(PB^2+QB^2)*RL/3/VB^2;
QA=QB+(PB^2+QB^2)*XL/3/VB^2;
VA=VB+(PB*RL+QB*XL)/3/VB;
SB=sqrt(PB^2+QB^2);

epslong=1/(1+(DD.W1-1)*PB*RL/3/VB^2+(DD.A1-1)*QB*RL/3/VB^2);

CC1=epslong*VA/PA*(PB/VB+2*RL*PB^2/3/VB^3);
CC2=epslong*VA/PA*(0+2*RL*QB^2/3/VB^3);
CC3=epslong*VA/QA*(0+2*XL*PB^2/3/VB^3);
CC4=epslong*VA/QA*(QB/VB+2*XL*QB^2/3/VB^3);

DD_y.PB=PA/1000;
DD_y.QB=QA/1000;

W1_tmp=epslong*VA/VB*(PB/PA*DD.W1-0*2*RL*SB^2/3/VB^2/PA);
W2_tmp=(epslong*VA/VB)^2*PB/PA*DD.W2;
```
~~~~~~~~~~

```
W3_tmp=(epslong*VA/VB)^3*PB/PA*DD.W3;

DD_y.A1_tmp =epslong*VA/VB*(QB/QA*DD.A1-0*2*XL*SB^2/3/VB^2/QA);
DD_y.A2_tmp =(epslong*VA/VB)^2*QB/QA*DD.A2;
DD_y.A3_tmp =(epslong*VA/VB)^3*QB/QA*DD.A3;

DD_y.A123_agg=[A1_tmp A2_tmp A3_tmp];
DD_y.W123_agg=[W1_tmp W2_tmp W3_tmp];

DD_y.Vt=DD.Vt+(PB*RL+QB*XL)/3/DD.Vt;
DD_y.Vb=VA;
DD_y.P_H=DD.P_H*CC1+DD.Q_H*CC2;
DD_y.Q_H=DD.P_H*CC3+DD.Q_H*CC4;

DD_y.P_H= pademod(DD_y.P_H,3,4);
DD_y.Q_H= pademod(DD_y.Q_H,3,4);

function G_r=pademod(G_Sys,r,k) % sub-function
KK1=G_Sys{1}(1)/G_Sys.den{1}(1)
G_Sys=G_Sys-KK1;% convert to standard TF form: num (r),den (k)
c=timmomt(G_Sys,r+k+1);
G_r=pade_app(c,r,k);
G_r=G_r+KK1;% convert to original TF form

function M=timmomt(G,k) % sub-function
%????G??k?????
G=ss(G);C=G.c;B=G.b;iA=inv(G.a);iA1=iA;M=zeros(1,k);
for i=1:k,M(i)=-C*iA1*B;iA1=iA*iA1;end

function Gr=pade_app(c,r,k) % sub-function
w=-c(r+2:r+k+1)';
vv=[c(r+1:-1:1)';zeros(k-1-r,1)];
W=rot90(hankel(c(r+k:-1:r+1),vv));
V=rot90(hankel(c(r:-1:1)));
x=[1 (W\w)'];
dred=x(k+1:-1:1)/x(k+1);
y=[c(1) x(2:r+1)*V'+c(2:r+1)];
nred=y(r+1:-1:1)/x(k+1);
Gr=tf(nred,dred);
```

========== End of file 2: “agg_Z .m ” ==========